UNIVERSITÀ DELLA CALABRIA

UNIVERSITA' DELLA CALABRIA

Dipartimento di Ingegneria Informatica, Modellistica, Elettronica e Sistemistica

Dottorato di Ricerca in

Information and Communication Technologies (ICT)

CICLO

XXXIII

Radianting elements for 5G Backhauling Systems

Settore Scientifico Disciplinare ING INF/02 – Campi Elettromagnetici

Coordinatore: Prof. Felice Crupi

Firma _____ Firma oscurata in base alle linee guida del Garante della privacy

Supervisore/Tutor: Prof. Emilio Arnieri

Firma___ Firma oscurata in base alle linee guida del Garante della privacy

Dottorando: Dott. Carmine Mustacchio

Firma _ Firma oscurata in base alle linee guida del Garante della privacy

ABSTRACT

5G will have to support a multitude of new applications with a wide variety of requirements, including higher peak and user data rates, reduced latency, enhanced indoor coverage, increased number of devices, and so on. These aspects will lead to a radical change in network architecture from different points of view. For example, the densification of small cells produces massive backhaul traffic in the core network, which inevitably becomes an important, but somewhat less addressed bottleneck in the system. In particular, millimeter waves (mm-waves) bands, due to their large unlicensed and lightly licensed bandwidths, have become a promising candidate for the next-generation wireless communications, to accommodate users demand for multi-Gbps data rates, but this will move the attention to the complexity, the criticality and the infrastructure costs of backhauling antennas. In fact, because of the losses produced by the increasing frequency, it will be necessary to use antennas with reconfigurable directional links and, where necessary, to enable the use of massive MIMO architectures.

Among the spectrum portions, the E-band and W-band are the most interesting and attractive. In fact, the unlicensed frequencies in many geographic areas will allow to reduce the operators' costs at the same bit rate. Furthermore, the directive beam steering antennas will allow the capability of spectrum reuse in the same cell. However, there are different unresolved problems, due to the need to use antennas with electronic reconfigurable beam steering both in azimuth and elevation. The spread of this kind of radiator, on a large scale,

will require, necessarily, the development of new antennas that will be able to reduce manufacturing and integration costs.

The main object of this work is to investigate and develop different types of new antennas, which will be able to satisfy all backhauling systems requirements for 5G applications. The research activities presented in this dissertation can be summarized into three parts.

In the first part, a beam-switched Cassegrain reflector antenna in E-band (71-86 GHz) for backhauling systems for 5G applications is presented, including the study of different feeding elements which will illuminate the double reflector system. This antenna has been thought to reconfigure the beam compensating small boom movements, which are estimated to be within ±1° in both azimuth and elevation planes. After evaluating all the possible solutions, an array of magneto-electric dipoles has been selected as feeding element for the E-band beam-switched Cassegrain antenna.

In the second part, the attention has been focused on the study and the design of antennas on-chip (AoCs) in a standard 0.13 µm SiGe BiCMOS technology. In particular, two new techniques for enhancing the gain of on-chip monopole antennas in W-Band (75-110 GHz) are proposed. These new proposed methodologies involved the use of a new AMC (Artificial magnetic conductor), composed by some SRRs (Split ring resonators) and LBE (Localized Backside Etching), and some capacitively loaded SRRs.

In the last part, a I/Q phase shifter design in E-band (71-86 GHz) in a SiGe BiCMOS 55 nm semiconductor technology is proposed. The proposed phase shifter is a sub-block of a compact E-band I/Q Receiver in SiGe BiCMOS for 5G backhauling applications.

TABLE OF CONTENTS

LIST OF FIGURES

LIST OF TABLES

INTRODUCTION

The first aim of this thesis will be the study of new antennas, which will be able to satisfy all backhauling systems requirements for 5G applications in E-band (71-86 GHz) and W-band (75-110 GHz).

A brief introduction on the upcoming new generation mobile 5G, including all the innovations introduced by the new fifth-generation will be presented in the first chapter, focusing the attention on mm-wave antennas, with generic considerations on PCB antennas, antennas in package (AiP), and antennas on-chip (AoC).

Then, the architecture and the requirements of 5G backhauling networks will be taken into account. Furthermore, the state of the art of 5G backhauling antennas will be considered in the second chapter, including all the possible solutions present in literature.

In the third chapter, basic architectural aspects related to the development of a reconfigurable antenna for 5G backhauling applications will be discussed. Different antenna configurations will be taken into account with a preliminary feasibility analysis.

Among the proposed antenna configurations, a beam-switched Cassegrain antenna has been selected, and different feeding elements suitable for illuminating the selected architecture will be considered in the fourth chapter.

With the recent massive use of highly integrated silicon-based circuits, the system-on-chip (SoC) approach has triggered significant interest, as it allows on-chip integration of digital baseband and complete RF front-ends. The higher frequencies, in particular mm-waves,

has reduced antenna sizes to only a few millimeters, making it suitable for on-chip implementation. In the fifth chapter, several techniques for enhancing the gain of on-chip monopole antennas in SiGe BiCMOS technology in W-band will be shown. Moreover, on-chip antennas challenges and benefits will be taken into account and the current state of the art of on-chip antennas will be shown.

Finally, in the sixth chapter, a I/Q phase shifter design in SiGe BiCMOS technology in E-band will be proposed. The selected phase shifter is a sub-block of a compact I/Q receiver in E-band.

CHAPTER 1

5G AND MM-WAVE ANTENNAS

1.1 Introduction to 5G

The amount of wireless traffic and number of connected devices are expected to grow up in the coming future. Today's wireless networks must be renewed completely to deal with the increasing amount of data traffic and the number of connected nodes. Millimeter-wave link frequencies such as 28, 38, and 60 GHz, as well as the E-band (71–76 and 81–86 GHz), have been proposed for use in wireless backhaul infrastructure to enable 5G networks, in fact, millimeter-wave telecommunication for fifth-generation (5G) is finally becoming a reality. 5G will lead us to a digital revolution in which everything will be much better, faster and everything will be connected. 5G is an entirely new network with a broad range of applications and use cases. 5G is a new global wireless standard after 1G, 2G, 3G, and 4G networks. 5G enables a new kind of network that is designed to connect virtually everyone and everything together including machines, objects, and devices. The users of 5G go beyond consumer-centric networks and include business, cities, services, utilities and beyond. 5G wireless technology is meant to deliver higher multi-Gbps peak data speeds, ultra-low latency, more reliability, massive network capacity, increased availability, and a more uniform user experience to more users. Higher performance and improved efficiency empower new user experiences and connects new industries. The challenge of 5G is to support in a flexible way with high fidelity immersive

applications that demand high-speed wireless connections, low latency, high reliability and high number of connected devices; another question is related to the accommodation of all the diverse use cases without increasing the management complexities. 5G systems will be required to support data rates of 10-50 Gbps for low mobility users, providing, for instance, gigabit-rate data services regardless of a user's location. 5G is based on OFDM (Orthogonal frequency-division multiplexing), a method of modulating a digital signal across several different channels to reduce interference. 5G uses 5G NR (New Radio) air interface alongside OFDM principles. 5G also uses wider bandwidth technologies such as sub-6 GHz and mm-wave. Like 4G, 5G OFDM operates based on the same mobile networking principles. However, the new 5G NR air interface can further enhance OFDM to deliver a much higher degree of flexibility and scalability. This could provide more 5G access to more people and things for a variety of different use cases. 5G is designed to not only deliver faster, better mobile broadband services compared to 4G, but can also expand into new service areas such as mission-critical communications and connecting the massive IoT (Internet of Things). This is enabled by many new 5G NR air interface design techniques, such as a new self-contained TDD (Time Division Duplex) sub-frame design. The proliferation of IoT with billions of connected devices will fuel the need for a better QoS (Quality of Service) that cannot be met by old generations. 5G systems will use context information in a real-time manner based on network, devices, applications on the user and his environment, for providing a high QoE (Quality of Experience) for services. 5G will introduce new air interfaces for cognitive designs, new modulation, full-duplex transmission, and so on. The network will include the integration and interoperation with multiple radio access networks (multi-RATs), using unlicensed networks such as 60 GHz

band [1]. Between the most promising innovations of 5G wireless requirements, it is possible to find network densifications with small cells which will increase the network capacity and coverage, achieve wireless network efficiency and extend the mobile device battery life. To avoid data transmission dead spots in the millimeter range, many small transmitting stations are located in close proximity to subscribers. They form a small cell network, which extends the existing cellular network. Expanding the network in this way allows closer proximity to users, yet at a low transmitting power level. Due to the smaller spacing of the stations, the cellular or IoT device can always find a good connection to the next station. Monolithic Microwave Integrated Circuits (MMIC) allow transmission of data at frequencies of up to 90 GHz; the market is currently focusing on frequencies of up to 40 GHz. On the other hand, there are lots of challenges to overcome, such as providing affordable, scalable, and flexible mobile backhaul to connect the small cells with high capacity back into the network [2]–[4]. To realize dense networks for enabling 5G wireless communication infrastructures as key enablers millimeter wave technologies and other lower frequency spectrum sharing architectures are being taken into account. For mobile systems, all the frequency spectrum available is concentrated below 6 GHz thanks to favorable conditions in those bands, but at the same time, these frequencies are requested by other applications including fixed, broadcasting, and satellite communications: thus becoming extremely crowded and not very favourable for transition to 5G architectures. Thanks to the recent advancements in mobile communication systems combined with new antenna and RF component technologies, new nonconventional bands for cellular applications have been taken into account. 5G will bring wider bandwidths by expanding the usage of spectrum resources, from sub-3 GHz used in 4G to 100 GHz and beyond. 5G

can operate in both lower bands (e.g., sub-6 GHz) as well as mm-wave (e.g., 24 GHz and up), which will bring extreme capacity, multi-Gbps throughput, and low latency. Network architectures operating over a spectrum not traditionally used by cellular systems (e.g. 10-100 GHz) will be deployed indoors and/or outdoors to meet 5G network requirements. Signal penetration loss increases, with the increase in carrier frequency, so diffracted signals become very weak, and thus the importance of line-of-sight (LOS) signal as well as reflected signal component increases. Although propagation at mm-wave bands covering 30-300GHz presents some challenges: they cannot penetrate stone house walls and can be absorbed by trees or heavy rain. To remove frequency-dependent propagation loss and to provide higher beamforming array gain is possible to use large antenna arrays [5]. By reducing the impact of interference with narrow beam adaptive arrays, millimeter-wave systems can operate in noise-limited conditions rather than interference-limited situations. Signals are radiated uniformly in all directions using traditional antennas. If signals overlap with those from other transmitters, interference can arise to the significant detriment of the signal transmission. The Massive MIMO multiple antenna technology resolves this problem in combination with beamforming: by sending the same signal at staggered intervals using several antennas, the transmitter targets the approximate location of the client and aligns its transmission power accordingly, thus creating a signal beam or beamforming. This means that a beamforming transmitter can send individual signals to individual recipients in different directions. This increases the coverage, ensures a more stable connection as well as higher transmission rates, and reduces unwelcome radio interference. It is difficult to implement a beamforming with large number of mm-wave front-end transceivers, due to high cost, power consumption, and excessive demand for

real time signal processing needs with high beamforming gains [6]. With analog beamforming the number of transceivers can be reduced, where each mm-wave transceiver is connected with multiple active antennas and a network of analog phase shifters controls the signal phase of each antenna element. Analog beamforming operates normally at the RF frequency by adjusting the phasing of antenna elements. Each antenna element could have its individual phase shifter. This enables a cost-efficient millimeter-wave design. Another possibility is to develop designs with a number of transceivers smaller than the number of antenna elements, but the architecture might introduce severe inter-user interference for inadequate spatial separation between users. For enhancing the performance, to achieve multiple data beam precoding on top of analog beamforming, digital beamforming can be utilized over transceivers. Digital beamforming relies on the precoding of the transmitted signals at baseband. This way both phase and amplitude of each stream can be efficiently controlled. The limitation of full digital beamforming in millimeter-wave designs is the cost of implementation in both hardware and power consumption, as every antenna element should have an individual transmitter/receiver chain from baseband to RF circuitry. Digital beamforming also requires channel state information for the generation of optimal precoding vectors. Large-scale antenna systems can be used with hybrid beamforming for mm-wave applications. Hybrid beamforming combines the benefits of both analog and digital beamforming. A hybrid beamforming system normally consists of antenna element specific analog phase shifters and fewer digital transmitter/receiver chains. It supports analog beamforming and works without good channel state information which is normally required by digital beamforming. A sub-optimal beamforming solution can be formed using analog phase shifters and then

compensated using by digital precoders. High gain antennas are used to make the connection for millimeter wave point to point LOS communications, even though the links between the base station and the user interface rarely have LOS and the use of high gain antennas is limited. In defining 5G system architectures for millimeter wave frequencies, multiple antenna technologies like Multiple-Input, Multiple-Output (MIMO) and beamforming will play an important role [7]. Multi-User MIMO (MU-MIMO) offers increased multiplexing gains and improves spectral efficiency, while Massive MIMO with higher capacity can be obtained by Very Large MIMO (VLM) arrays employed at the base station. Some implications have to be taken into account with the increasing transmit-array sizes, such as for coverage, array gain, inter-symbol, and intra-cell interference control, and transmit power budget optimization; most of the gains can be realized even at manageable antenna dimensions. In applications that don't require backward compatibility, it is possible to perform a Massive MIMO, which can be also provided for backhauling for base stations that serve small cells in a densely populated service area [8]. It is expected that massive-MIMO will be a central technology to create significantly higher capacity in the deployment of hundreds of antenna elements in higher frequency bands such as mm-wave, where antenna dimensions become more practical and in the form of distributed radio heads with centralized processing [9], [10]. In a transmission system using MIMO technology, the data stream is transmitted using multiple transmitting and receiving antennas. This improves the received signal, extends the possible distance, and increases data throughput in general. While LTE usually combines up to eight antenna elements at most, 5G requires significantly more power: Several hundred antennas are frequently used at a receiver-transmitter station in the case of millimeter waves. This optimized multiple

antenna technology, or Massive MIMO as it is known, increases the capacity of the cellular network by a multiple. However Massive MIMO requires an additional technology in order to exploit the advantages of the millimeter waves: the signals can only be focused and transmitted reliably using beamforming, as it is known [11], [12].

5G will be used across three main types of connected services, including enhanced mobile broadband, mission-critical communications, and the massive IoT. A defining capability of 5G is that it is designed for forward compatibility—the ability to flexibly support future services that are unknown today. Three use cases of 5G air interface are eMBB (Enhanced mobile broadband), URLLC (ultra-reliable low latency communication), and mMTC (massive machine type communication).

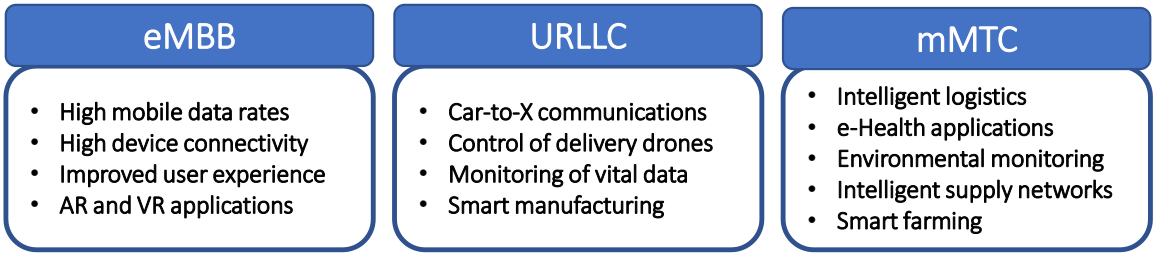

Figure 1-1: 5G major applications

The main object of eMBB is to enhance the system capacity to support the high mobile data rates demand, achieved by pushing the envelope of current limitations of the frequency spectrum. To solve this issue, it is possible to license available bandwidth in sub-10 GHz range as well as open mm-wave frequencies, where wide bandwidth can be easily allocated. In order to multiply the capacity of the network, antenna arrays with multiple antenna elements can enable massive multiple-input multiple-output (MIMO) and beamforming, by exploiting multi-path propagation. eMBB is considered as the initial phase and face of 5G deployment and includes modern broadband use-cases such as Ultra-HD and 360 streaming, and emerging augmented reality (AR) and virtual reality (VR) media and

applications. URLLC provides ultra-response connections with <1 ms latency and 99.9999% availability of connection along with the support of high-speed mobility for mission-critical applications, in fact one of its primary advantages is related to the reliability to support robust and autonomous real-time decision [13]. On the other hand, the ability to process and harmonize various inputs for fast response falls under its domain [14]. 5G can enable new services that can transform industries with ultra-reliable, available, low-latency links like remote control of critical infrastructure, vehicles, and medical procedures. Security, vehicle-to-vehicle (V2V) and vehicle-to-everything (V2X) applications, healthcare, utilities, cloud, and real-time monitoring situations are all use cases of URLLC. mMTC service refers to the robust and cost-sensitive connection of billions of devices such as Internet of Things (IoT) with long-time availability and low power consumption; its use cases include machine-to-machine (M2M) applications with minimal human interaction. mMTC involves a large mesh of low-cost, densely connected devices and considers IoT with low data rate for a large number of connected devices such as sensors with long-range and low maintenance times [15]. 5G is meant to impeccably connect a massive number of embedded sensors in virtually everything through the ability to scale down in data rates, power, and mobility, providing extremely lean and low-cost connectivity solutions.

3GPP has defined two frequency range designations for 5G: Frequency Range 1 (FR1) and Frequency Range 2 (FR2). FR1 covers low and mid-frequency bands while FR2 is solely for mm-wave bands.

The frequency range of FR1 and FR2 are defined below:

- FR1: 450 MHz - 6000 MHz (3GPP Rel. 15 V15.4.0 [16]), 410 MHz - 7125 MHz (3GPP Rel. 15 V15.5.0 [17])
- FR2: 24250 MHz - 52600 MHz Till 3GPP Release 15 V15.4.0, the maximum frequency range of FR1 was 6000 MHz hence the name “sub-6 GHz” became a norm but it was changed to 7125 MHz in 3GPP Release 15 v15.5.0. FR2 has remained the same till the latest report (3GPP Release 16 v16.3.0) [18].

The 5G spectrum is classified into low-, mid- and high-bands:

- Low-band: <1 GHz
- Mid-band: sub-7 GHz (1 GHz - 7.125 GHz)
- High-band: mm-wave (above 24 GHz)

Two approaches are given by 3GPP for the rapid need of 5G roll-out: non-standalone (NSA) and standalone (SA). NSA is the early version of 5G NR as it uses LTE radio access network (RAN) and core with additional support for 5G low and mid-bands (sub-7 GHz). This variant is for fast-to-launch approach preferred by many carriers all over the world. While, the long-term variant, SA has advantages in terms of simplicity and improved efficiency of 5G next-gen core, lower costs, steady improvement of performance in the entire network while enabling URLLC and mMTC use-cases. In particular, SA gives 5G NR the ability for independent deployment as it is an end-to-end solution with a solid basis to exploit its full potential. On the other hand, it presents multiple time-consuming and cost-demanding challenges associated with it such as building new 5G infrastructure [19]. NSA 5G requires more incremental improvements over its SA counterpart. 4G LTE had 40 bands and the 5G cellular networks support even more low- and mid-bands, resulting in complexity in hardware design. The first phase of 5G deployment and its implementation

has introduced challenges by adding more bands in FR1. Similarly, FR2 requires addition of new hardware, resulting in added complexity and miniaturization challenges. This has driven advances in all aspects of the system hardware: from ICs to devices and from cellular devices to base stations [20].

1.2 Mm-wave antennas

The ever-demanding growing need for higher data rates in wireless communications pushes new applications into the mm-wave frequency domain. Base stations for 5G wireless communication, two-way satellite communication, and point-to-point wireless backhaul, and commercial radar are all emerging applications in this domain [21], [22]. These mm-wave applications take advance from using phased array technologies. Phased arrays offer fast electronic beam steering, multi-beam operation, adaptive pattern shaping, and multiple-input, multiple-output (MIMO) capabilities [23]. The available spectrum at mm-wave frequency bands, above 24 GHz, can deliver ultra-high throughput, ultra-low latency, and extreme capacity. It is an essential part of 5G system, but it is necessary to evaluate different complexities, such as:

- link budget: achieve target radiated power with high bandwidths at mmWave frequencies;
- power consumption: support multi-Gigabit throughputs with high power efficiency;
- mobility: maintain reliable mm-wave connectivity in a changing mobile environment;
- thermal performance: support high transmit power while maintaining thermal stability and avoiding localized hotspots;

- regulatory compliance: optimize transmit power and throughput while meeting regulatory requirements;
- stringent size constraints: achieve high antenna efficiency and multi-band support in challenging form factors.

In the 5G network concept, the networks are getting denser than ever before. Millimeter-wave communications play an important role in the backhauling of mobile traffic: for example, millimeter-wave systems operating at 71- 86 GHz (E-Band) area can provide high throughput with very high-frequency reuse by utilizing very narrow beams. The mm-waves area is relatively new in terms of actual products, but it has been an area of research for over a hundred years. Since the data rates in wireless communication systems have been growing very fast recently, the systems operating on the sub-6GHz spectrum are reaching their capacity limits. The big potential of mm-wave is the available spectrum. A very commonly used MIMO technique for millimeter-wave systems is beamforming. With beamforming, it is possible to generate high gain and very directive beams by electronically phasing the antenna elements in an antenna array. Multiple elements transmitting with different phases and/or amplitudes can be used to cause constructive interference towards desired directions and destructive interference towards undesired directions. Eight are the specification requirements for 5G technology: frequency bands, data rate, mobility, latency, forward error correction, access technology, spectral efficiency, and connection density considering connection reliability [24]–[26]. One of the key elements for 5G mm-waves device is the antenna, which is required to work at an enhanced gain, bandwidth, and lesser radiation losses. For this purpose, it is possible to distinguish three kinds of

antennas: printed antennas or PCB antennas, in-package antennas, and on-chip antennas. In the first case, the antenna is implemented directly on the PCB board, the major advantages are related to the lower cost and to the process maturity, while the major challenges are the manufacturing process and the tolerances, in terms of patterning precision and coarse design rules.

Nowadays, because of the short wavelength at mm-wave frequencies, antenna designs are shifting from conventional PCB designs to in-package antennas and on-chip antennas solutions. Compared with the on-chip solution, in-package solutions offer a high gain, broad bandwidth, and cost-effective approach by incorporating multilayer substrate materials and chip-integration techniques. Moreover, the insertion loss between the antenna and chip can be minimized by providing a shorter interconnect. Wire bonding and flip-chip are interconnection techniques available in the packaging industry: the first is well known in consumer electronics and remains a very attractive solution because it is robust and inexpensive. On the other hand, the discontinuity introduced by the bond wire, if not well designed, can significantly affect the performance of the interconnect. While, the flip-chip interconnection, because of its less parasitic inductance; has a better performance than that of the wire bonding but it is more expensive and complex.

In comparison with conventional off-chip antennas, on-chip antennas solution offers several advantages. Firstly, on-chip implementation is more feasible, it integrates the complete RF front-end and the antenna directly on the same silicon die, thereby avoiding lossy interconnections. Secondly, there is no need for an impedance matching network between the antenna and RF front-end in the presence of an antenna on-chip (AoC). Finally, they provide flexibility to designers in the form of antenna and transceiver

components codesign opportunity thus saving precious chip area and design time. Despite its high potential, this approach offers several challenges, one of them being related to the inherent low gain caused by losses in low-resistivity silicon substrates (silicon 10 Ω-cm), which is beneficial for ICs (as it avoids latch-up) but disastrous for on-chip antenna design. Besides, silicon substrate causes the confinement of the power in the substrate thus reducing the portion of fields radiated into the air, this situation is related to the high dielectric constant (silicon relative permittivity constant is ε_R=11.9). All these problems are typical of CMOS or BiCMOS technologies. Another problem is related to surface waves, which are in turn related to the problems listed before, as they interfere with the space waves of the antenna resulting in a radiation pattern with multiple nulls, causing power losses and severely influence the antenna radiation, thus resulting in low gain and low efficiency. The three approaches listed before are all examples of mm-waves antennas that can be employed as feeding elements for 5G networks.

CHAPTER 2

5G BACKHAULING

2.1 Architectures and requirements

With the increasing mobile traffic in the upcoming new generation for mobile communication, better solutions for capacity and coverage should be added to the new backhaul networks, in fact, the capacity requirements of the transmission network that supports backhaul traffic from the core network increase significantly. 5G backhaul mobile networks deals with the well-known issues typical of old generations such as capacity, availability, deployment cost, and long-distance reaches, but introduces new challenges in terms of ultra-low latency and ultra-dense network capabilities.

Mobile backhaul is a portion of the network which connects radio access air interfaces to the cells of the core network which gives the network connectivity to the end-user, or it can be defined as a part of the network which connects the Base Stations (BS) with the Base Station Controllers (BSC). Most of these links mainly rely upon physical mediums such as copper, microwave radio link, and optical fibers based on specific applications. In the first generations, mobile backhauls implementations were time-division multiplexing-based but the packet-based network is inevitable due to latency delay and heavy growth in mobile traffic [27].In the second generation (2G), because of next-generation services availability, service usages fall. In the last decade, with the big developments in mobile devices, there is a change in mobile backhauls applications which

firstly were human-centric traffic and now machine-based traffic; another issue is related to the bandwidth consumption in new mobile backhaul networks with the ever-increasing data. Due to the advancements in technologies, backhaul networks based on 3G and 4G are not able to meet the requirements of gigabits of data rates, in fact, they lack in terms of latency, capacity, cost efficiency, energy, and availability. The upcoming new generation 5G mobile backhaul network will be capable of supporting ultrahigh definition video streaming, high-quality image transfer, cloud resources, and live video games with multimedia and advanced computing features.

5G key concepts will be ultralow latency and small cell concept, the latter provides increased throughput and also efficiently reduces the energy consumption in cellular networks. For 5G mobile communication, mm-wave is a very important backhaul solution, in fact, thanks to the short wavelengths at these frequencies, communications will provide higher transmission bandwidth. As stated before, small cells and so ultra-dense networks are the main characteristics of 5G networks, but they have some limitations in terms of network architecture and cellular densification. Another novelty is introduced by MIMO technology, which can increase the spectrum efficiency of 5G mobile networks. A key concept is related to the increased data rate, which is 1000 times much higher than the previous generation 4G technology, and the most preferred technique to support this application is network densification.

5G networks major challenges can be summarized into eight different points [28]:

- Network capacity: 5G will interconnect and will support different devices, typical of applications such as M2M and IoT. There will be an increased traffic of the

network, so one of the major challenges in 5G cellular network will be the high-capacity requirement from the transport network to the core;

- Ultra-dense network: In this case, network densification is reached by increasing the density of the small base stations (SBS), which support more users in a specific location. From a density point of view, SBS can be augmented until there is only one user-supported per SBS with its backhaul connection and transmission. This intense densification poses lots of challenges such as providing high capacity backhaul connectivity to the SBS and defining the cell associations.
- Frequency: With the use of radio access network frequency band in 5G, the cell site capability will be less if compared to the present micro or macro cell and also cell reach cannot be augmented by 1000 times. To solve this issue, dense small cell implementation is one of the possible and efficient solutions to support this increased capability. On the other hand, with the densification of the cells, the frequency reuse phenomenon is limited.
- Availability: In mm-waves and microwaves, backhaul links are affected because of weather conditions and multipath propagation. To solve these issues, adaptive modulation schemes are used to reduce the line rates. For 5G networks, maintaining availability is essential to reach new services and for many M2M applications.
- Ultra-low latency: As stated before, ultralow-latency and denser small cell deployment are two key concepts of 5G network. On the other hand, in case of an high demand, cost efficiency and network reliability are very crucial while designing these networks.

- Network energy consumption: Energy consumption is an important aspect in order to solve backhaul energy-related bottlenecks. In 5G networks, fifty percent more rise in energy consumption comes from growth in small cell density, from the establishment of Heterogeneous Networks (HetNets), and from the generation of ultra-dense networks.
- Deployment cost: In order to provide an increased network capability, a big issue is the establishment of a cost-effective backhaul solution in 5G networks. To meet the customer demands, an application-based traffic-engineering system is required.
- Coverage: In 5G networks, the main disadvantage of dense small cell deployment is massive backhaul traffic at the supercell, which is an aggregation point where the traffic is concentrated, and all the cells are connected together. This creates congestion, and it may result in collapsing the backhaul networks [29]. In recent years, coverage is one of the challenges for backhaul networks based on 5G.

Among mobile backhaul solutions for 5G networks, it is possible to distinguish wired and wireless backhaul solutions. As wired solutions, it is possible to take into account optical fibers and T1/E1 lines. T1/E1 cables represent the main type of typical backhaul option, which interconnects the BSC and the Base Transceiver Stations. For backhaul networks, optical fibers are the most preferred for their huge bandwidth, increased capacity, coverage, and their improved Bit Error Rate. On the other hand, this technology poses different challenges, such as its time-consuming deployment and the problem to lay fibers at mountains, highways, rivers and under buildings; other influencing factors are represented by optical fiber transport and aggregation costs. On the contrary T1/E1 copper cables suffer from poor bandwidth granularity which increases with the growth of T1 or E1, but recently

effective cost solutions such as digital subscriber lines are largely adopted as cellular traffic backhaul solutions.

Due to its viability and cost-effectiveness, wireless backhaul is in use worldwide; as well as optical fibers and T1 and L1 copper lines, its implementation depends on different parameters such as propagation conditions, cost factors, site locations, interference conditions, and traffic intensity. Moreover, as wireless backhaul medium, microwave and millimeter-wave provide end-to-end control of the network to the operator.

Mm-wave is principally used for small cell backhaul solutions for its enormous spectrum, especially in the high-frequency range which includes frequencies from 30 GHz up to 300 GHz, while the range which covers frequencies from 6 GHz to 60 GHz also support RF mm-wave backhaul networks. Thanks to the smaller wavelengths, it is possible to integrate multiple antennas and small cells resulting in Massive MIMO in LOS or non-LOS applications. When compared with microwave techniques, mm-wave backhaul techniques are able to reach high data rates (1-2 Gbps) with a small reach, which causes high propagation loss. This is caused by phenomena such as fading due to rain, absorption, and multipath propagation. The mm-wave communication suffers narrow beams phenomenon which brings to alignment problems and can be solved by using mm-wave RF equipments in a solid structure. Mm-wave is a wireless backhaul solution for small-cell networks in the upcoming 5G network, in this scenario RF components of transceivers, in terms of modulation and beamforming, and the antenna array play an important role.

Microwave bands are used as backhaul frequencies bands with a maximum distance of 50 km. The supported data rate is up to 500 Mbps, but by using ultra-high spectral efficiency schemes, such as MIMO or LOS, or advanced modulation schemes, such as

4096 QAM or much wider channel gaps, it can be boosted up to 10 Gbps for medium and long-haul communications. At the moment, 50% of mobile backhaul traffic comes from microwave RF technology. The advantages of microwave RF usages are lower deployment time and cost-efficient; on the other hand, its performance is adversely affected by weather conditions and propagation environment.

Satellite backhaul is another solution for mobile backhauling. It can be implemented in fringe areas of the network, especially in rural scenarios in emerging markets. It can be also defined as an emergency backhaul communications link solution in developed and emerging markets. Furthermore, satellite backhaul may be deployed as a temporary measure, waiting for regulatory microwave licenses to be approved. The 3GPP has already evaluated the potential of satellites for 5G backhaul as part of Release 14. To define the technical aspects of integrating satellite networks into 5G network infrastructure deployments, 3GPP is considering two possibilities. One study aims to define deployment scenarios and related system parameters as well as to gain more information on channel models. The second phase of the study will handle the evaluation and definition of RAN protocols and architecture [30].

The spectrum for 5G wireless backhaul takes place in the sub-6 GHz (licensed and unlicensed), microwave (6 GHz to 40 GHz), V-band (60 GHz), E-band (71 GHz to 86 GHz), and W-band (92 GHz to 114.25 GHz) as well as the D-band (130 GHz to 174.8 GHz). Worldwide most of the mobile backhaul links are concentrated in bands below 23 GHz. Significant regional differences come from rain intensity statistics, for example in Europe frequencies particularly involved are 26 and 38 GHz after 15, 18, and 23 severely crowded, while in Far East and in Latin America they are concentrated mostly on 7/8, 15,

18 and 23 GHz. E-band is growing fast and it can be a valid solution for tropical countries such as India, where there are still untapped bands above 23 GHz and E-Band [31]. Considering E-band, W-Band and D-Band, it is possible to do some considerations: the E-Band is the most mature technology with lots of applications, W-Band, in CEPT ECC released Recommendation (18)02, is considered as an extension of the E-Band considering propagation characteristics and technology availability, and D-Band, in CEPT ECC released Recommendation (18)01, the availability of huge amounts of spectrum in this band and its favourable propagation characteristics, makes this a high priority band for the industry.

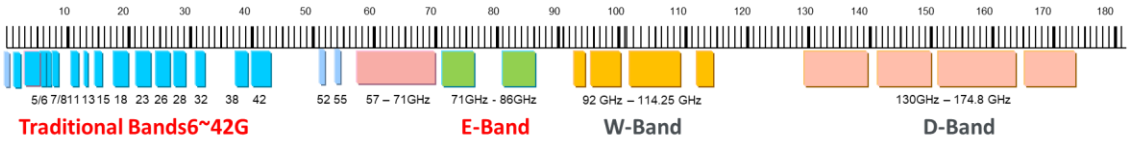

Figure 2-1: Spectrum for backhauling [31]

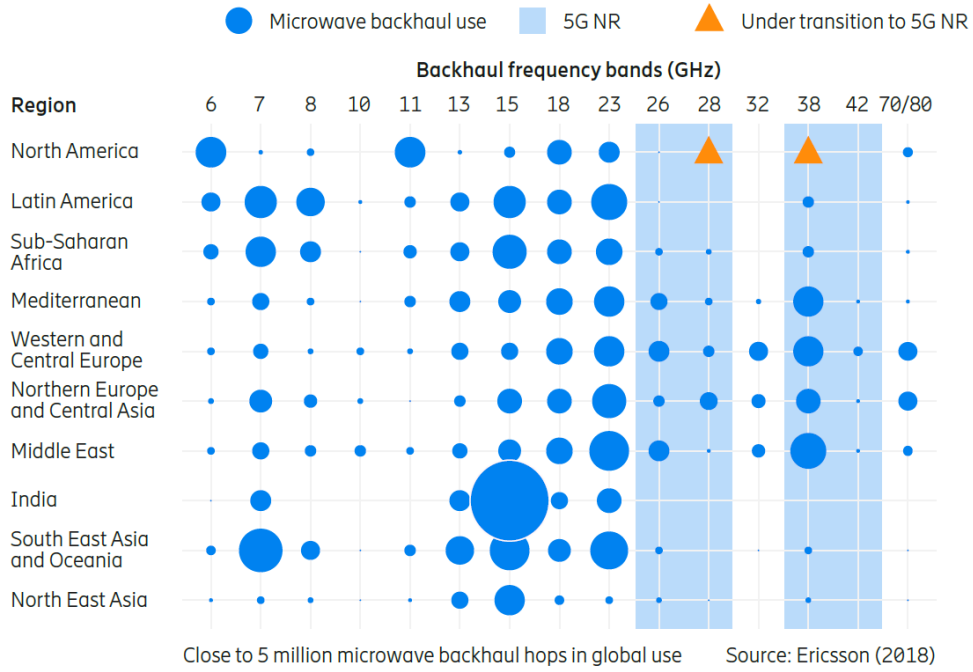

Figure 2-2: Backhaul frequency bands (GHz) in global use [31]

2.2 Backhauling antennas: State of the Art

In this section will be evaluated the State of the Art of backhauling antennas, taking the mm-wave frequencies as target. In particular, the attention will be focused on the E-Band and W-Band because the radiating elements which will be presented in the next chapters have been designed taking into account these mm-wave bands. The use of mm-wave bands for the design of data transmission and sensing systems has various advantages such as high data rate, given by the large bandwidth which resolves the spectrum crowding; reduced size, in which the short-wavelength allows the design of small antennas of high directivity; and finally the possibility to fully monolithically integrate the transceiver in a single chip [32]. For backhauling purpose, millimeter-wave wireless technology requires antenna systems with high gain (narrow beam) and the capability of electronic beam steering. That is necessary to provide a sufficient link budget and simultaneously to cover a large angle of view. A large class of millimeter-wave antennas is obtained by wavelength scaling of well-established antenna configurations developed for the microwave and lower frequency bands [33]. The antennas for such bands are typically required to have high gain, wide operating bandwidth, and low cross-polarization. There are several possibilities, going from basic antennas, which include patch, slot, monopole or dipole antennas, to reflector antennas, which comprise single or dual reflector configurations, Cassegrain configuration, and so on; passing from other applications which embrace a new type of antennas such as magneto-electric (ME) dipole or stacked patch antenna arrays, especially for beamforming purpose. Other radiating elements suited for these requests are aperture antennas, which include for example lens antennas or Fabry-Perot (FP) antennas. All these antennas are well suited for mm-wave applications in the bands of our interest, but at the

same time, they differ on the specific application which can require for example a reduced size, an high directivity antenna, a large bandwidth, and so on. For instance, high directivity can be fulfilled by using conventional lens [34], [35] and reflector antennas [36], [37]. However, if we consider other specifications such as low profile, lightweight, and easy installation, planar antennas are generally well suited for long-distance mm-wave wireless communication applications. At the same time, there are many challenges in the design and implementation of E-band and W-band antennas, which include the high conductor losses, high costs, and high sensitivity for the fabrication process. Another important challenge is related to the fact of developing high performance antennas at these frequencies with planar form and low cost which will be suitable for the future massive commercial E-band and W-band wireless [38].

One of the most popular low-profile antennas in microwave frequencies is microstrip patch antenna array, but at the same time low radiation efficiency, generated by surface wave losses, radiation loss, and dielectric loss inhibits their applications in the mm-wave spectrum [39], [40]. Another commonly used planar antenna is the slotted waveguide array, they can differ in air-filled waveguide, laminated waveguide, substrate integrated waveguide (SIW), and gap waveguide [41]–[46]. On the other hand, the conventional slotted waveguide arrays usually suffer from narrow impedance bandwidth or radiation pattern bandwidth. In recent years, the substrate integrated waveguide (SIW), which keeps similar merits of its planar counterparts and has lower loss than that of the microstrip antenna, has been proven to be a good design for high-performance microwave and millimeter-wave components, even for E-band, W-band and beyond applications. On the other hand, the resonant-slot SIW array antenna suffers from a relatively narrow impedance

bandwidth, and also as the number of radiation slots increases, the operating bandwidth decreases quickly since the impedance of the resonant slot varies significantly apart from the resonating frequency [47]. There are different techniques to enhance the bandwidth and the gain for these antennas such as: using hybrid cavity modes [45], using corporate feeding networks [41], optimizing the height of the loaded cavities for decreasing the Q values [48], etc. Other applications involve composite structures where different antennas are combined together with the waveguide, such as SIW aperture coupled magneto-electric dipole [49], [50], SIW feed patch arrays [39], [51], gap waveguide feed patch arrays [52] and air-filled waveguide feed patch or magneto-electric arrays [46], [53].

Mm-wave antennas are generally presented as aperture antennas in the form of reflectors and lens antennas or antenna arrays, depending on system requirements. Aperture antennas are regarded as promising candidates to provide high gain radiation patterns, while antenna arrays offer a flexible antenna policy from which high gain antenna patterns, including adaptive ones like phased arrays, can be realized. The main drawbacks of arrays are represented by the complexity of beam-forming networks and also by the potential losses related to them [54].

In the E-Band and W-band other most conventional high gain antennas used are parabolic reflector antennas, but because of the high operating frequency, they will have high production costs caused principally by the complex machining process. Another factor that has to be taken into account is related to the big size and the weight of the antenna, which result in high shipping costs and heavy manpower expenditure on equipment installation and adjustment [55]. On the other hand, reflector antennas are able to provide at least 50 dBi of peak gain. Other attractive solutions to design high gain antennas at mm-

wave frequencies are planar reflectarray or discrete lens antennas and they can be a valid substitute in terms of size, installation, low cost, small volume, and lightweight for the traditional reflector antennas.

For instance, the lens, compared to the reflector, offers more degrees of freedom in the design [56]. Lens antennas have been receiving considerable interest recently due to their advantages such as multi-beam availability and potentials for wide-angle beam scanning. In order to take advantage from lens benefits, various beam-switching integrated lens antennas (ILAs) with homogeneous material lens and a planar antenna mounted on the lens back plane were proposed based on geometrical optics (GO) [57] or 3-D full-wave simulation tools [58]. Both lens and reflector antennas are often criticized because they provide high gain, but on the contrary, they are non-planar structures with a noticeable size. In [59], a technique for reducing the height and weight of extended hemispherical lenses is proposed, based on the introduction of a cylindrical air cavity above the primary feed.

Other planar antennas that could be a valid solution for mm-wave antennas for backhauling applications are reflectarrays, which combine the best features of reflector antennas and antenna arrays. They provide good efficiency and a high degree of flexibility in synthesizing arbitrary antenna patterns. They are regarded as planar antennas because the array and the scatters are usually planar. Reflectarrays mimic the behaviour of a curved reflector, so each scatter has a configuration that produces a phase shift to compensate for the path lengths and successive phase delays introduced between the antenna and the reflector. Generally, reflectarrays can be imagined as an array of phase shifters capable, over a defined frequency range, to distort electrically the surface to represent the electromagnetic behaviour of a physical reflector. The first reflectarray elements were

based on resonators, based on the fact that pronounced shifts in the phase of the scattered field can be produced in the vicinity of the resonant frequency of the scatterer. Such designs employed printed dipoles/patches slots, rings, and other interesting shapes to realize the resonator.

In the last years, researchers are posing their attention on reconfigurable reflectarrays capable of tuning the response of the scatterers to provide adaptive beam-steering and beam-forming capabilities, while at first reflectarrays were approached to realize fixed-beam [54].

Fabry-Perot Cavity Antennas (FPCAs) are another type of highly directive planar antennas, well suited for mm-wave frequencies and for backhauling applications, which can be a valid alternative to microstrip patch arrays or waveguide slot array antennas. Among its advantages is possible to find low fabrication complexity, high radiation efficiency, and good radiation pattern performance. The concept of Fabry-Perot Cavity antenna was introduced in 1956 by Trentini [60], although the term wasn't used at time. In this work, have been proved how several types of periodic surface, acting as partially reflective surfaces (PRSs), can enhance the directivity of a single waveguide aperture surrounded by a ground plane. The FPCA is formed by an excitation source, for example, a slot in the ground plane, a microstrip patch or a dipole, and a partially reflective surface (PRS) placed at a distance of about half-wavelength and in parallel to a ground plane thus forming an open Fabry-Perot resonant cavity. The characteristics parameters of the FPCA, such as gain and bandwidth, are related mainly to the reflection from the PRS as well as the distance from the ground plane. There are different possibilities to represent the PRS, they can be a passive periodic array in the form of Frequency Selective Surfaces (FSSs),

used for filtering electromagnetic waves, or metasurfaces with sub-wavelength and potentially non-uniform unit cells [54]. In recent years different applications have been proposed for Fabry-Perot Cavity antennas for mm-wave spectrum, involving for example 2D metallo-dielectric arrays of conducting elements [61], [62] or metallic periodic arrays of apertures in a conducting sheet [63]; other implementations employ one or more dielectric layers with different dielectric constants and thickness functioning as PRS [64]–[66]. The use of superstrates reduces the degrees of freedom in the design, but at the same time presents benefits in terms of reduced fabrication complexity.

Other attractive radiating elements in the mm-wave spectrum for backhauling applications are represented by stacked patch and magneto-electric dipole; in last years, these solutions are well suited for phased-array approaches.

Stacked patches consist in stacking a secondary parasitic patch on a driven fed patch, this approach gives the possibility to enhance the bandwidth and the gain of the simple microstrip patch antenna, but on the other hand, the disadvantage of this approach is the additional fabrication cost [67].

Magneto-electric (ME) dipole antenna has been studied and discovered in recent years [68], it is regarded as a complementary antenna where an electric dipole is combined with a vertically shorted planar magnetic dipole; in particular, the feeding is provided to the magnetic dipole from the bottom side of the substrate. The ME dipole owns a high front-to-back ratio, low sidelobe and back lobe level, wide bandwidth, and low cross-polarization. These features make this antenna very suitable for mm-wave applications for backhauling purpose [49], [69].

CHAPTER 3

BACKHAULING ANTENNA CONFIGURATIONS

3.1 Preliminary considerations

In this chapter, will be described basic architectural aspects related to the development of a reconfigurable antenna for 5G backhauling applications.

Different antenna configurations will be taken into account performing a preliminary feasibility analysis. This study is focused on integration aspects and on dimensional feasibility thus not taking into account link budget analysis. The antenna architectures taken into account in this work are analyzed based on the following preliminary considerations. The idea of developing a direct radiating array is discarded for two main reasons. First, because of the losses which would be generated in the power distribution network. The second motivation is related to the limited beam steering requirements which, combined with the high gain requirements, would not justify the implementation of a conventional direct radiating array. Mechanical steering is not taken into account.

3.2 Possible antenna configurations

Different antenna configurations will be taken into account such as: phased array-fed reflector antenna, reconfigurable reflectarray-fed reflector, beam-switched reflector

antenna, beam-switched Cassegrain reflector antenna, reflector antenna with beam switching discrete lens, and confocal reflector antennas.

3.2.1 Phased array-fed reflector antenna

The geometry of this antenna is shown in **Figure 3-1**. It consists of a prime focus parabolic reflector antenna whose feed consists of a phased array [70]. In the simplest configuration, this antenna employs a single parabolic reflector which collimates the spherical waves originating from the feed to a given direction. The feed consists of an active electronically scanned array (AESA) which allows the reconfiguration of the reflector surface illumination as it is required to scan the reflector beam. Usually, the offset design is preferred as it avoids the feed blockage. The AESA size is usually higher than the horn feeds even though its size depends on the reflector F/D ratio. The phase of each element of the AESA has to be controlled in order to scan the reflector beam. Different approaches can be used to synthesize the AESA amplitude and phase distribution. On typical example is the conjugate field matching (CFM) method [71]. In general, to avoid beam aberrations, the phases of each AESA element in a given position, $\phi_A(m,n)$, should be calculated taking into account the phase of the field scattered by the reflector surface, $\phi_{Refl}(m,n)$. In order to steer the reflector beam to a given direction, the sum of the two phases should be constant:

$$\phi_{Refl}(m,n) + \phi_A(m,n) = K \tag{1}$$

With respect to beam scanning techniques achieved by moving the feed away from the reflector focal point, this approach provides less scanning losses [72]. However, this effect becomes less relevant when the scanning range is small as it is for the case at hand.

Feed blockage effect can be avoided by using offset configurations. It is worth noticing that this type of configuration requires an F/D significantly higher than other architectures. The AESA size, d_a, can be estimated assuming an inter-element spacing, i_a, of $\lambda/2$ or 0.7λ. In the proposed configuration, each AESA element should be controlled in phase and, possibly, in amplitude.

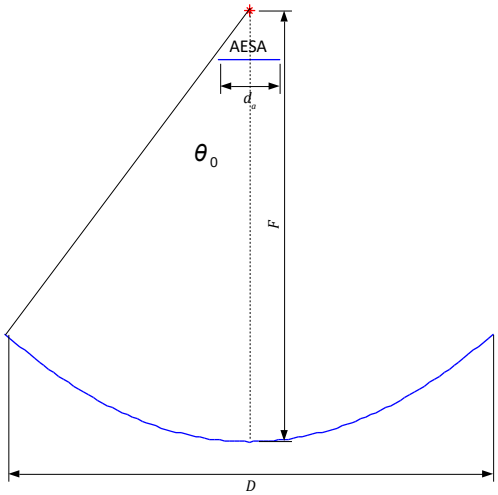

Figure 3-1: Phased Array-Fed Reflector (PAFR) antenna geometry

In principle, the PAFR configuration would be an effective solution for beam steering reflector configurations. Its main advantages are related to the possibility to have a better control on the synthesis of the feed pattern which can, in turn, avoid or correct distortions of the reflector pattern. Feed blockage can be avoided using off-set feeding configurations or folded architectures (e.g. Cassegrain). The same reflector could be used for Tx and Rx channels by using two off-set AESA. Nevertheless, the feasibility of the PAFR configuration is limited by possible integration issues which would likely arise in a real application scenario.

3.2.2 Reconfigurable reflectarray-fed reflector

This configuration reflects the architecture shown in the previous section but the array, instead of having a corporate distribution network, is a reflectarray, i.e. it is spatially fed. The reflectarray acts as a reconfigurable secondary reflector which is illuminated by an external feed [73]. The phase of each reflectarray element can be determined following the approach of equation (1) but including, in this case, the effect of the feed as shown in the following expression:

$$\phi_{Refl}(m,n) + \phi_A(m,n) + \phi_{Feed}(m,n) = K \quad (2)$$

where $\phi_{Feed}(m,n)$ is the feed phase.

In principle, the reconfigurable reflectarray size should not be the same of the AESA feed of the previous section. The effective size, indeed, depends on the radiation pattern of the primary feed and on the overall antenna configuration as well as on the efficiency requirements. Nevertheless, the integration aspects, which are being investigated in this chapter, are similar to the AESA with one major exception. The reflectarray, indeed, does not require a corporate distribution network. Therefore, the number of passive blocks to be implemented for the integration is limited to a minimal intra-cell routing and to two transitions for each antenna.

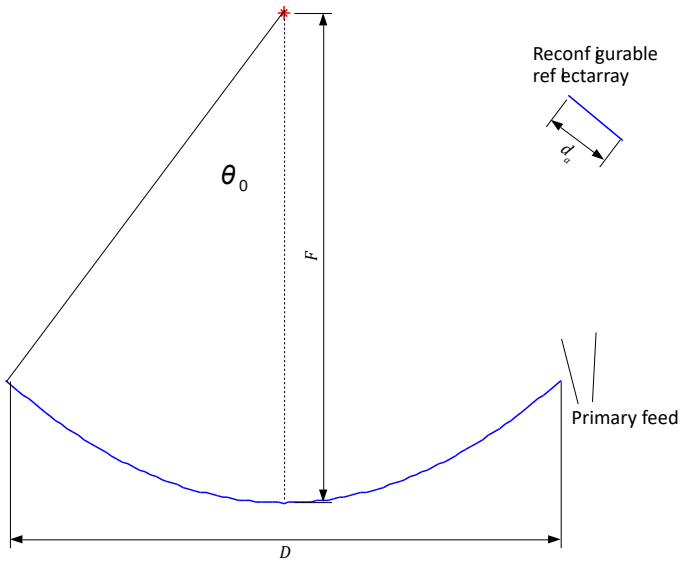

Figure 3-2: Reconfigurable reflectarray-fed reflector antenna geometry

The reconfigurable reflectarray-fed reflector presented in this section is an alternative to the PAFR architecture described in section 3.2.1. With respect to the PAFR, the configuration at hand has a simplified structure of the manifold due to the absence of a corporate feed network. This feature results in a higher efficiency when the size of the reflectarray becomes larger. For smaller sizes of the reflectarray, this peculiarity is limited by spillover losses in the sub-reflector. The absence of the feeding network avoids also the use of an IF section as well as buffer amplifiers which should be taken into account in the design of a large AESA. Therefore, the configuration proposed in this section appears to be sustainable in terms of integration capacity although further investigations are requested to validate the preliminary results presented in this section.

3.2.3 Beam switched reflector antenna

The configuration proposed in this section is based on the focal-plane array concept. This reflector configuration consists of a reflector antenna fed by an array of feeds located in the reflector focal plane [74]–[76]. As shown in **Figure 3-3**, each array element, or sub-sets of array elements, can be used to create a beam feeding for the reflector. Typically, focal-plane arrays are implemented using a cluster of horn antennas so as a multi-beam reflector can be achieved. Aberrations and distortions might affect off-axis beams thus leading to a reduction of the aperture efficiency. The different beams can be also combined to generate other beam configurations. Is worth noticing that, in this case, each feed configuration would illuminate only a portion of the reflector from an off-focus position. Therefore, this would generate a distortion of the reflector beam and a reduction of the overall efficiency. In order to generate continuity between two adjacent beams, the different feeds in the array can be connected to the MMIC along with an IF switching/combining unit. This approach has the advantage of having the switching /combining unit operating at a lower frequency (i.e. with lower losses) while having the power and low noise amplification units closer to the antenna. Nevertheless, there is the drawback of a higher integration area.

The geometrical description of the antenna configuration proposed in this section is shown in **Figure 3-3**. The array of feeds is integrated in a single PCB board having on one side the radiating elements and on the opposite sides the MMICs. One MMIC is required for each feed whereas other chips (or another chip) are necessary to implement the switching/combining unit. As for the previous configurations, also in this case it is possible to use a multi-reflector configuration (e.g. Cassegrain will be described in the following

section). The size of each cell is m_a. Therefore, the feed can be laterally moved of multiples of m_a. Assuming a lateral displacement of the feed at d_f (corresponding to an angular displacement θ_f, the main reflector beam scans at θ_b off axis. The ratio θ_f/θ_b is called beam deviation factor (BDF) [77]. Two examples of BDF are reported in **Figure 3-5** for two reflector configurations having F/D=0.3 and 0.4. As it can be observed, BDF is always higher than one meaning that the lateral movement of the feed should be higher than the beam off-axis angle. This tendency is reduced when the F/D is increased. However, this option is not viable as it requires more directive and therefore larger, feeds. The use of dual reflector configurations can reduce the BDF to values lower than the unity thus providing larger room for the integration.

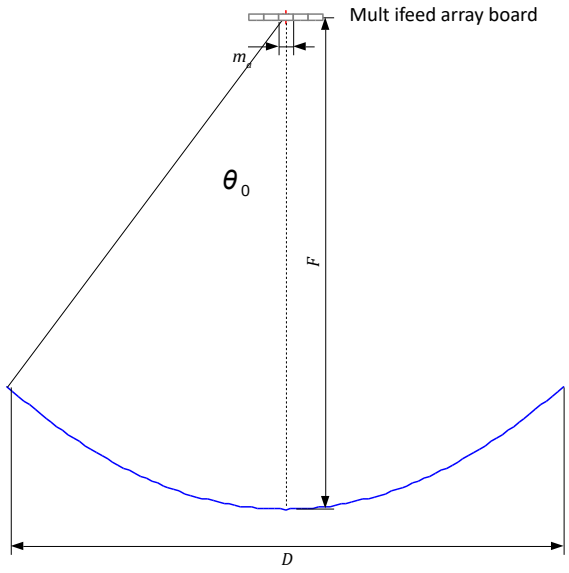

Figure 3-3: Switched beam reflector antenna geometry with a feed array on the reflector focal plane

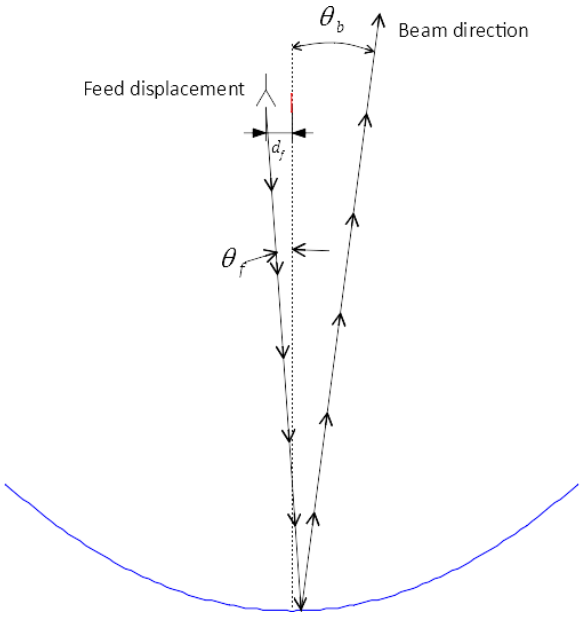

Figure 3-4: Far-field beam and feed off-set

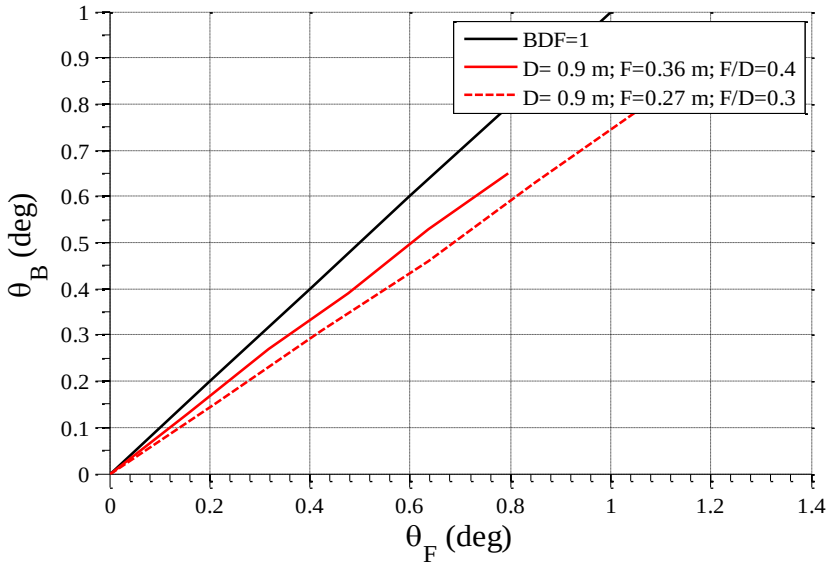

Figure 3-5: Beam deviation factor for two different configurations of single reflector

The integration aspects are explored in the case of a single reflector at 75 GHz. The reference values are summarized in **Table 3-1**. Considering that for D=0.9 m the HPBW is equal to 0.3 deg, beam switching within the HPBW requires the angular off-set between two adjacent beams to be not higher than 0.3 deg (i.e. θ_F should be designed to achieve θ_B equal to 0.3 deg). It is worth noticing that the BDF is not constant for all values of θ_B. Consequently, the values of m_a shown on **Table 3-1** are subject to small changes.

D (m)	**F/D**	**θ_0 (deg)**	**m_a (mm)**
0.9	0.3	79	1.88
0.9	0.4	64	2.2
0.9	0.5	53	2.8

Table 3-1: Beam switching single reflectors

The value of m_a fixes the available space for the integration of the chips, of the radiating elements, and of the switching and distribution/combining circuit. The radiating element size, whose value can change depending on several factors, is also essential to determine the reflector illumination efficiency. As an example, the directivity of the reflector vs. the feed taper at θ_0 is shown in **Figure 3-6**. As it can be observed, for the three configurations at hand the optimal gain value is reached when the amplitude taper is comprised between -10 and -5 dB with a directivity deviation of less than 0.5 dB. It is worth noticing that the integration issues are due to the size of the MMIC rather than to the size of the radiating element. Indeed, considering that the requirements on the link-budget for the application at hand are broadly matched, it would be easy to implement the focal plane array by using simple patch antennas combined with a focusing element which can be a dielectric lens or

a parasitic radiator. In both cases, this arrangement will cover the beam taper requirements shown in **Figure 3-6**-a.

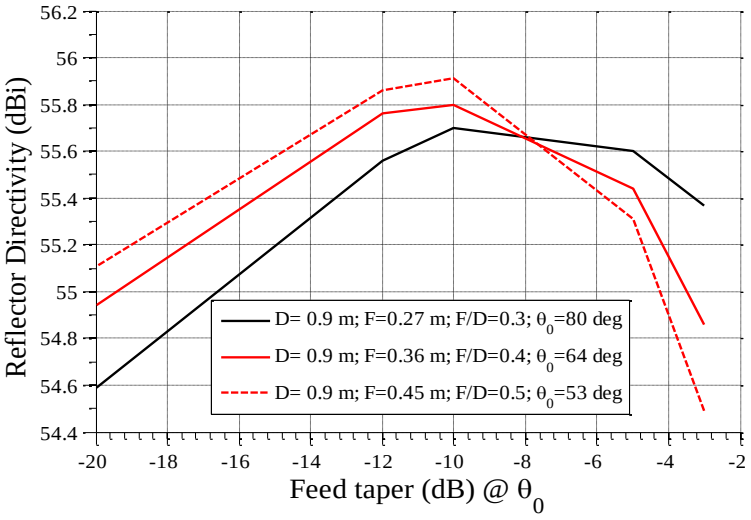

(a)

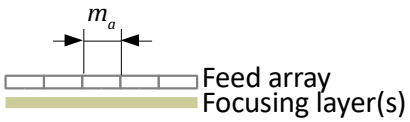

(b)

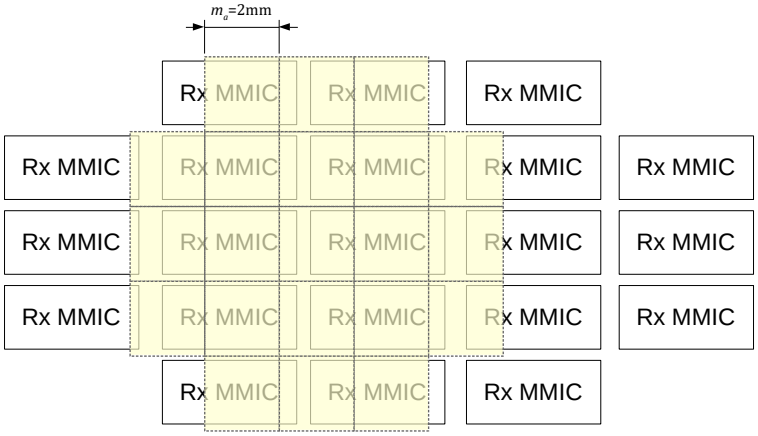

(c)

Figure 3-6: a) Reflector directivity vs. feed taper angle at θ_0 when $\theta_B = 0$ deg; b) pictorial view of the feed array board with focusing layer to control the feed directivity; c) example of array of feeds with integrated MMICs

The single reflector antenna with switched beam feeds might be a valid solution for the application at hand only if small feeds are used. For example, considering m_a equal to 2 mm, the array of feeds to be placed on the reflector focal plane is shown in **Figure 3-6**-c. Based on the results shown in the previous section, this cell size should be sufficient to achieve a beam shift of 0.3 deg while providing enough room for the integration of a single patch antenna. A stacked arrangement or a focusing layer should be used to increase the single feed directivity. The overall array of feeds is comprised of 21 cells. Each cell is connected to one chip (Rx MMIC in the example). The area occupied by the MMIC exceeds the area of the radiating unit cell ($m_a \times m_a$) thus making difficult the integration. Nevertheless, the limited number of elements to be used in the array allows extending the MMIC integration area beyond the limits posed by the radiating elements. If needed, the on-chip phase shifter could be used to control the channel phase, if required. In order to simplify the integration, the chip configuration should be changed to include the switching elements (not shown in **Figure 3-6**-c) required by this antenna architecture. If this would be possible, the same front end could be used, for example, to serve two feeds thus simplifying the overall design of the array board. On the other hand, the efficiency reduction due to feed blockage would be minimal as the size of the array of feeds would be limited to a centimeter. The most challenging aspect of this solution is, instead, on the board manufacturing technology which should be more advanced with respect to standard PCB processes.

3.2.4 Beam switched Cassegrain reflector antenna

Dual reflectors and, in particular, Cassegrain reflector antennas can be a valid alternative to single reflector antennas. Indeed, Cassegrain reflectors allow having beam deviation factors lower than unity thus making possible to achieve larger sizes of the unit cell size, m_a. The geometry of the Cassegrain reflector antenna with a switched beam feed is shown in **Figure 3-7**. An array of switched feed points towards the sub-reflector which reflects the beam to the main reflector.

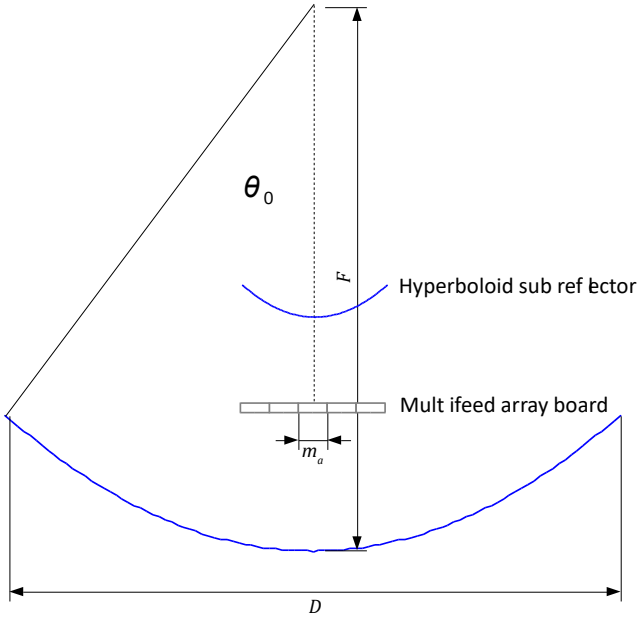

Figure 3-7: Geometry of the Cassegrain antenna with switched feed

As for the single reflector, a lateral displacement of the feed, d_f, results in a squint of the main reflector beam at an angle θ_B. As it can be observed in **Figure 3-8**, the Cassegrain reflector has a beam deviation factor higher than the single reflector case resulting in a wider integration area. A higher value of the eccentricity of the secondary reflector, although requiring more focused feeds, results in lower beam scanning losses.

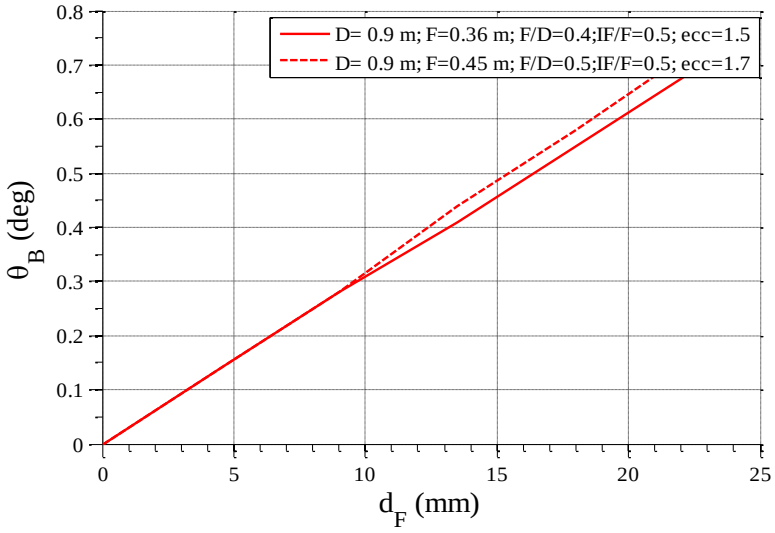

(a)

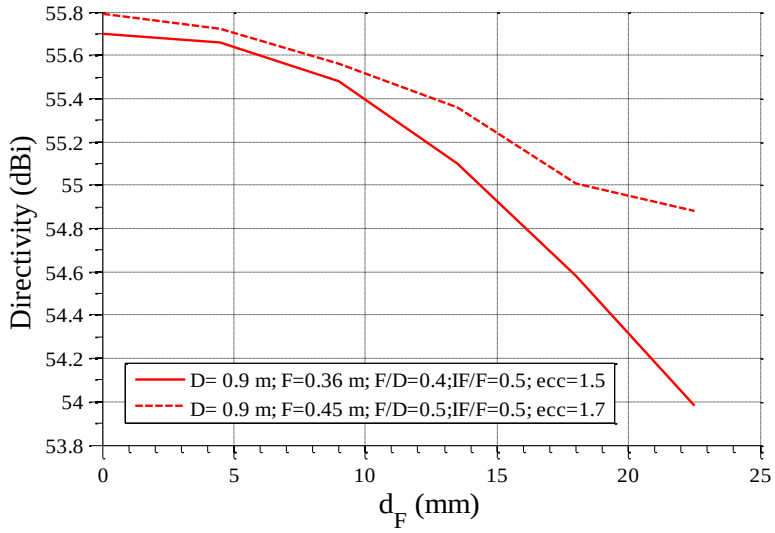

(b)

Figure 3-8: Cassegrain reflector: a) beam tilt vs. lateral feed displacement; b) Reflector directivity vs. lateral feed displacement

The effect of the feed directivity was analyzed by simulating in TICRA Grasp [78] the gain of the Cassegrain reflector with D=0.9m, F/D=0.5, IF/F=0.5, and ecc=1.7 when excited by different feed typologies. In particular, the feed taper at $\theta_0 = 14.7$ deg was taken in the

range from -12 to -3 dB. Results, reported in **Figure 3-9**, show that the effect directivity of the feed on the reflector directivity is greater with respect to the single reflector configuration. An acceptable range of feed amplitude taper from the axis to the sub-reflector rim, $\theta_0 = 14.7$ deg, is comprised between -12 and -6 dB. It is worth noticing that even considering an amplitude taper of 6 dB at θ_0 in a single plane would require a uniform array of 5 elements spaced at half a wavelength. Therefore, the size occupied by each feed would be equal, at 75 GHz, to about 8 mm. Higher values of directivity will thus exceed the expected unit cell size, m_a. More complex feed structures should be studied to overcome this problem. For example, as mentioned in the previous section, a superlayer could be used to increase the directivity of the single feed. Other compact printed structures providing high directivity include cavity-backed printed antennas or shorted patch antennas. A dedicated study is required to validate the feasibility of these alternative solutions.

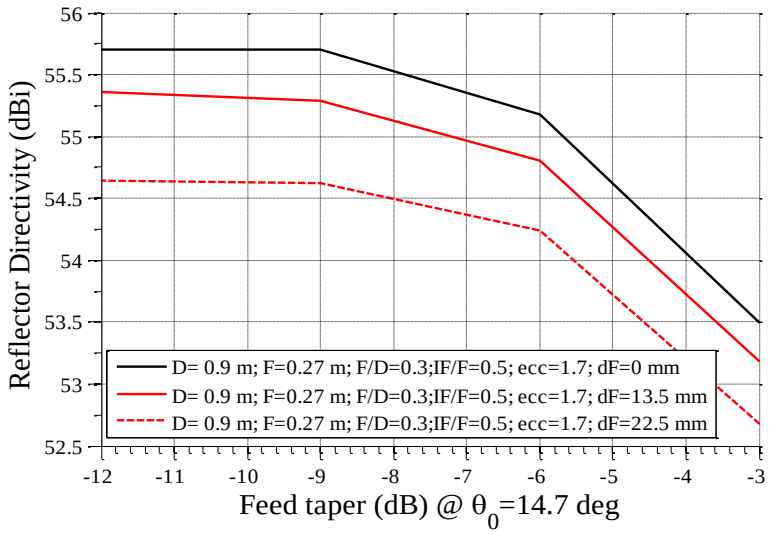

Figure 3-9: Effect of the feed taper over the directivity of the dual Cassegrain reflector (D=0.9m, F/D=0.5, IF/F=0.5, and ecc=1.7)

The Cassegrain reflector configuration with switched feed array appears to be a theoretically valid solution but it poses several integration challenges. In particular, the preliminary study shows that the needed feed directivity is not compatible with the lateral feed displacement required to achieve the desired off-axis beam squint. While in the case of the single reflector the limit was due to the size of the MMIC, in this case, the limitation is generated by the high directivity of each feed which is not compatible with the required lateral displacement. Alternative antenna configurations should be analyzed to verify the feasibility of this approach.

3.2.5 Reflector antenna with beam switching discrete lens

As an alternative configuration that provides another degree of freedom in the design of the reflector optics, in this section is proposed a single reflector (e.g. D=0.9 m) fed using a discrete lens with beam switching [79]. The proposed geometry is shown in **Figure 3-10**. Depending on the active feed, the discrete lens pattern can be scanned to an off-axis angle. With respect to the reflectarray solution, this approach has the advantage of offering more degrees of freedom while posing less complex integration challenges. A classic example of constrained lens array (CLA) is the Rotman lens [80] which is typically used to achieve beam scanning on a single plane. The basic design principles which will be presented in this section are based on the assumption of using a constrained lens which is the discrete lens configuration offering the higher number of degrees of freedom. The reference geometry is shown in **Figure 3-10**-c and, in a more detailed view, in **Figure 3-10**-d. The radiating surface is made up of a linear uniform array. Each element on the radiating surface is back-to-back connected to the internal surface through transmission

lines. Other antenna elements are present on the internal surface, which forms a cavity with the focal surface where the array of feeds is located. In the form shown in **Figure 3-10**-d, the constrained lens has three degrees of freedom, namely: the shape of the internal surface, the relative position between the elements on both sides of the lens and the phase delay added by the transmission lines interconnecting each couple of radiating elements. A simplification of the proposed lens structure can be achieved by using a planar (i.e. printed) constrained lens [81] which leads to a transmit array configuration (**Figure 3-10**-b). An interesting example of this type is shown in [82]. In this work, beam switching is realized integrating by means of flip-chip technology an off-the-shelf (Triquint TGS4306-FC) single-port four-throw (SP4T) MMIC which activates four different feeds implemented by an array of printed slots. The antenna gain is about 32 dBi in E-band. It is worth noticing that this configuration implements beam scanning on a single plane and the OP1dB of the switch is not taken into account as well as its impact in terms of noise.

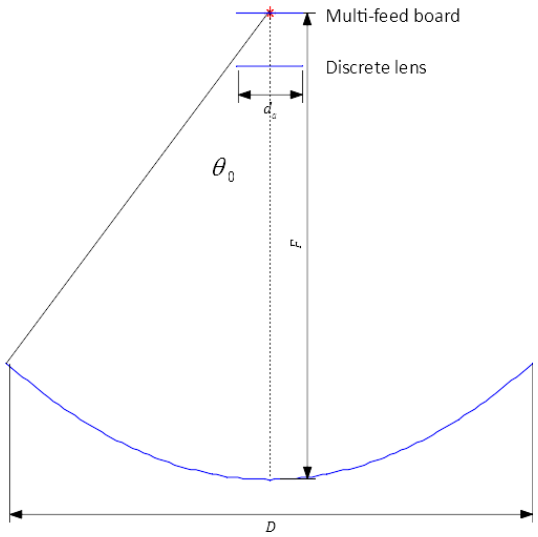

(a)

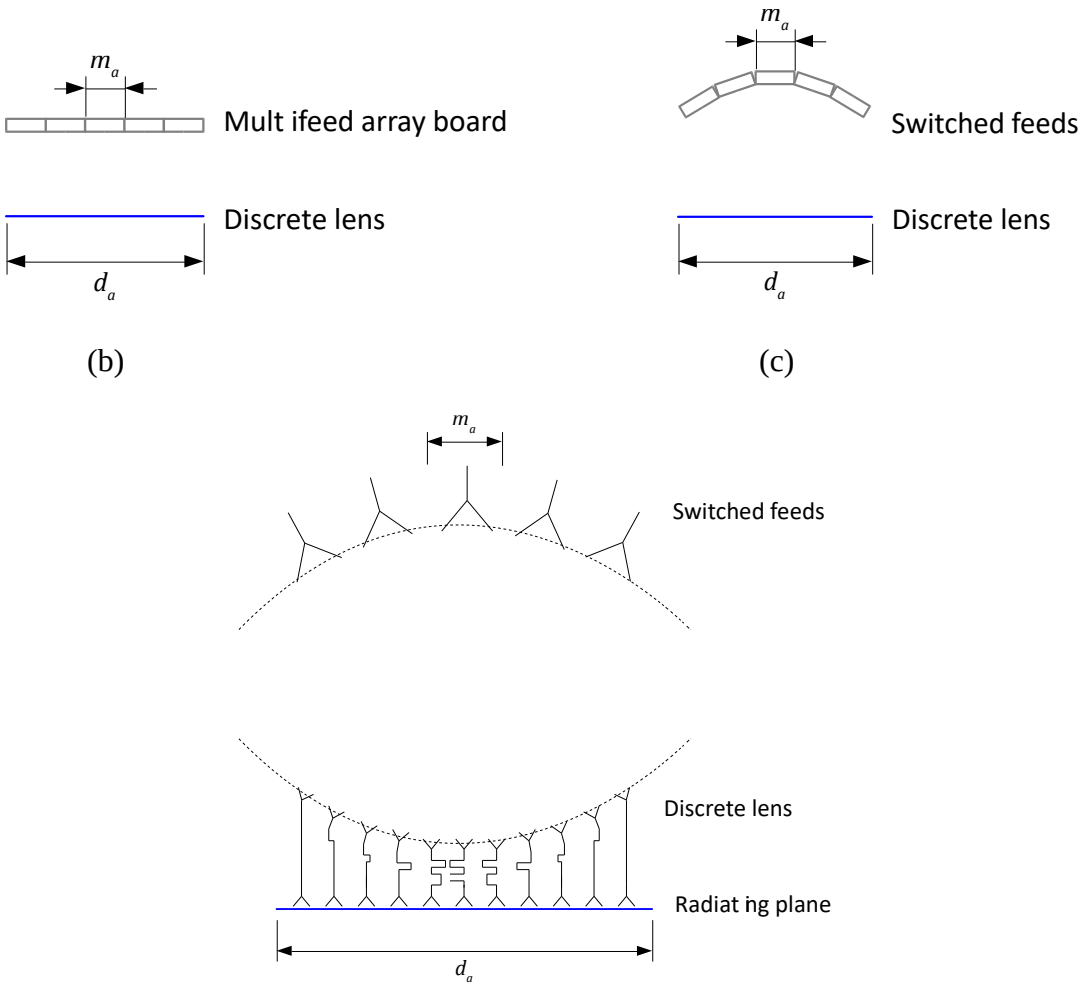

Figure 3-10: Reflector antenna fed with a switched feed discrete lens: a) full antenna geometry; b) discrete lens with switched feed on a planar array; c) discrete lens with switched feeds integrated over a spherical surface; d) discrete lens with feed array: section view of a generic configuration with three degrees of freedom.

The basic design principle for the beam switched planar discrete lens can be explained taking into account the 2-D analysis which is illustrated in **Figure 3-11**. The design procedure should be finalized to the calculations of the phase offset required between each couple of back-to-back antennas. This phase delay, which is implemented by the transmission lines interconnecting the antennas, has to be designed so as the antenna has a specific focal point. Assuming a focal length F, the design can be implemented to have the

lens focal point at F_1 having coordinates in the x-z plane equal to $(-Fsin\theta_0, Fcos\theta_0)$. Calculating the path length between the feed coordinates, each radiating element on the feed side (z=0), and on the radiating size (z= -dielectric height), the phase delay can be calculated for each element of the dielectric lens. When the feed is located at F_1 the lens beam can thus point towards θ_B. The higher degree of freedom of this configuration relies on the possibility to customize the value of θ_B and, in turn, the beam deviation factor. In such a way, it is possible to obtain larger values of the inter-feed distance thus allowing an easier integration of the MMIC. It is worth noticing that this effect is limited by the off-axis gain of the radiating elements which constitute the discrete lens.

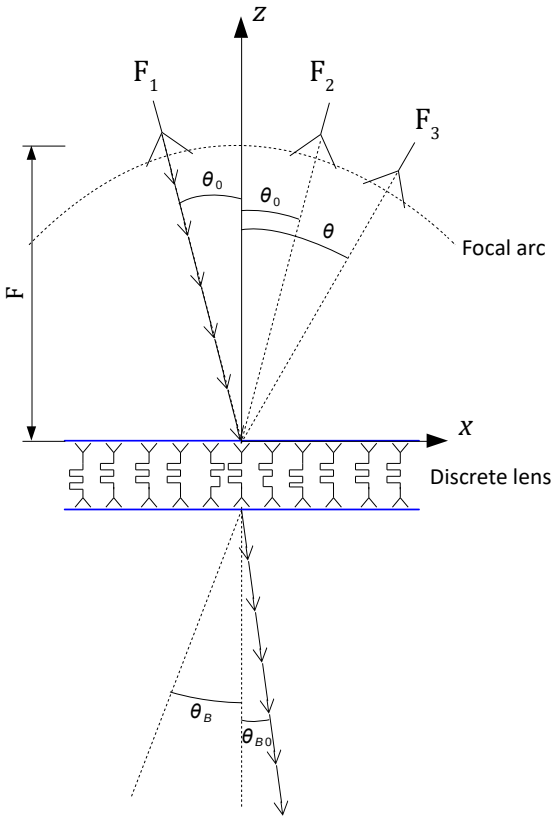

Figure 3-11: Multi-focal discrete lens: section view

It is worth noticing that there are only four focal points, which provide an ideal response of the lens. In the figure, it is shown F_1 and F_2 being the other two ones symmetrically located in the z-y axis. When fed at F_2, the lens beam points towards $-\theta_B$. Feeding points located between F_1 and F_2 will generate beams pointing between $\pm\theta_B$. An arbitrary feed point, F_3, will see the lens element as there was a path length error in the transmission lines interconnecting the internal and external radiator. This error will generate a distortion of the radiation pattern. The focal arc is the surface where the RMS of this path error is minimized. For $\theta_0 = \theta_B$, it can be calculated as [81]:

$$G(\theta, \theta_0) = \sec(\theta_0)\, F\left[1 + \frac{\sin^2 \alpha \sin^2 \theta}{2(1 - \sec \alpha)(1 + \sin \alpha \sin \theta)}\right] \tag{3}$$

where $\alpha = \sin^{-1}(d_a/2F)$. An example of an ideal focal arc is reported in **Figure 3-12**. As it can be seen, for limited scan angles, the ideal focal arc remains almost flat thus allowing, with minimal errors, the planar approximation as reported in **Figure 3-10**-b.

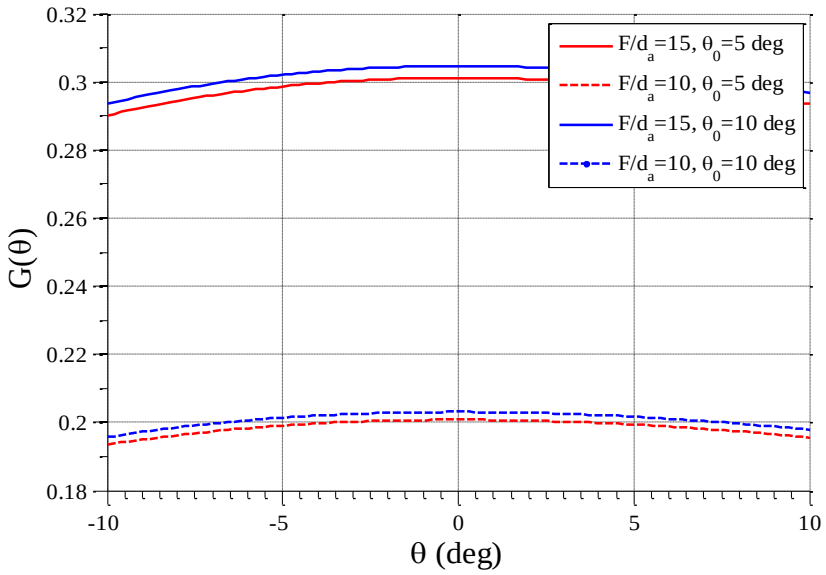

Figure 3-12: Ideal focal arc for different discrete lens configurations. d_a=20 mm, $\theta_0 = \theta_B$

This type of antenna suffers from several loss factors. Losses in the lens, including the losses of the transmission lines, depending on the dielectric and on the printed technology. However, they are comparable with what could be found using the other approaches proposed in this chapter. The aperture losses strongly depend on the design choices and affect the feasibility of the entire antenna architecture. They are defined as $\eta_A = \eta_S \times \eta_I$, where η_S and η_I are the spillover and the illumination efficiency, respectively. In general, η_S and η_I are complementary to each other because η_S increases as the feed becomes more directive while η_I decreases. It can be shown that for a circular lens with F/d_a=1 the maximum of η_A can be achieved when the feed directivity corresponds to $\cos^q \theta$ with q=10. The use of a beam-switching discrete lens can be seen as an alternative to the PAFR or to the reflectarray-fed reflector. It is worth noticing that the beam scanning properties of a reflector fed with this system should be expected to be slightly degraded with respect to the PAFR and reflectarray feed case. Indeed, in the case of discrete lens feed, it is impossible to satisfy the conditions reported in equations (1) and (2) for different pointing directions of the reflector beam. The dimensional analysis regarding the lens aperture size, d_a , is similar to these two cases. The main difference is that in the discrete lens configuration the spacing between the feeding elements can be adjusted through the design of the bi-focal configuration described previously.

3.2.6 Confocal reflectors

An alternative configuration presented in this section is the confocal reflector antenna [83] shown in **Figure 3-13**.

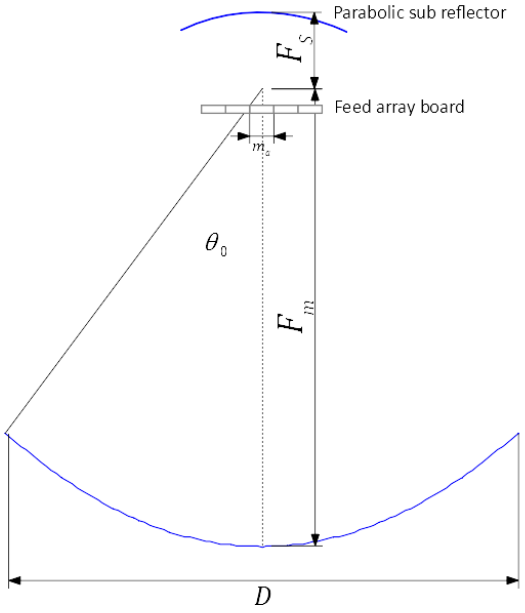

(a)

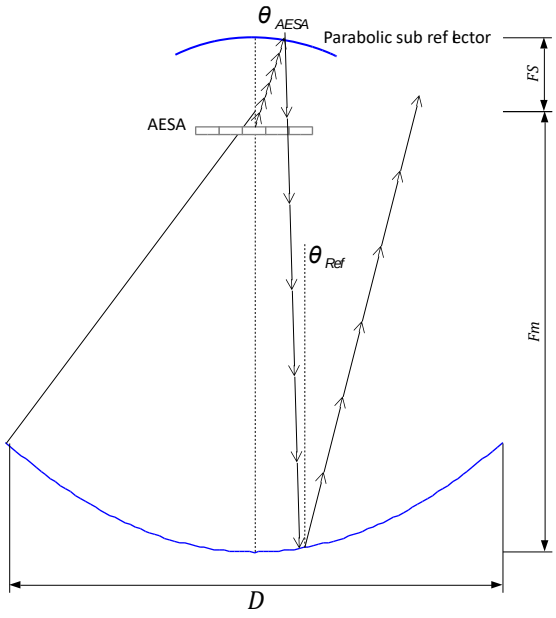

(b)

Figure 3-13: a) Geometry of the confocal reflector antenna; b) basic radiation principle: AESA feed

The confocal architecture makes use of two parabolic reflectors with two focal lengths, namely F_M and F_S for the main and sub-reflector respectively. The pair of parabolas are

confocal, i.e. they share the focal location and they are usually off-set. In Tx mode, the sub-reflector is illuminated by an array feed which can be an AESA or any other beam scanning array such as a discrete lens. The sub-reflector magnifies the received field reflecting it towards the main parabola which in turn generates the main radiation. The magnification factor, M, defined as $M = F_M/F_S$ is a key parameter for this type of antenna. Typically, M ranges between 5 and 15 resulting in a magnification of the feed. Essentially, the gain (or the directivity) of the feeding element is increased by a factor equal to M^2. The main advantage of this configuration is related to the possibility to simplify the feed architecture by reducing its number of elements. This configuration is less used in space or terrestrial applications as the overall antenna height is higher than the corresponding Cassegrain solution. Nevertheless, for the case at hand, its inherent scan compression is considered as an essential advantage. Indeed, when the AESA feed is scanned of an angle θ_{AESA}, the beam radiated by the main reflector will be scanned by an angle θ_{Ref} which is typically equal to θ_{AESA}/M. This architecture could be used in conjunction with a discrete lens having two degrees of freedom in the overall antenna design: i) the beam scanning in the feed can be reduced increasing the magnification of the confocal reflector; ii) the spacing between the feeds of the discrete lens can be increased applying the bi-focal design approach described in the previous section.

3.3 Antenna solutions: comparison

The preliminary study conducted in this work has analyzed, at different levels, some of the possible approaches which can be taken into account to design a beam scanning reflector antenna for E-band applications. The study has mainly taken into account the

dimensional feasibility of each configuration based on the system requirements. A summary of the results of this study is reported in **Table 3-2**.

N	Configuration	Pros'	Cons'
1	PAFR	Highest degrees of freedom in the beam control	Complex architecture Integration feasibility High losses
2	Reflectarray fed reflector	Highest degrees of freedom in the beam control	Complexity of the integration is similar to PAFR The architecture is simpler than PAFR Combining/Dividing losses are reduced
3	Beam switched reflector	Simple architecture of the feed	Integration is limited by the MMIC size
4	Beam switched Cassegrain	Simple architecture of the feed	Integration is limited by the required feed directivity
5	Reflector with beam switching discrete lens	The integration space can be controlled by design	The control on the feed radiated beam is limited and its effect on the reflector should be verified
6	Confocal reflector	An alternative to be combined with Solution 1 or 5	Full-scale simulations required to validate the reflector patterns

Table 3-2: Pros and Cons for each antenna configuration

Solutions 1 and 2 allow the highest level of control of the feed pattern as, in both cases, the amplitude and the phase of each element of the array can be controlled. The integration at the limits of the feasibility and it requires further investigations. The use of flip-chip bonding instead of wire bonding will reduce the overall area occupied by the integrated MMIC. Beam switched reflectors implemented by means of lateral movements of the feed are a valid solution considering either single reflector or Cassegrain designs. In the first case, the integration is limited by the MMIC size while in the second case the limit is due to the directivity required for each feed which would create overlaps. A possible integration approach for the feed of the single reflector has been proposed. This solution can be further improved by modifying the MMIC architecture to embed a switching stage. In such a case, each MMIC could serve more than one feed location thus significantly improving the manifold layout. The use of a superstrate layer has been proposed to increase the directivity of each feed in a printed arrangement. In Solution 5, the beam switched discrete lens, is proposed as an alternative to AESA feeds. In this configuration, the distance between the feeds can be controlled by design thus allowing an optimization of the layout and a simplification of the integration. It is worth noticing that the discrete lens could be employed as a reflector feed but also as a self-standing radiator. The confocal configuration, to be designed in off-set configuration, offers an additional degree of freedom in combination with an AESA or with a beam-switching discrete lens.

CHAPTER 4

E-BAND BEAM SWITCHED CASSEGRAIN REFLECTOR ANTENNA

4.1 Proposed solution

The activities concerning antennas encompass the practical application to radiating structures of the transceiving chip. The envisioned chip architecture allows freedom in controlling both amplitude and phase of the transmitted or received RF signal. As a natural consequence, the chip becomes a basic component in a multi-antenna structure, which can then provide beam-scanning/forming/switching capabilities. The rationale for such desire is the very large directivity required by modern 80 GHz backhauling links, which in turn involves extremely narrow beamwidths and hence cause issues of alignment and tracking of the remote site. An analytical model has been developed and used to analyze the statistical availability of practical links. The outcome has shown how current solutions (without beam tracking) are severely hampered by thermal deformations of the masts and thus may not benefit from even larger antennas. Besides, the devised model has also been used to estimate the effect of a beam-tracking system: larger antennas can be used and their thermal deformations compensated for, hence allowing longer hops. A number of requirements for a beam-tracking system have therefore been drafted in the previous chapter, concerning the maximum angle to be scanned, tracking speed, allowed scan loss, and angular uncertainties. Based on such requirements several solutions have been

considered and compared, roughly summarizable as a large direct-radiating phased array with the same total EIRP, single- and double-reflector configurations fed by a small phased-array, single- and double-reflector configurations fed by a small switched-beam radiator. The former would require an excessive number of chips and a consequently huge DC power consumption; the latter two solutions instead allow to exploit the large gain of a reflecting dish while confining the control part to a small feed. Among these, the switched-beam solution has been chosen for its lower density of radiating elements, sufficient to accommodate an underlying array of TRX chips working only one at a time. The next steps will involve a proof of concept applied to a custom dish.

As a proof of concept, the E-band dies are intended to be integrated on a feed-array reflector antenna providing multi-beam or switched beam operation. Different antenna configurations have been analyzed and a multi-feed Cassegrain reflector has been identified as the ideal antenna to validate the proposed concept. An array of switched feed points towards the sub-reflector which reflects the beam to the main reflector. A lateral displacement of the feed, m_a, results in a squint of the main reflector beam at an angle θ. The proposed antenna concept is shown in **Figure 4-1**: a parabolic main reflector is illuminated through a secondary reflector, which is in turn fed through an array of feeds. The distance between the feeds, m_a, allows the generation of a tilt in the beam whose characteristics are proportional to the feed offset. Therefore, the integration of each feed of the board with a MMIC generates multiple beams within an offset compatible with the targeted applications, i.e. +/- 1 degree.

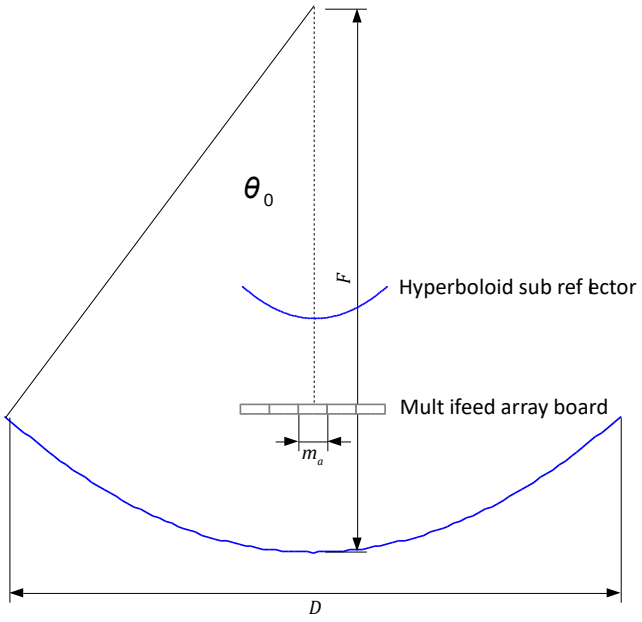

Figure 4-1: Multi-feed Cassegrain reflector antenna concept

4.2 Antenna requirements

The main requirements of the antenna, shown in **Table 4-1**, are related to the possibility to reconfigure the beam compensating small boom movements, which are estimated to be within ±1° in both azimuth and elevation planes.

Requirement	Value
Frequency range	71-76 GHz
	81-86 GHz
Steering range	±1°
Gain	50 dBi
Polarization	Linear

Table 4-1: Main antenna requirements

To satisfy all the antenna specifications, the work has been organized in this way:

1. Estimation of the feed unit cell size;
2. Primary feed selection;

3. Primary feed test in Cassegrain configuration;

4.3 Estimation of the feed unit cell size

As first step, several simulations have been performed using TICRA Grasp [78] to define the unit cell dimension m_a of the Cassegrain antenna. The configuration used in TICRA Grasp is presented in **Figure 4-2**; a horn antenna has been taken as reference antenna and has been evaluated in Cassegrain configuration considering these parameters:

- Diameter of the parabolic reflector=90 cm (D=90 cm);
- Subreflector eccentricity=1.7 (Ecc=1.7);
- Focal distance=22.5 cm (F=22.5 cm);
- Interfocal distance=15.7 cm (IF=15.7 cm);
- IF/F=0.7;
- F/D=0.25;

The unit cell dimension is linked to the steering specification presented in **Table 4-1**, in the final prototype the main beam of the reflector can thus be tilted from broadside by activating different elements of the feed array of the Cassegrain antenna.

In this preliminary phase, the main beam will be tilted by moving a horn antenna in azimuth and elevation planes. A double reflector system has been taken into account considering a parabolic main reflector with D=90 cm and a hyperbolic sub-reflector with an eccentricity=1.7; the focal distance is F=22.5 cm. The horn antenna was placed at a distance of IF=15.7 cm from the focal point.

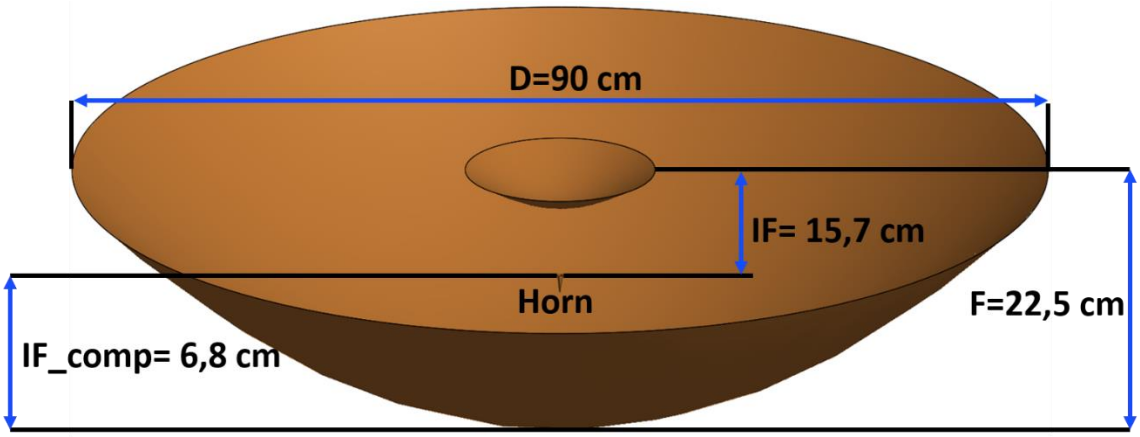

Figure 4-2: Preliminary Cassegrain configuration for defining the unit cell size

To provide the requested steering of ±1°, the reference horn antenna should be moved of 15.3 mm from the reference position, thus providing a steering angle of ±0.96°. Once delineated the maximum displacement in order to fulfill the steering specification, it is necessary to define the number of elements that will create the final feeding element that will feed the beam-switched Cassegrain reflector antenna that will meet all the design specifications. For instance, if we want to realize an array 3x3 of feeding elements, the unit cell dimension will be m_a= 15.3 mm and every cell will be capable to provide a steering of $\theta_B = \pm 0.96°$, where θ_B is the squint of the main beam. For an array 5x5, it is necessary to use a unit cell size of m_a= 7.65 mm, thus providing a steering of $\theta_B = \pm 0.5°$. For an array 7x7, the unit cell size will be 5.1 mm and the provided squint angle will be equal to $\theta_B = \pm 0.33°$. For an array 9x9, the unit cell size will have a steering angle of $\theta_B = \pm 0.25°$ with a dimension of m_a= 3.83 mm. All the proposed solutions are summarized in **Figure 4-3**.

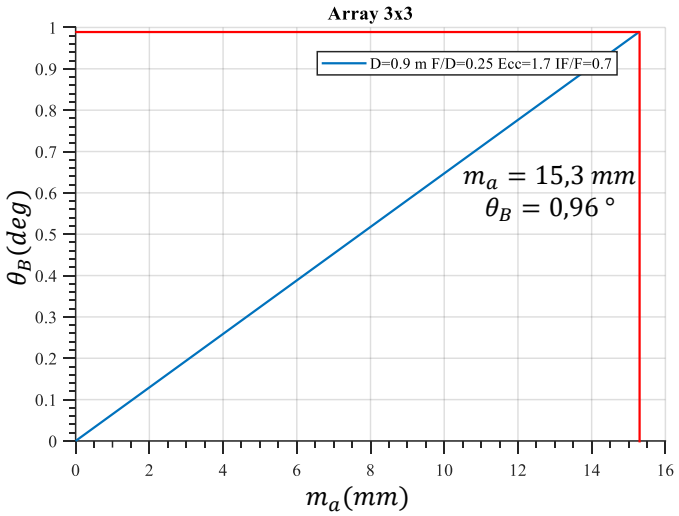
Array 3x3
D=0.9 m F/D=0.25 Ecc=1.7 IF/F=0.7
$m_a = 15{,}3\ mm$
$\theta_B = 0{,}96\ °$
$\theta_B(deg)$
$m_a(mm)$

(a)

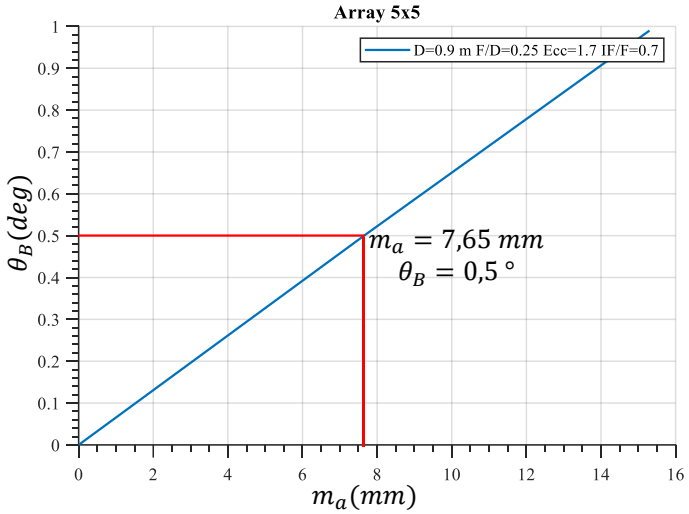
Array 5x5
D=0.9 m F/D=0.25 Ecc=1.7 IF/F=0.7
$m_a = 7{,}65\ mm$
$\theta_B = 0{,}5\ °$
$\theta_B(deg)$
$m_a(mm)$

(b)

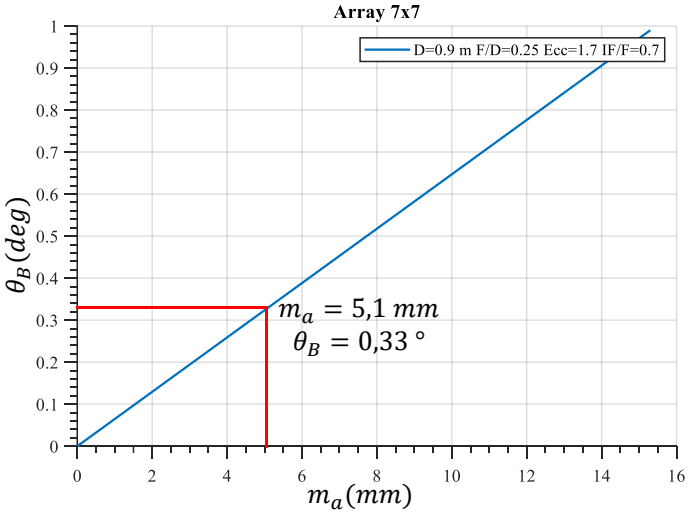
Array 7x7
D=0.9 m F/D=0.25 Ecc=1.7 IF/F=0.7
$m_a = 5{,}1\ mm$
$\theta_B = 0{,}33\ °$
$\theta_B(deg)$
$m_a(mm)$

(c)

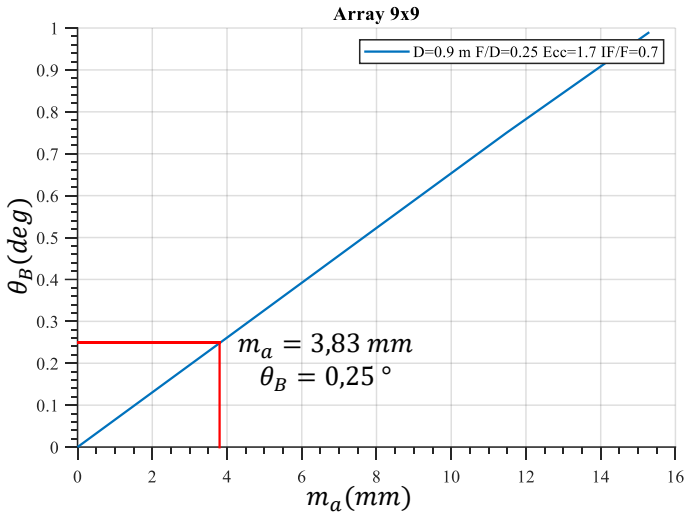

(d)

Figure 4-3: a) Unit cell dimension m_a considering an array 3x3 b) Unit cell dimension m_a considering an array 5x5 c) Unit cell dimension m_a considering an array 7x7 d) Unit cell dimension m_a considering an array 9x9

The first (**Figure 4-3**-a) and second (**Figure 4-3**-b) configurations have been discarded because they lack in terms of resolution of phase of beam-steering; the first directly provides the requested steering and it doesn't take into account other intermediate values, while in the second, the phase resolution is limited only to three values that is to say: 0 degrees, 0.5 degrees and 0.96 degrees.

The third (**Figure 4-3**-c) and the fourth (**Figure 4-3**-d) configurations are very similar, especially in terms of phase resolution, in fact, they provide a similar squint per unit cell, 0.33 degrees the third and 0.25 degrees the latter. By looking forward to the final prototype that will feed the Cassegrain reflector antenna, it is necessary to evaluate other parameters and not only the phase resolution of the beam-steering.

A key parameter is the unit cell dimension for the feeding network. For example, in the case of an array 7x7, the unit cell dimension will be 5.1 mm. For an array 9x9, the cell will

be 3.65 mm. As stated before, the first two configurations have been discarded because they lack in terms of phase resolution for beam-steering.

In the case of an array 9x9, with m_a=3,65 mm, the space will be very restricted for the feeding network, nevertheless, other parameters such as mutual coupling must be taken into account and the reduced intracell space can cause this kind of problem.

A good balance, in terms of phase resolution, for beam-steering and unit cell dimension for the feeding network, can be fulfilled with an array 7x7. Thus the unit cell size has been set to m_a =5.1 mm and so an array 7x7 of feeding elements will feed the final reflector Cassegrain antenna, to realize a beam switched antenna.

The effect of the feed directivity has been evaluated in TICRA Grasp using a horn as reference antenna, as shown in **Figure 4-2**, with the following parameters:

- Taper=-12 dB;
- Taper angle= 29.068910408117°;
- Polarization: Linear

The results obtained with the reference horn are shown in **Figure 4-4**.

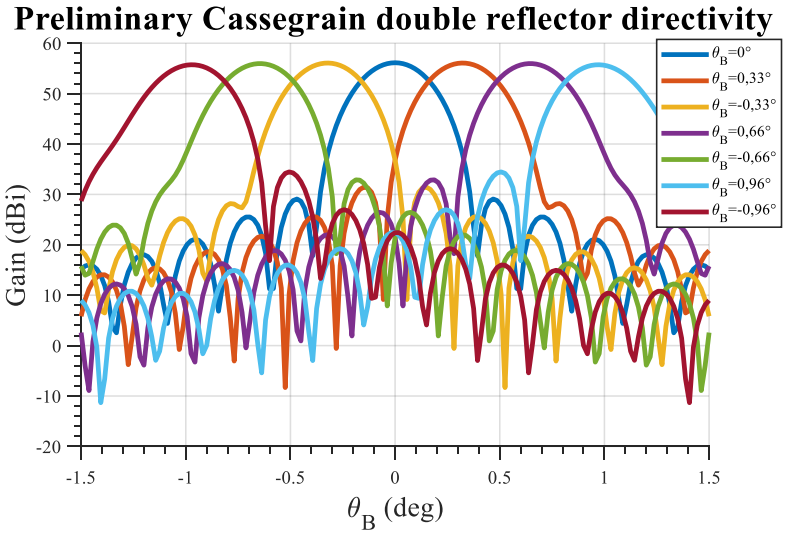

Figure 4-4: Preliminary Cassegrain double reflector with a horn as reference antenna at @77 GHz

In **Figure 4-4** are presented the results obtained with a reference horn antenna in a Cassegrain configuration. The average gain obtained in this configuration is 56 dBi. In the reference position the peak gain is 56.12 dBi; at 0.33 degrees of steering, the peak gain is 56 dBi; at 0.66 degrees is 55.95 dBi and at 0.96 degrees the peak gain is 55.66 dBi. As can be seen, the squint of the main beam does not have relevant effects, in terms of the gain, on the other configurations with respect to the reference case, where the antenna is placed at the reference position. In fact, the maximum losses are estimated in a range of 0.5 dB with respect to the reference case. At the same time, the side lobe level is good in every configuration and it goes from -27 dB, for the reference case, to -22 dB for the case where is realized the maximum steering, that is to say, 0.96 degrees. By considering the design specifications listed in **Table 4-1**, a horn antenna in a Cassegrain configuration can give a good balance in terms of gain and steering specifications. In the following section will be discussed different feeding elements which will be suited for the Cassegrain antenna, in order to realize a beam switched antenna and which will satisfy all the design specifications.

4.4 Primary feed selection

In the primary feed selection choice have been taken into account different parameters, in fact, as discussed in Chapter 2, several antennas can be suited for backhauling purpose for 5G mm-wave frequencies. The primary feed choice can involve from the simple microstrip antenna, such as a patch antenna, to the most complex antenna, such as magneto-electric dipole antenna. The selection of the feeding element is based mainly on the design specifications.

4.4.1 Magneto-electric dipole

For the case at hand as primary feed, a magneto-electric dipole has been selected. Magneto-electric dipole is a complementary antenna, in which a planar electric dipole is combined with a vertically planar shorted magnetic dipole. This kind of antenna is well known in literature for owning wide bandwidth, superior radiation performance, high gain, and a simple structure as well. The two vertical metallic walls, which operate as a magnetic dipole, and the portion of the ground plane connecting the two walls together, that is to say, the electric dipole can be interpreted as a vertically oriented thick quarter-wave patch antenna, which has a ground plane size identical to the patch size. The principle of operation of the magneto-electric dipole is shown in **Figure 4-5**. The height of the basic magneto-electric dipole is about 0.25 λ_g, referring to the center wavelength. For low-profile design, the vertical walls of the antenna can be folded without affecting the antenna performance too much [68]. From a technological point of view, this type of antenna was not originally conceived for integration in PCB structures. Only one decade ago [84], it has been demonstrated how this type of radiator can be effectively integrated into a standard multi-layer PCB for mm-wave applications.

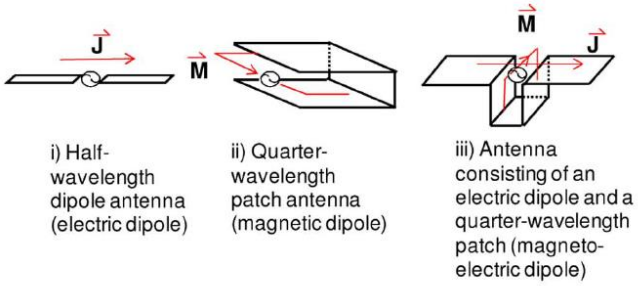

Figure 4-5: Principle of operation of Magneto-electric dipole [84]

The combination of the radiation properties of the electric dipole and of the magnetic dipole, and so of the magneto-electric dipole, are shown in **Figure 4-6**. As can be noticed, the electric dipole presents an '8'-shaped radiation pattern on the E-plane and an omnidirectional radiation pattern on the H-plane. On the other hand, the magnetic dipole shows a complementary behavior, which means an '8'-shaped radiation pattern in the H-plane and an omnidirectional radiation pattern in the E-plane. As a magnetic dipole and an electric dipole are excited simultaneously, a ME dipole is achieved. The radiation pattern of the ME dipole is a combination of the patterns of a magnetic dipole and an electric dipole. By compounding a y-aligned electric dipole and an x-aligned magnetic dipole, the forward radiation of the ME dipole is reinforced, whereas the back-radiation is reduced. Therefore, the identical heart-shaped radiation patterns of the E- and H-plane shown in **Figure 4-6** are achieved [85].

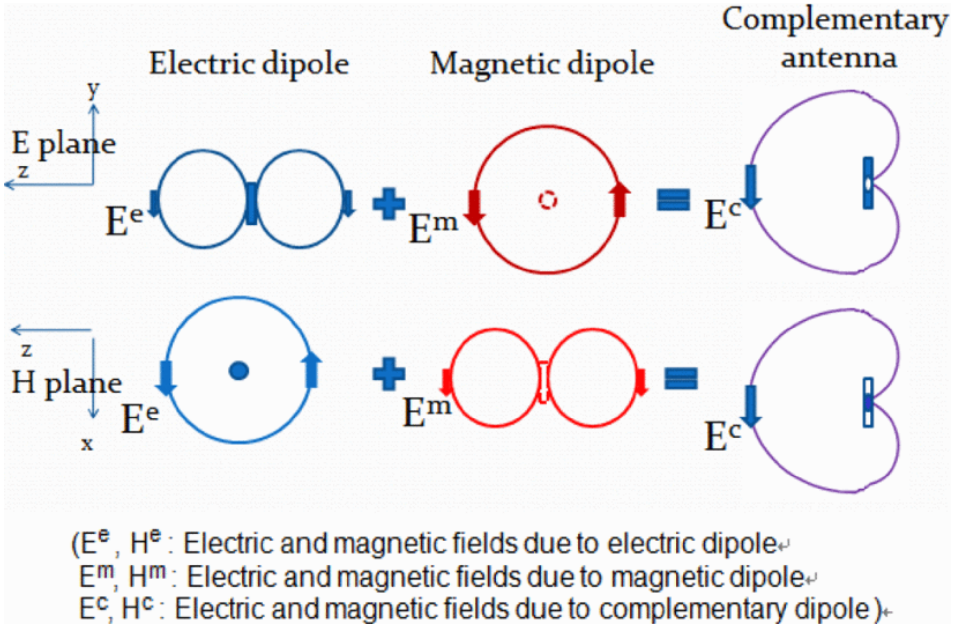

Figure 4-6: Synthesis of the Magneto-electric dipole patterns [68]

The compound electric field of the ME dipole in the far-field can be expressed as follows:

$$\vec{E} = j\frac{E_y dxdy}{2\lambda r}[e_\theta \sin\varphi\,(1+\cos\theta) + e_\varphi \cos\varphi(1+\cos\theta)]e^{-jkr} \quad (4)$$

$$F(\theta) = \frac{(1+\cos\theta)}{2} \quad (5)$$

According to (5), when θ = 180°, F(θ) = 0, which shows that the magneto-electric dipole has a low back lobe. In the last few years, thanks to the research advances in the ME integration on PCB, several examples of printed ME dipole have been proposed in literature by varying the shape of the radiating elements or by using different feeding configurations [86].

For the case at hand, a substrate integrated waveguide (SIW) fed aperture-coupled magneto-electric dipole has been proposed. The antenna consists of two PCB laminates as shown in **Figure 4-7**, in particular, two Rogers 3003 PCB laminates with a thickness of 0.5 mm and a relative permittivity of 3 are used, detailed dimensions of the antenna are illustrated in **Figure 4-8**. The whole ME dipole structure is built in Substrate 2. A pair of horizontal planar dipoles composed of four identical metallic patch sections are printed on the top surface of Substrate 1. Each patch is connected to the ground through a vertical metallic via.

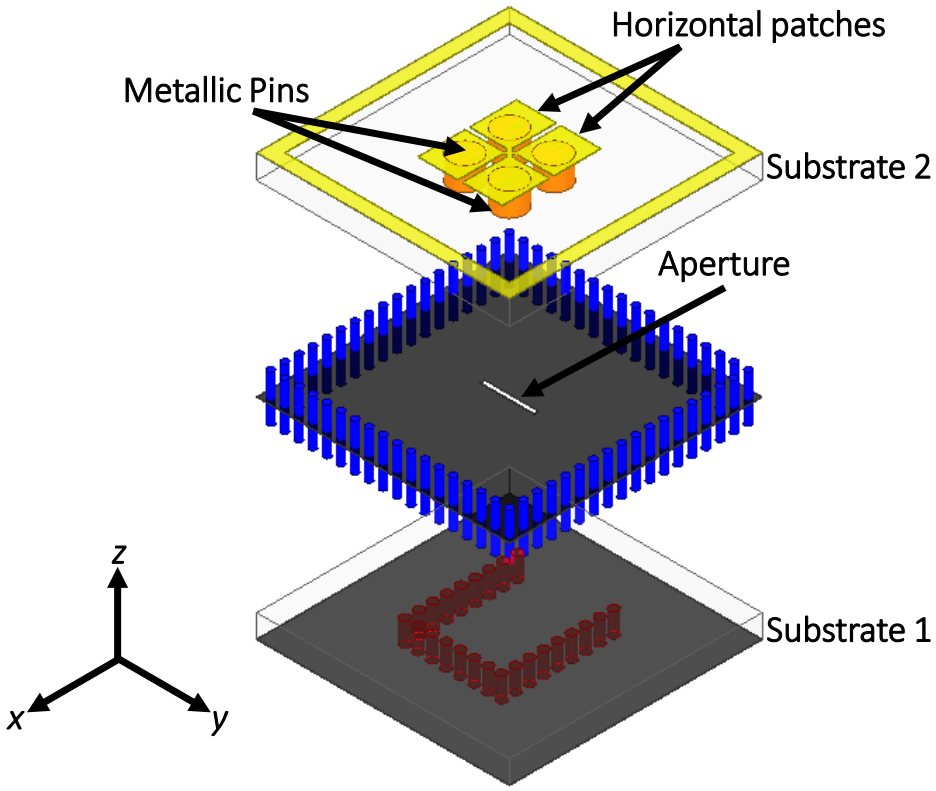

Figure 4-7: Geometry of the SIW-fed aperture coupled ME-dipole antenna

Most of ME-dipoles present in literature are fed using a L-probe [87], and by using a coupling aperture instead of a L-shaped probe is difficult to achieve a good impedance matching. As stated in [49], by using a crossed strip located at the center of the antenna, added to connect the inner corners of the four patches of the ME-dipole together, is possible to solve the issue and to tune the impedance matching and, as a result, to have a good impedance matching. The antenna is excited by a slot; this aperture is etched on the top copper-clad surface of Substrate 1. A shorted-end section of a SIW with input port 1 is constructed in Substrate 1 to feed the aperture. The width of the SIW a is chosen as 2.06 mm to guarantee that over the operating band, the SIW supports only the dominant mode and also is far away from the cut-off frequency. The diameter of the vias composing each

SIW is 0.2 mm. The size of the metallic ground plane is 5.4 mm×5.4 mm. The idea of the ME dipole is to combine a magnetic and an electric dipole together to get a symmetrically unidirectional radiation pattern with low back radiation. In this design, the electric dipole is realized by the pair of patches printed on the top surface of Substrate 2, and the magnetic dipole, which in general is presented as vertical walls of the shorted patch antenna, is represented by four vertical metallic vias.

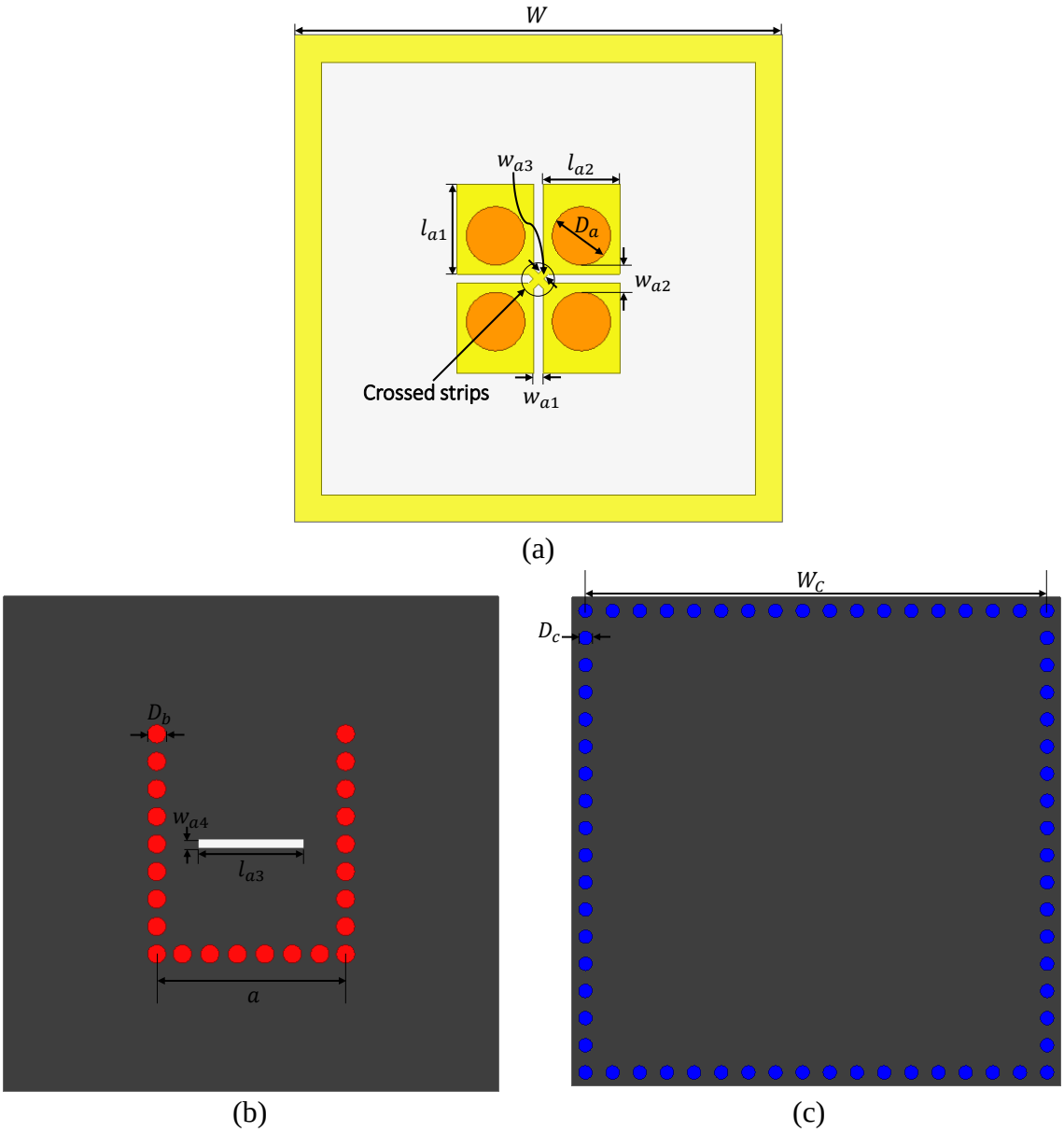

Figure 4-8: Top views of the proposed ME-dipole

The antenna has been simulated and designed with the assistance of a full-wave electromagnetic solver Ansoft HFSS [88]. The simulated current distributions, in the proposed aperture-coupled ME-dipole antenna, are shown in **Figure 4-9**. As can be noticed, at time $t = 0$ and $^{T}/_{2}$, where T is a period of time, the current on the inner edges of the horizontal patches is dominant, which indicates that the two quarter-wavelength apertures, that is to say the equivalent magnetic dipole in *y*-direction, are excited. On the other hand, at time $t = {}^{T}/_{4}$ and $^{3T}/_{4}$, the current is concentrated on the major portion of the horizontal patches, which indicates that the electric dipole in *x*-direction is strongly excited. Therefore, the planar electric dipole and the magnetic dipole are excited alternately with similar strength. As mentioned in [68], [89], the combination of the cross-electric and magnetic dipoles can operate as a complementary antenna, which leads to the desirable unidirectional pattern with low back radiation.

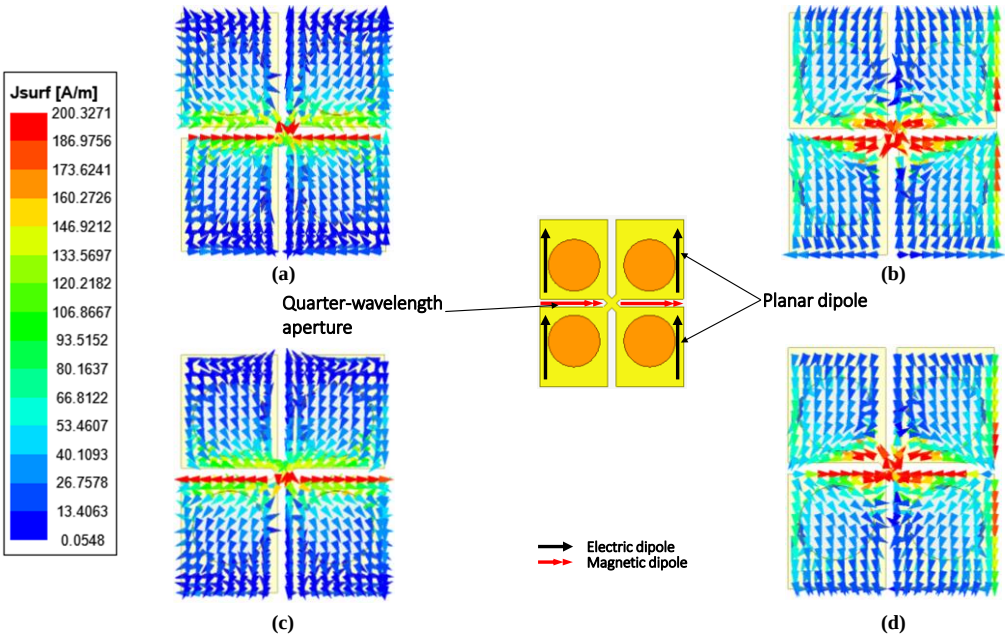

Figure 4-9: Current distributions of the aperture coupled ME-dipole over a period of time: (a) $t = 0$ (b) $t = {}^{T}/_{4}$ (c) $t = {}^{T}/_{2}$ (d) $t = {}^{3T}/_{4}$

The final values of the dimensions of the aperture-coupled ME-dipole antenna working at E-band, that is to say from 71 to 86 GHz, as stated in the design specifications, are listed in **Table 4-2**.

Parameters	W	w_{a1}	w_{a2}	w_{a3}	W_C	l_{a1}	l_{a2}	l_{a3}	D_a	D_b	D_c	a
Values (mm)	5.4	0.1	0.3	0.08	5.1	1	0.85	1.15	0.65	0.2	0.15	2.06

Table 4-2: Dimensions of the SIW fed aperture coupled ME-dipole antenna

The simulated Return Loss of the proposed antenna is shown in **Figure 4-10**. As can be noticed, the antenna presents a good impedance matching which is smaller than -10 dB in the band of interest, that is to say from 71 GHz to 86 GHz, and covers the whole E-band.

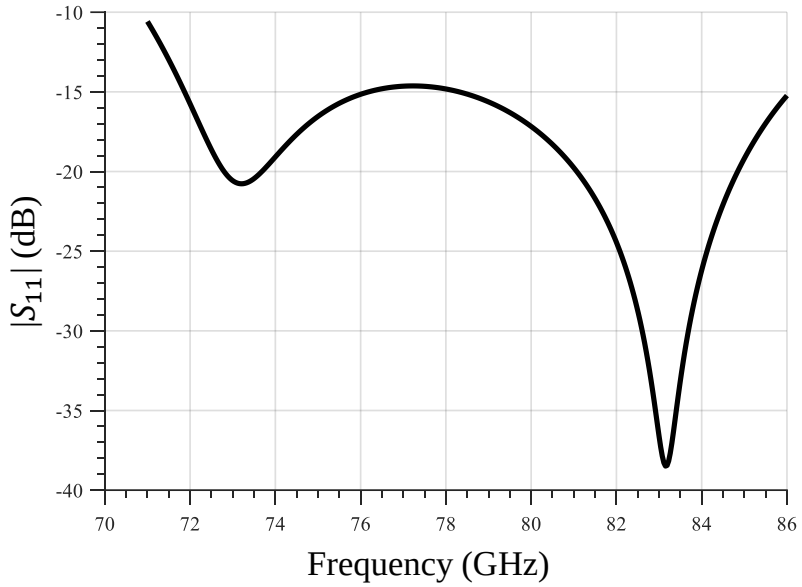

Figure 4-10: Simulated Return loss of the proposed SIW-fed aperture-coupled ME-dipole antenna

In **Figure 4-11** is shown the gain VS frequency response of the proposed antenna, which shows a peak gain of 10.8 dBi at 84 GHz. The 3-dB beamwidth includes all the band of

interest, as stated in the design specifications. In **Figure 4-12** are displayed the Radiation Patterns of the SIW fed aperture coupled ME dipole antenna at 71, 77, and 85 GHz.

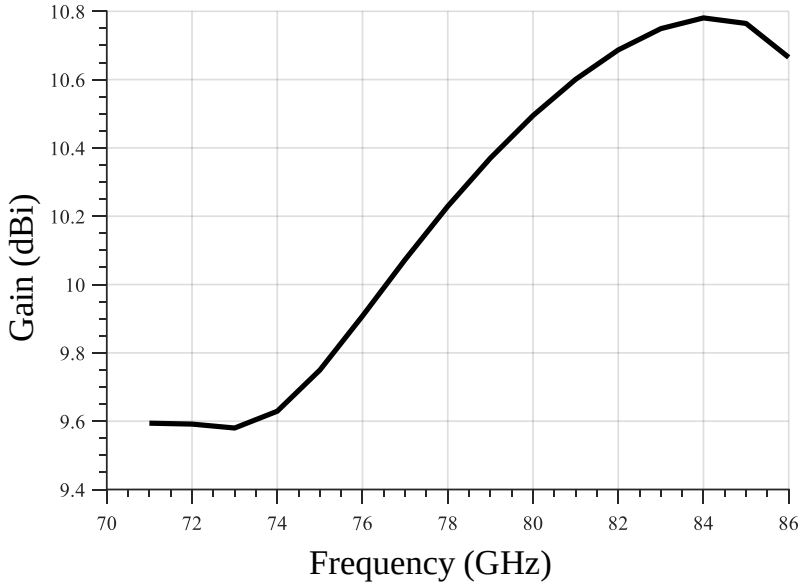

Figure 4-11: Simulated gain VS frequency of the proposed SIW-fed aperture-coupled ME-dipole antenna

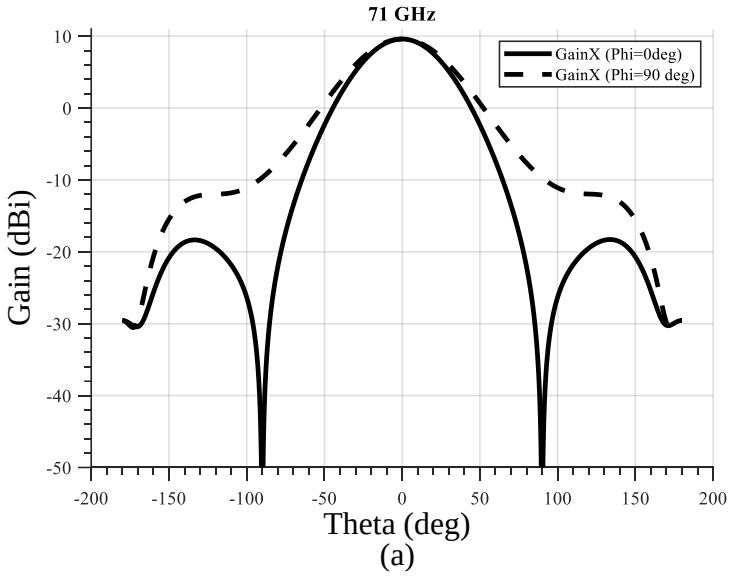

(a)

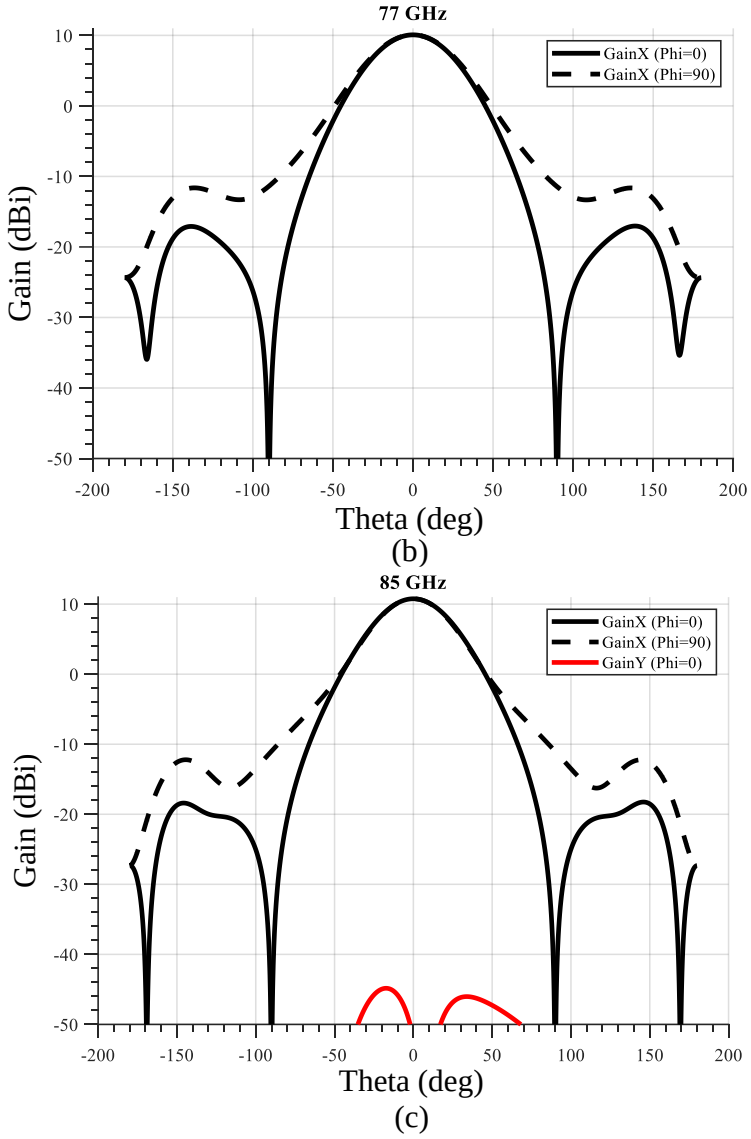

Figure 4-12: Radiation Patterns of the ME dipole at (a) 71 GHz (b) 77 GHz (c) 85 GHz

4.4.2 Butterfly magneto-electric dipole antenna

In this section, a SIW-fed aperture coupled butterfly magneto-electric dipole is presented. The antenna is based on the same operating principle of the ME dipole presented previously, but the introduction of the rhomboid form [90],[91] for the electric dipole flattens and enlarges the impedance matching bandwidth and power up the gain response with respect to the simple SIW-fed aperture coupled ME dipole antenna. The proposed butterfly ME dipole antenna is shown in **Figure 4-13**; the antenna stackup is the same of

the simple ME dipole presented in the previous section, while the detailed dimension are depicted in **Figure 4-14**.

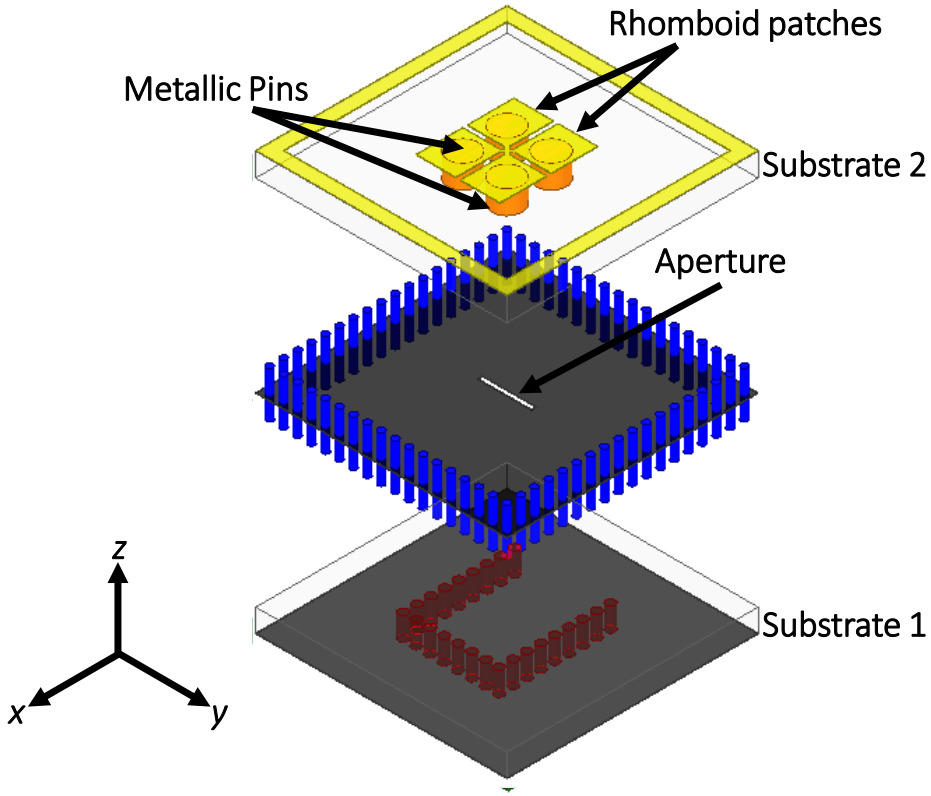

Figure 4-13: Geometry of the SIW-fed aperture coupled butterfly ME-dipole antenna

The final values of the dimensions of the aperture-coupled butterfly ME-dipole antenna working at E-band (71-86 GHz) are listed in **Table 4-3**.

Parameters	W	w_{a1}	w_{a2}	w_{a3}	W_C	l_{a1}	l_{a2}	l_{a3}	D_a	D_b	D_c	a
Values (mm)	5.4	0.285	0.08	0.1	5.1	1.2	1.3	1.15	0.65	0.2	0.15	2.06

Table 4-3: Dimensions of the SIW fed aperture coupled butterfly ME-dipole antenna

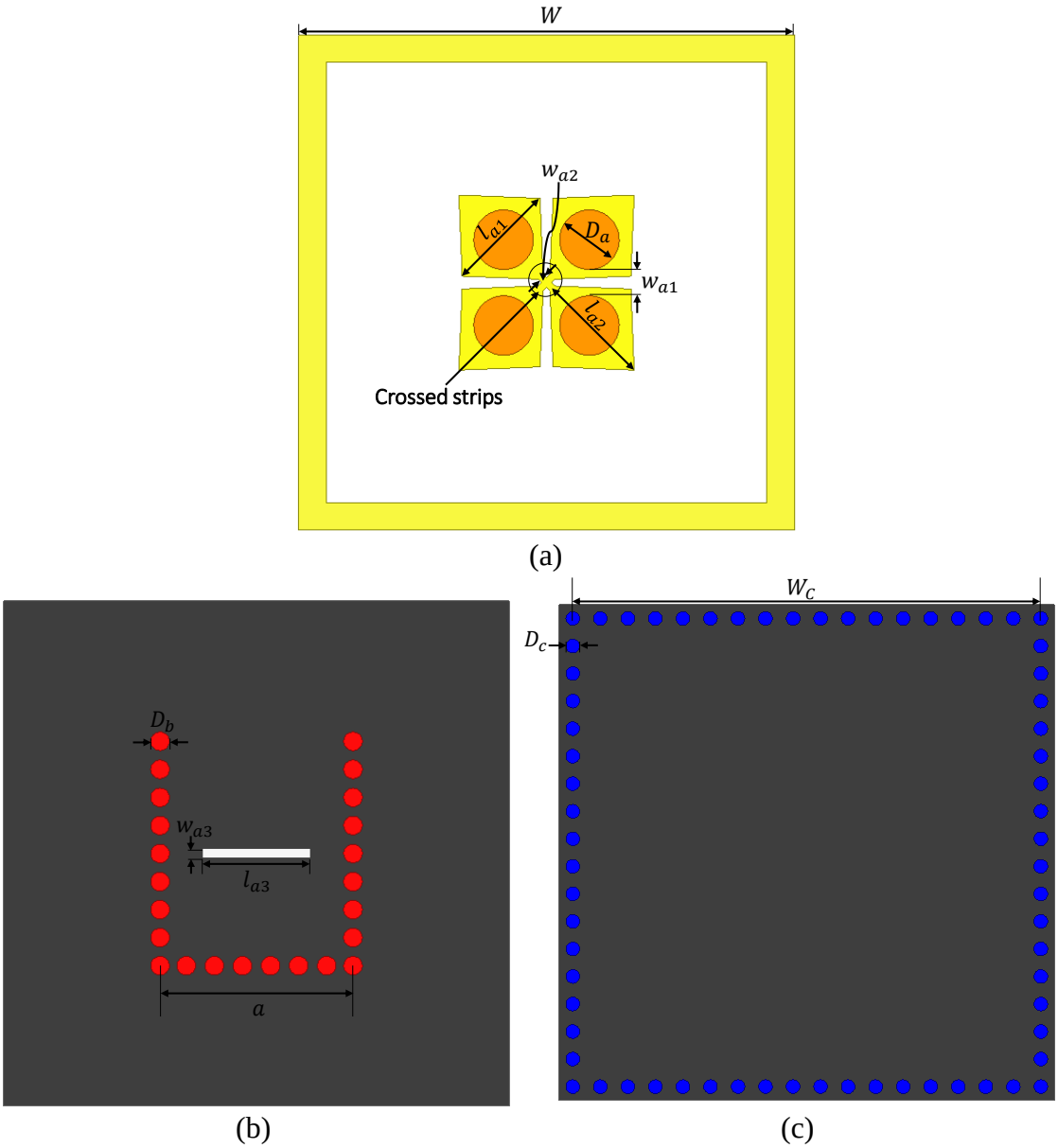

Figure 4-14: Top views of the proposed butterfly ME-dipole

In **Figure 4-15** and **Figure 4-16** are presented respectively the return loss and the gain vs frequency response. As can be observed, with respect to the previous ME dipole configuration, the impedance matching is flattened and enlarged by maintaining a -10 dB level from 72 to 86 GHz and over. In terms of gain by comparing this element to the previous one, the peak gain is 11.1 dBi at 74 GHz and moreover, it is noticeable a power-up of the gain in the first part of the E-band (71-76 GHz); this can be ascribed to the

presence of the rhomboid ME dipole. In **Figure 4-17** are displayed the Radiation Patterns of the SIW fed aperture coupled butterfly ME dipole antenna at 71, 77, and 85 GHz.

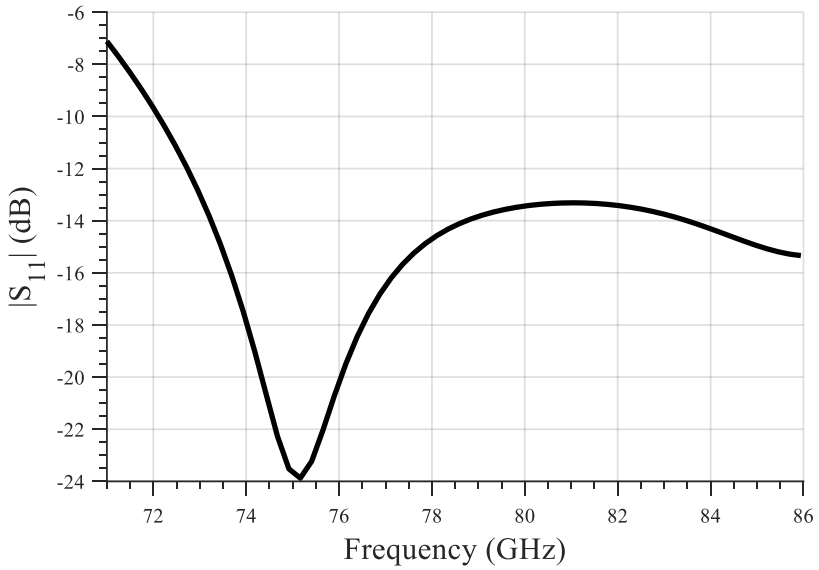

Figure 4-15: Simulated Return loss of the proposed SIW-fed aperture-coupled butterfly ME-dipole antenna

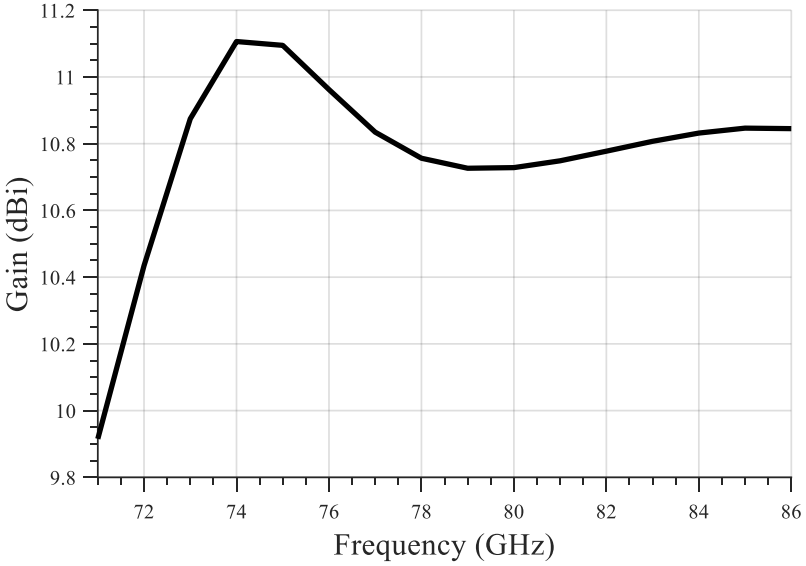

Figure 4-16: Simulated gain VS frequency of the proposed SIW-fed aperture-coupled butterfly ME-dipole antenna

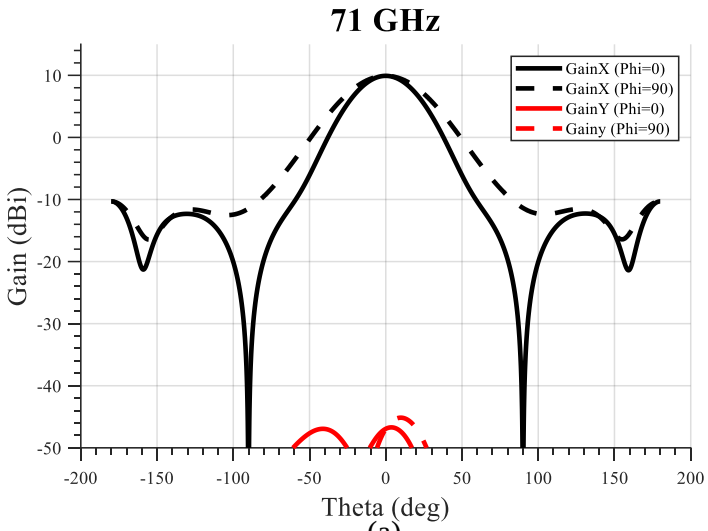

(a)

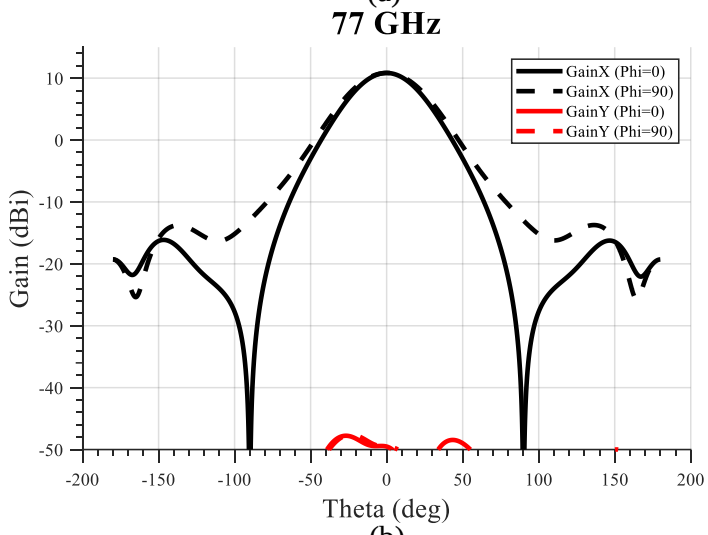

(b)

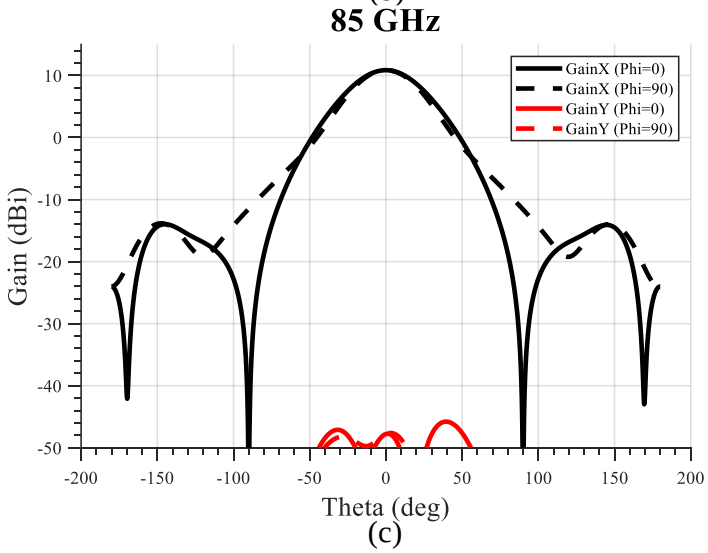

(c)

Figure 4-17: Radiation patterns of the butterfly ME dipole antenna at (a) 71 GHz (b) 77 GHz (c) 85 GHz

4.4.3 Lens antenna

Integrated lens antennas (ILAs) are widely used at mm-waves for various applications such as communication, imaging, and radars. One of the limits of this approach is linked to the height and weight of the lens, which is sometimes incompatible for on-board applications. For this purpose, four techniques have been proposed in literature I order to overcome this issue. The first is linked to the fact of increasing the lens permittivity by using materials such as ceramics, silicon, etc. [92], [93]. This approach poses several problems for the lens, in fact they are lossy, expensive, and difficult to machine; moreover, their larger density does not lead to the reduction of the lens weight. The second technique refers to the optimization of the lens shape in order to reconstruct a required phase wave front at the antenna aperture, while keeping small the lens size and by using lenses with low permittivity index. Nevertheless, this solution leads to complex 3D shapes [94]–[96]. The third approach involves the use of multi-material dielectric lenses and 3D monolithic subwavelength periodic structures with variable permittivity [57], [97], [98]. On the other hand, the corresponding fabrication techniques are very difficult to realize at mm-waves. The fourth and last technique refers to an alternative and low-cost solution which involves the reduction of the lens focal length by introducing an air cavity inside the lens, in this way, there is no need to modify the lens shape or permittivity [59]. By using the last approach, it is possible to have a significant reduction of the size and of the weight of the lens. By introducing an air cavity, it is possible to reduce the focal length of the lens, without modifying the lens shape or change its permittivity. The height of the cavity is very important, because it brings the focus directly on the substrate, where the feeding antenna of the lens is placed [59].

The typical dielectrics used for the lenses for this kind of configuration are: Rexolite, ABS, Polyethylene, Teflon, etc. with low permittivity indexes which vary from 2.1 to 2.53. In this section, as possible feeding element for the Cassegrain antenna, a lens antenna is proposed. The antenna concept will follow the fourth approach presented previously, so a lens antenna with an air cavity will be used in order to reduce the size and the weight of the lens. Moreover, as feeding element of the lens, a SIW-fed aperture coupled ME-dipole antenna will be employed. The use of this radiating element is a novelty because in literature is possible to find several applications with slot and patch antennas as primary feeding element of the lens [54], [99]. The proposed integrated lens antenna is shown in **Figure 4-18**.

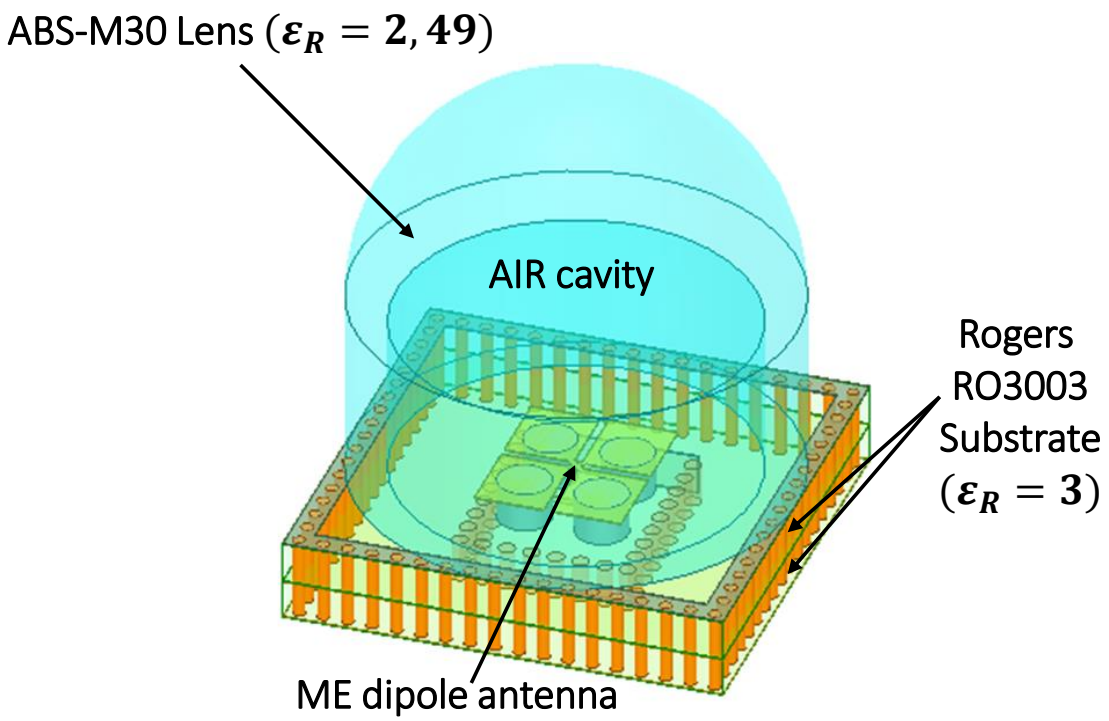

Figure 4-18: Proposed integrated lens antenna

The lens is made in ABS M-30 ($\varepsilon_L = 2.49$), which is a plastic material typically used for 3D printers, in fact this material has been selected to print the lens with a 3D printer. The lens has an extended hemispherical form, with a diameter $\theta_L = 5.4\,mm \approx {}^{4\lambda_0}/_{3}$ ($R_L = \theta_L/2 = 2.7\,mm$) with $f_0 = 77\,GHz$. L is the lens extension, h is the air cavity height and θ_A is the air cavity diameter ($\theta_A = 4.4\,mm$). If the height of the air cavity is properly selected, it brings the focal point directly in the substrate. The reciprocity principle says that the best broadside directivity for a reduced size integrated lens antenna will be achieved when $(h + L) \sim F$, where F is the focal length of the lens. Some displacement may appear due to the finite size of the lens and primary feed [59]. h is set to 2 mm and L=0.36 mm.

All the parameters and the geometry of the lens are shown in **Figure 4-19**.

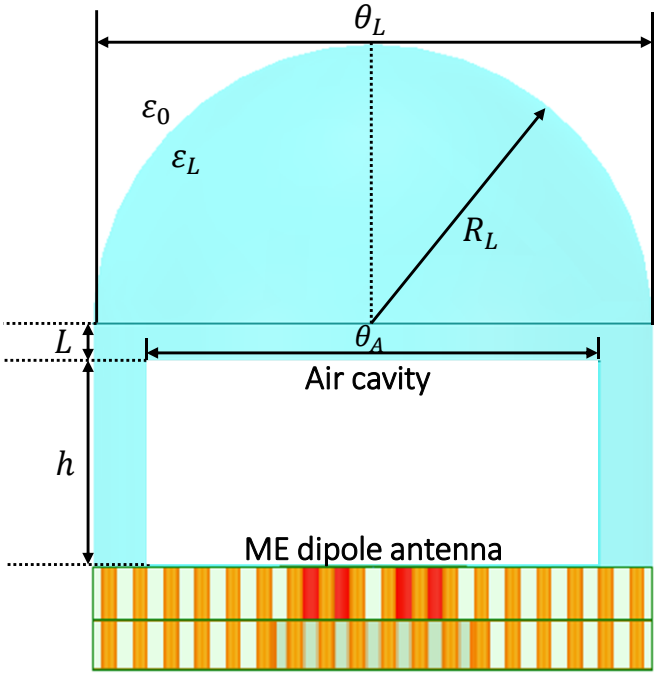

Figure 4-19: Geometry of the proposed lens

The lens is illuminated by a SIW-fed aperture coupled ME dipole antenna printed on substrate Rogers RO3003 ($\varepsilon_{sub} = 3$) , the feeding element is the same of the previous section and it is possible to see the characteristics parameters Return Loss and Gain vs Frequency response respectively in **Figure 4-10** and **Figure 4-11**.

The simulated Return Loss of the integrated lens antenna is depicted in **Figure 4-20**. As can be noticed, the antenna presents a good impedance matching which is smaller than -10 dB in the band of interest, that is to say from 71 GHz to 86 GHz, and covers the whole E-band.

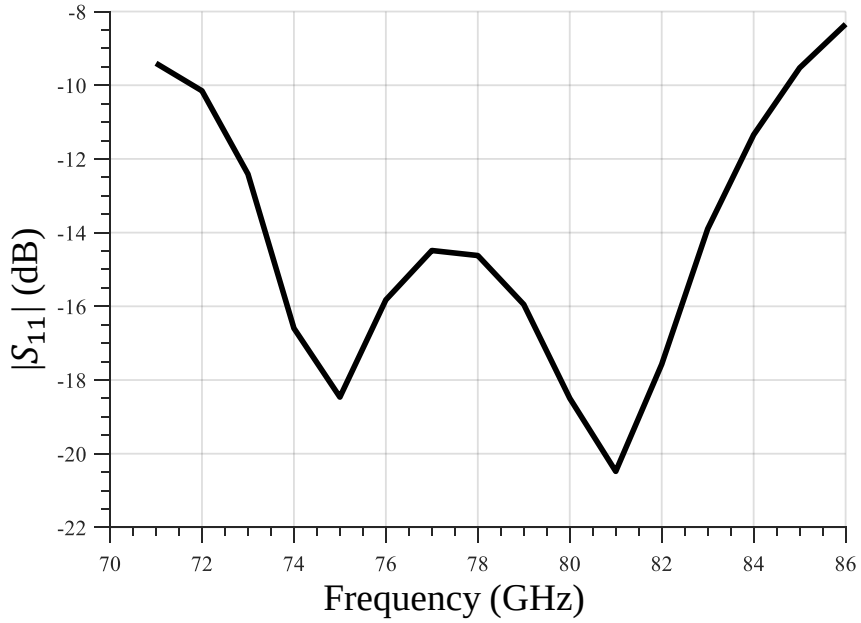

Figure 4-20: Simulated Return loss of the proposed integrated lens

In **Figure 4-21** is illustrated the gain vs frequency response of the proposed antenna, which shows a peak gain of 14.3 dBi at 86 GHz. The 3-dB beamwidth includes all the band of interest, as stated in the design specifications. With respect to the simple SIW fed aperture coupled ME dipole antenna, in this case, the lens provided a gain enhancement of about 3.5 dBi within the band of interest.

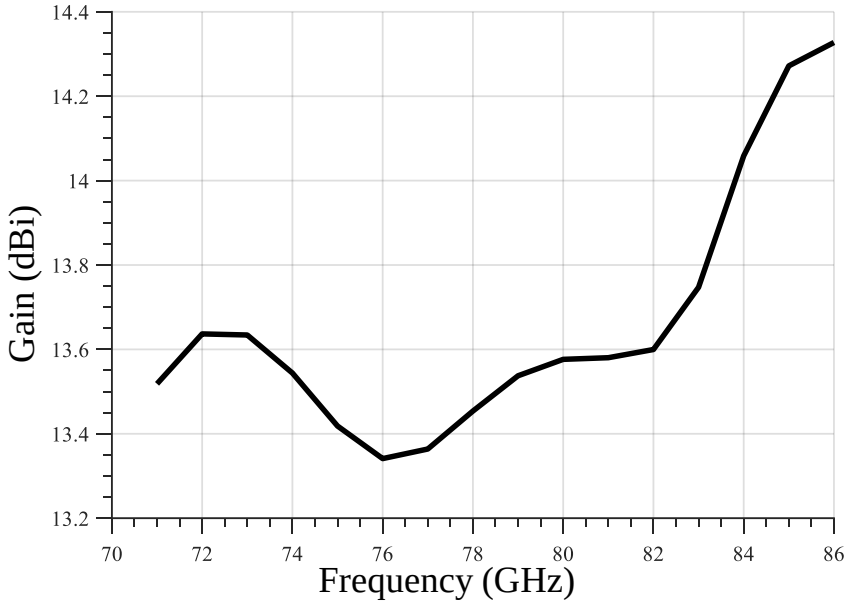

Figure 4-21: Simulated gain VS frequency of the proposed integrated lens

In **Figure 4-22** are shown the Radiation Patterns of the proposed lens at 71, 77, and 85 GHz. Even in this case, the proposed integrated lens antenna can be a valid solution as feeding element for the Cassegrain antenna, because it fulfills all the design requirements (**Table 4-1**).

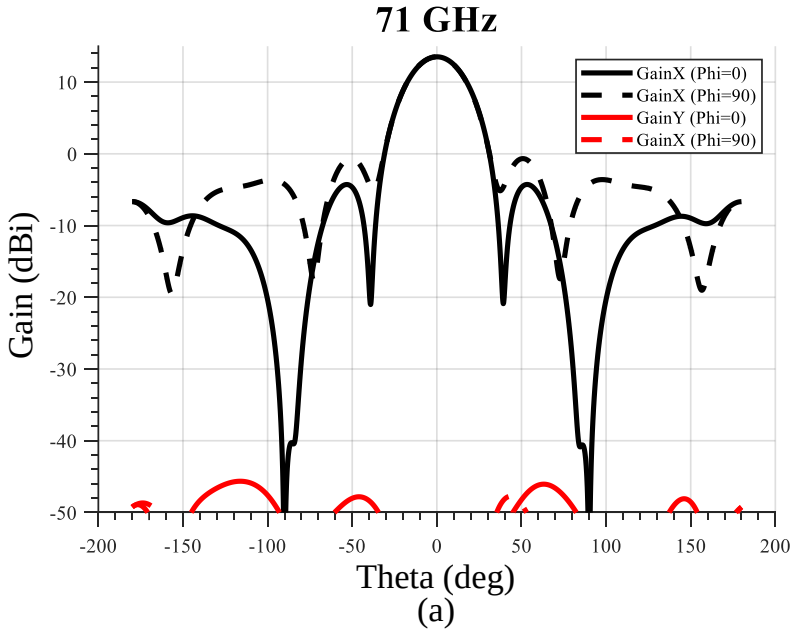

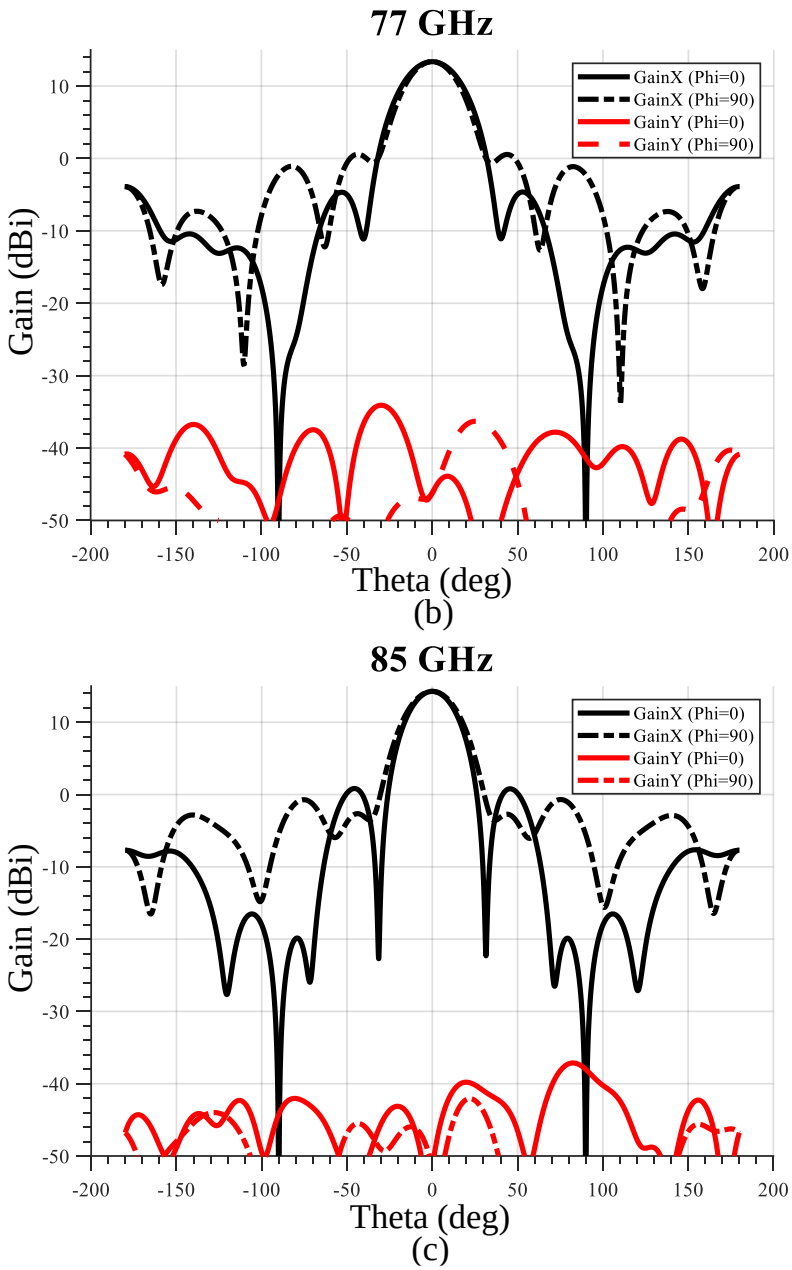

Figure 4-22: Radiation Patterns of the proposed integrated lens antenna at (a) 71 GHz (b) 77 GHz (c) 85 GHz

4.4.4 Fabry-Perot Cavity antenna

Fabry Perot Cavity Antennas (FPCAs) are a type of high directive antennas that belong to the category of planar antennas and they can be a valid alternative to simple planar microstrip antennas array or waveguide slot antennas array. Especially at mm-wave,

they bring with them lots of advantages such as high radiation efficiency and good radiation pattern performance. The recent renewed interest in periodic surfaces and metasurfaces, with these advantages, has attracted the interest of the research for designing high directivity antennas [54]. The basic concept of the Fabry-Perot cavity antenna was introduced for the first time by Trentini in 1956 [60], who used a partially reflecting surface (PRS) above a ground plane to produce high directivity. In particular, Trentini employed a geometric optics approximation to describe mathematically the antenna operation by means of the multiple reflections of plane waves between the ground plane and the PRS. Moreover, the term FPCA was still not used at time and it was introduced for the first time in 2001, when the similarities of the operating principle of these antennas with the Fabry-Perot interferometer, widely used in optics, were reported and a study on the effect of the periodic superstrate characteristics on the antenna bandwidth and directivity was performed. Other terms have also been used for these antennas such as Electromagnetic Band Gap (EBG) resonator antennas, high gain leaky-wave antennas, or PRS antennas. The main FPCA structure is composed by a partially reflective surface (PRS) placed at a distance h, which typically is about half-wavelength, and in parallel to a ground plane thus forming an open Fabry-Perot type resonant cavity. Also, an excitation source is typically included within the cavity with feeding antennas such as dipole, microstrip patch, or slot in the ground plane. The gain and the bandwidth of the FPCA depend on the reflection, evaluated in amplitude and phase, from the PRS as well as the distance from the ground plane. The PRS can be composed either by passive structure or metasurfaces, such as Frequency-Selective Surfaces (FSSs) or metasurfaces non-uniform unit cells [54]. As

stated before, the FPCA consists of a PRS and a ground plane acting as fully reflecting surface; to obtain a high gain two conditions must be satisfied:

1. High reflectivity in the cavity: the PRS has a high reflection coefficient. The PRS reflection coefficient magnitude R_{PRS} and the increased gain G are linked thanks to [100] which is valid for infinite array:

$$G = \frac{1+R_{PRS}}{1-R_{PRS}} \qquad (6)$$

The half-power fractional bandwidth 3 dB BW is inversely proportional to the reflection magnitude R_{PRS} as stated in [100]:

$$BW = \frac{\lambda(1-R_{PRS})}{2\pi h\sqrt{R_{PRS}}} \qquad (7)$$

where h is defined as the distance between the ground plane and the PRS superstate, that is to say, the cavity height, and λ the free-space wavelength.

2. The cavity height h, as a function of the resonant frequency f_r, must satisfy the following relationship [101]:

$$h = \frac{c}{4\pi f_r}(\phi_{PRS} + \phi_{GND} - 2\pi k),\ k = 0, \pm 1, \pm 2 \qquad (8)$$

where c is the speed of light, ϕ_{PRS} is the PRS reflection phase, and ϕ_{GND} the ground plane reflection phase ($\phi_{GND} = -\pi$).

For the case at hand, in order to realize a Fabry-Perot cavity antenna suited for the design specifications listed in **Table 4-1**, a magneto-electric dipole excited by a stripline has been selected as primary source of the PRS antenna, whose structure is shown in **Figure 4-23**. The ME-dipole antenna was designed first without the PRS cavity, and by using three substrate layers of Rogers RO3003 (ε_r), one thicker of $500\,\mu m$ and two smaller of $125\,\mu m$. The ME dipole stripline-fed antenna dimension are listed in **Table 4-4**, while the

characteristics parameters, that is to say, return loss and gain vs frequency response, are shown in **Figure 4-24** and **Figure 4-25**.

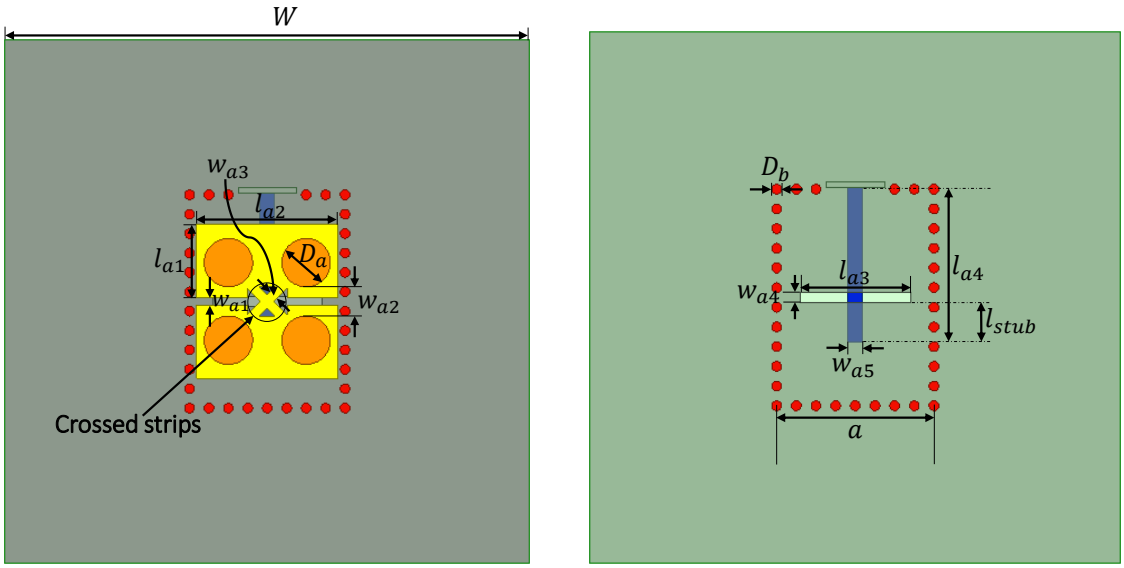

(a) (b)

Figure 4-23: ME dipole stripline-fed: (a) Top view (b) Bottom view

Parameters	W	w_{a1}	w_{a2}	w_{a3}	w_{a4}	w_{a5}	l_{a1}	l_{a2}	l_{a3}	l_{a4}	l_{stub}	D_a	D_b	a
Values (mm)	5.4	0.08	0.3	0.08	0.1	0.15	0.76	1.46	1.12	1.57	0.4	0.5	0.1	1.6

Table 4-4: ME dipole stripline fed antenna dimensions

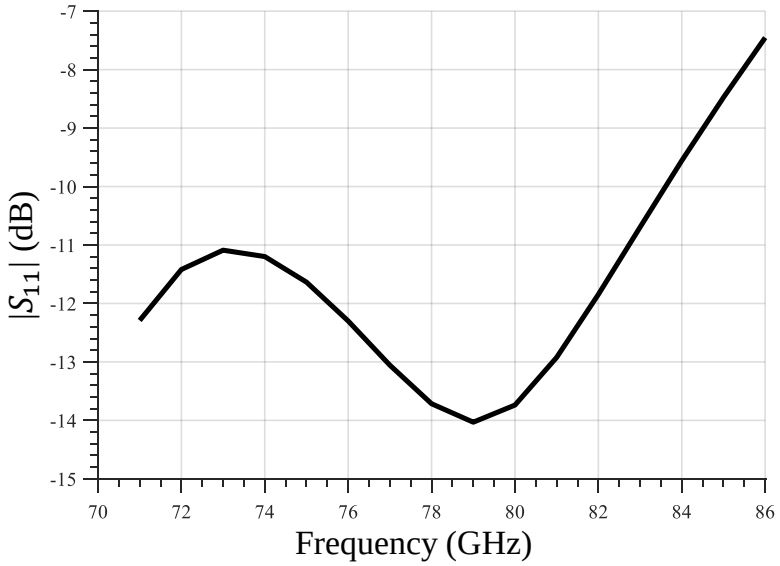

Figure 4-24: Simulated Return loss of the proposed ME-dipole stripline-fed antenna

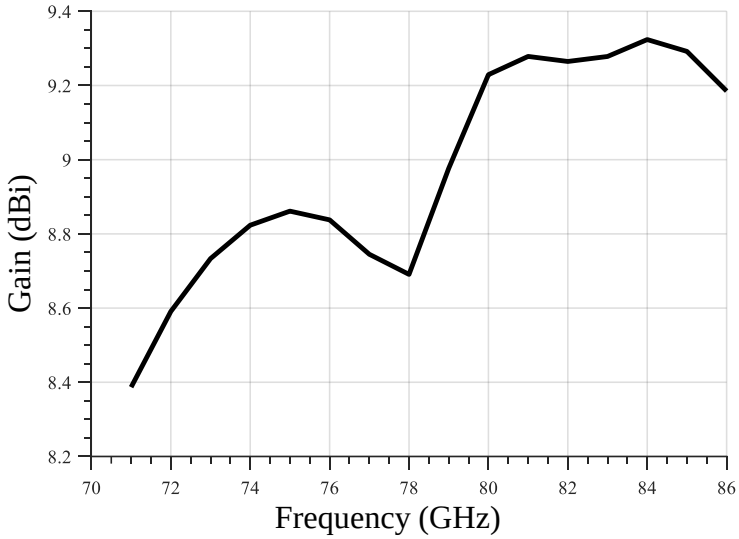

Figure 4-25: Simulated gain vs frequency of the proposed ME-dipole stripline-fed antenna

As depicted in **Figure 4-24**, the return loss of the ME dipole fed stripline antenna presents an impedance matching below $-10\ dB$ from 71 GHz to 84 GHz and it almost covers the whole band of interest, that is to say the E-band. In **Figure 4-25** is shown the gain vs frequency response, in which is visible a peak gain of 9.3 dBi at 84 GHz; and the 3-dB beamwidth covers all the band of interest, as stated in the design specifications.

The Fabry-Perot cavity antenna will be composed by the ME dipole fed stripline antenna and by an array of PRS, placed at a distance h; in **Figure 4-26** is presented the whole antenna structure. **Figure 4-27** shows the layout of the PRS, the proposed geometry is a double squared ring, whose dimensions are: $b = 1.6\ mm$, $a_1 = 1.15\ mm$, $a_2 = 0.9\ mm$ and $a_3 = 0.5\ mm$. The final PRS will be composed by 3x3 unit cell elements. A classical array was first performed using the initial unit cells, then later were rearranged in diagonal form to build a compact array. This compact geometry increases the metallic part of the unit cell, thus raising the reflectivity and the gain according to (6). The proposed PRS array

has been designed to ensure high reflectivity with a reduced size $1.4\lambda_0$ x $1.4\lambda_0$, with f_0=77 GHz.

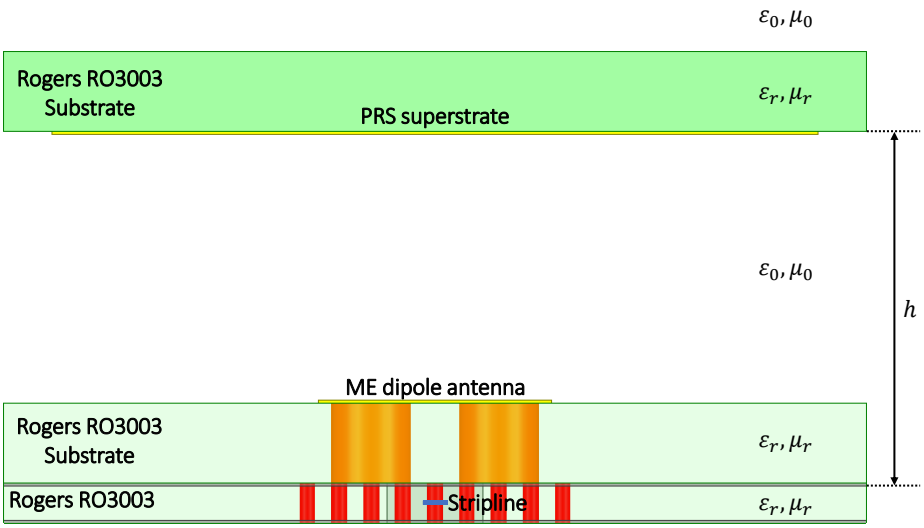

Figure 4-26: Side view of the proposed Fabry-Perot cavity antenna

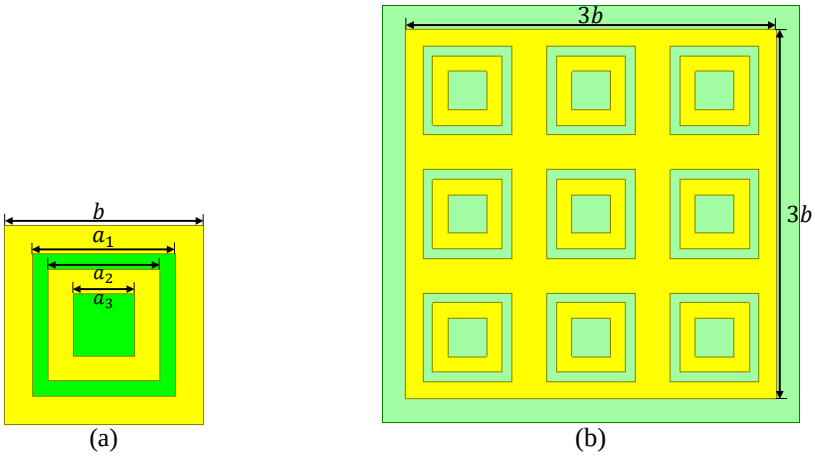

Figure 4-27: Layout of the PRS (a) PRS unit cell (b) 3x3 PRS array

In order to have an overview of the behavior of the PRS unit cell, simulations have been performed for the unit cell using Ansys HFSS [88] and applying a Floquet Port; in particular, the reflection magnitude and phase of the PRS unit cell have been taken into account and the simulation results are shown in **Figure 4-28**. As can be observed in the E-

band, the reflection coefficient in terms of magnitude varies from 0.73 to 0.89, while its phase it is comprised between -166° and 155.5°.

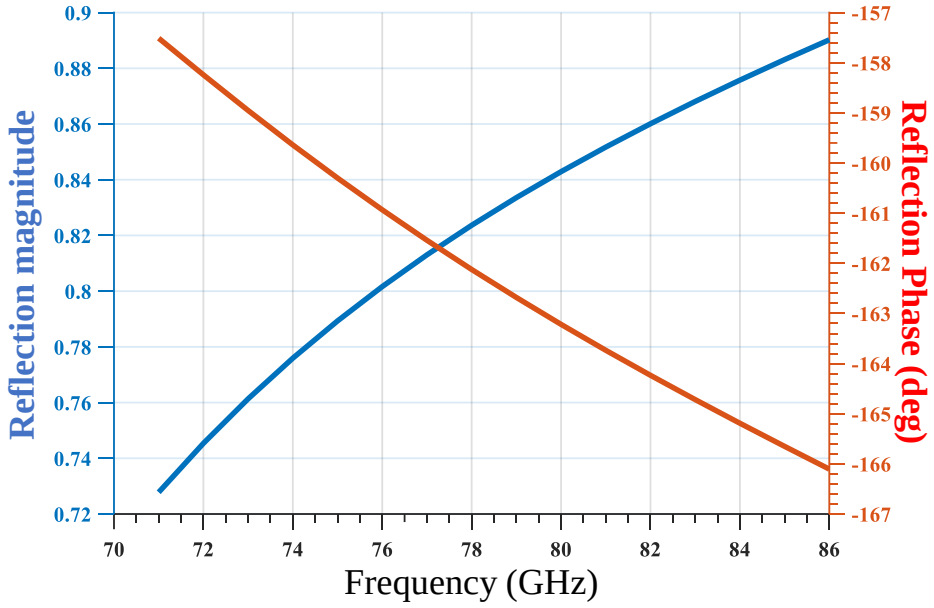

Figure 4-28: Reflection magnitude and phase of the PRS unit cell

The reflection coefficient parameters depicted in **Figure 4-28** have been used in (8) to evaluate the height h of the Fabry-Perot cavity antenna, at the same time this height is defined as the distance between the ground plane and the PRS surface. The height cavity variations within the band of interest are illustrated in **Figure 4-29**; to obtain high gain within the band of interest the suitable cavity height has been set to $h = 2.2$ mm, with a resonant frequency of $f_r = 72\ GHz$.

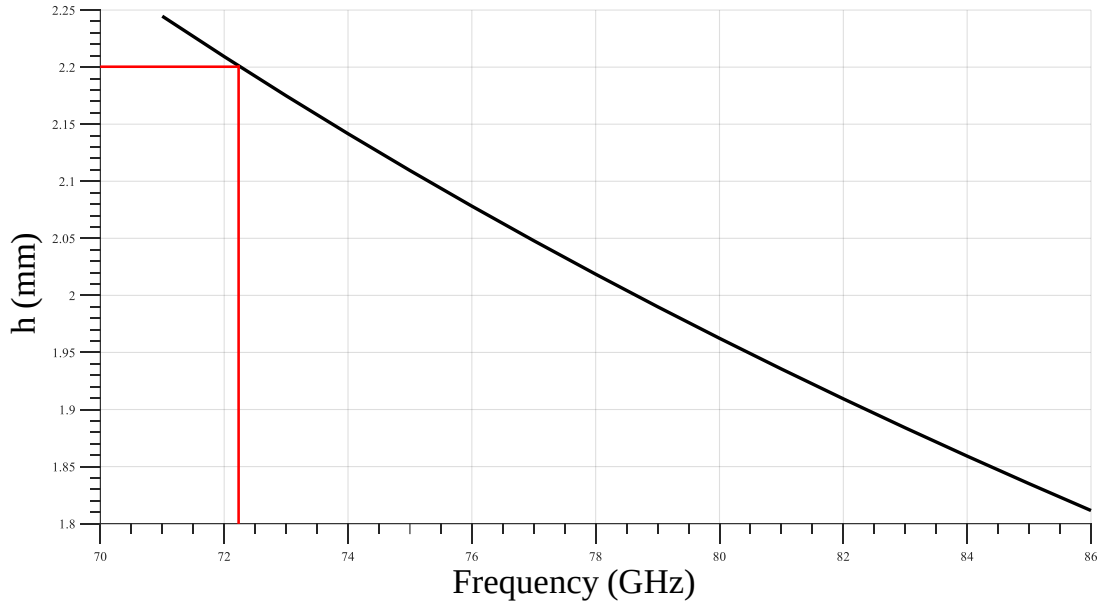

Figure 4-29: Fabry-Perot cavity antenna height variations

The final FPCA is presented in **Figure 4-30**.

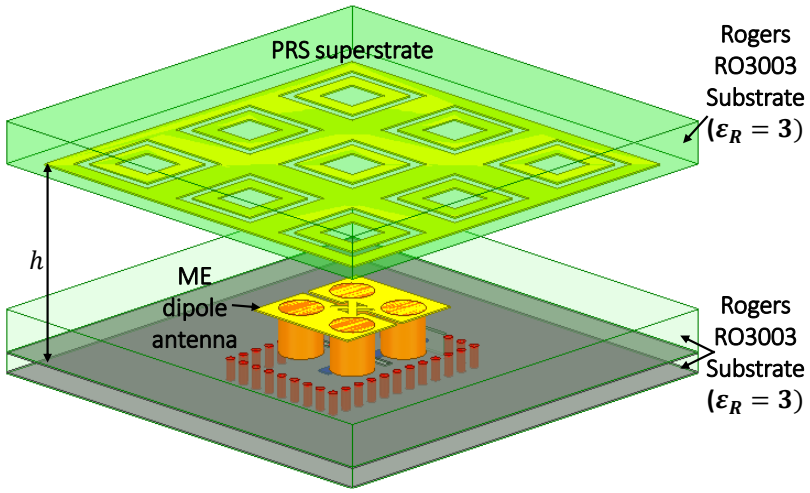

Figure 4-30: Proposed Fabry-Perot cavity antenna

The simulation results of the proposed Fabry-Perot cavity antenna are shown in **Figure 4-31** and **Figure 4-32**. With respect to the source element, that is to say the ME dipole stripline-fed, the return loss presents an impedance matching below $-10\ dB$ from 73 GHz to 85 GHz, in this case the impedance matching bandwidth, has been slightly upshifted.

The gain vs frequency response (**Figure 4-32**) shows a peak gain of 11.9 dBi at 71 GHz, with a 3-dB beamwidth which covers all the band of interest.

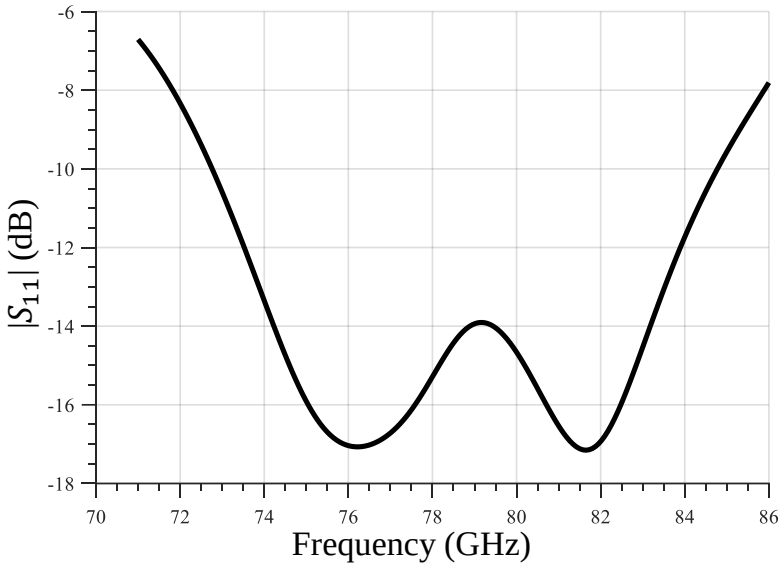

Figure 4-31: Simulated Return loss of the proposed Fabry-Perot cavity antenna

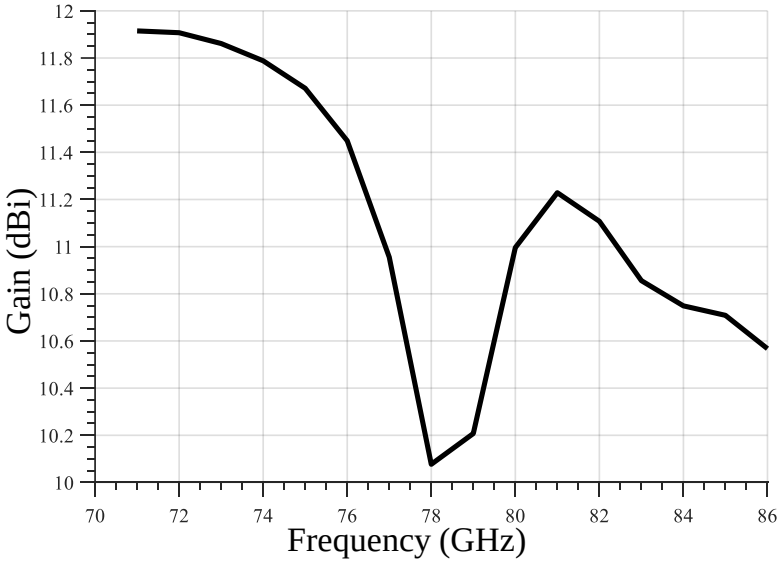

Figure 4-32: Simulated gain VS frequency of the proposed Fabry-Perot cavity antenna

In terms of gain response, the Fabry-Perot cavity antenna, with respect to the source ME-dipole stripline-fed antenna, provides an average gain enhancement of about 2 dBi within the band of interest. In particular, as shown in **Figure 4-33**, the gain enhancement is evident

from 71 to 76 GHz in which there is an average gain improvement of 3 dBi, and from 80 to 82 GHz, where the gain response increases its value of about 2 dBi. This localized gain enhancement can be ascribed to the PRS, which is working at these frequencies. This is also confirmed by **Figure 4-29**, in which the decay of the curve related to the height of the FPCA is less pronounced at these frequencies, in which the FPCA is working correctly.

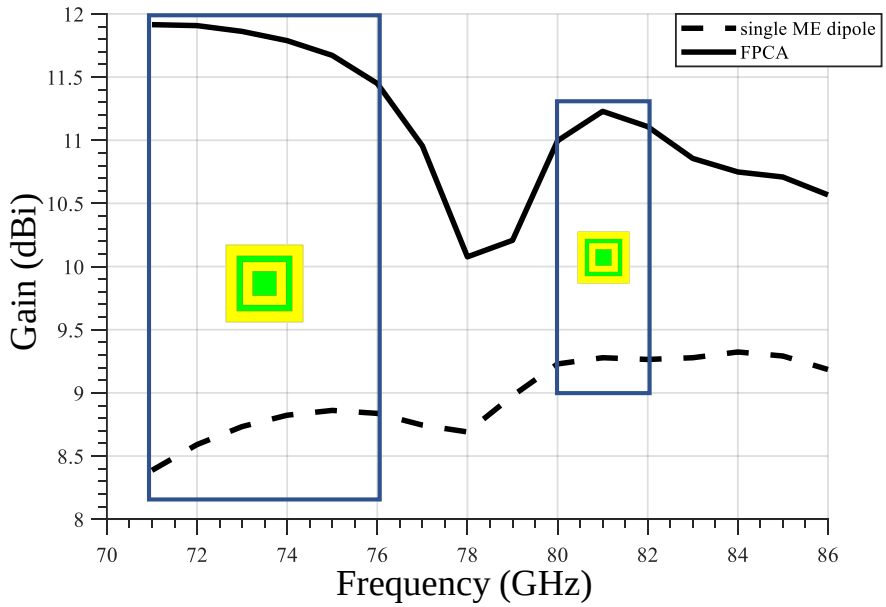

Figure 4-33: Simulated gain vs frequency comparison FPCA vs ME-dipole stripline fed

In **Figure 4-34** are illustrated the radiation patterns at 71, 77, and 85 GHz of the proposed FPCA. At 85 GHz for GainX, when Phi=0°, some side lobes appear; this behavior can be ascribed to the fact that the PRS, which realizes the FPCA, isn't working correctly at that frequency, and for this reason side lobes are present. The FPCA can be a valid candidate for feeding the final Cassegrain antenna, because all the requirements are respected.

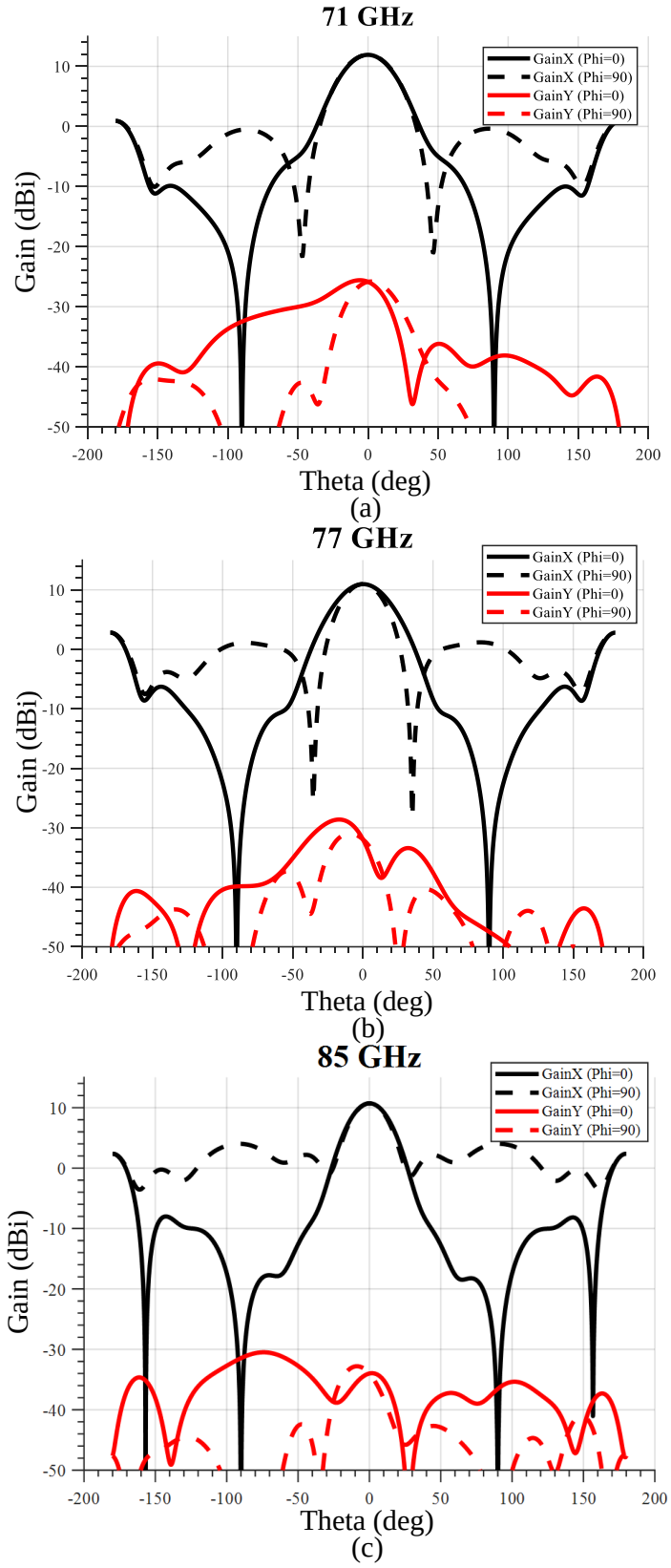

Figure 4-34: Radiation Patterns of the proposed Fabry-Perot cavity antenna at (a) 71 GHz (b) 77 GHz (c) 85 GHz

4.5 Primary feed test in Cassegrain configuration

After evaluating all the possible feeding antennas for the Cassegrain configuration, an array 7x7 of SIW-fed aperture coupled ME dipole has been selected as primary feed for the final Cassegrain antenna. All the solutions presented in the previous paragraph are valid, but only the SIW-fed aperture coupled ME dipole array has been designed and fabricated. The selected array will be composed by 49 elements with a unit cell dimension $x_b = 5.1$ mm and the final antenna will be a beam-switched antenna, in which will be activated one element per time and every single cell will be capable to provide a steering of $\theta_B = 0.33$ degrees. These information are well known from the studies done in the previous sections. The final array dimension will be 37.2 mm x 37.2 mm and an external frame of vias has been added to confine the EM-field. The proposed array 7x7 is shown in **Figure 4-35**.

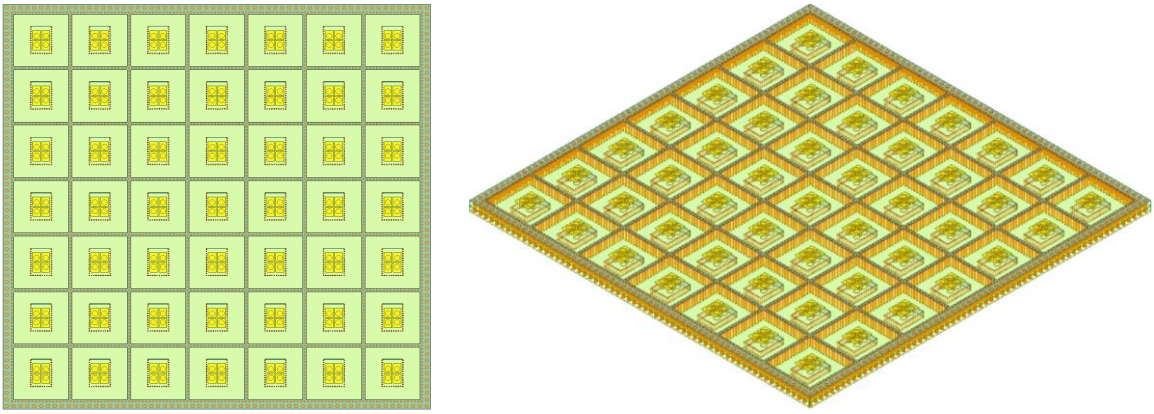

(a) (b)

Figure 4-35: SIW-fed aperture coupled ME dipole antenna array (a) Top view (b) Side view

By activating the central element, it is possible to have an overview of the behavior of the array by considering return loss and gain vs frequency response, which are illustrated in **Figure 4-36** and **Figure 4-37**. As can be stated, both the responses are very similar to the ones presented in section 4.4.1 (**Figure 4-10** and **Figure 4-11**). The radiation patterns at

71, 77, and 85 GHz of the central element, in array configuration, are presented in **Figure 4-38**. The peak gain is 11.4 dBi at 86 GHz and the 3-dB beamwidth covers all the E-Band.

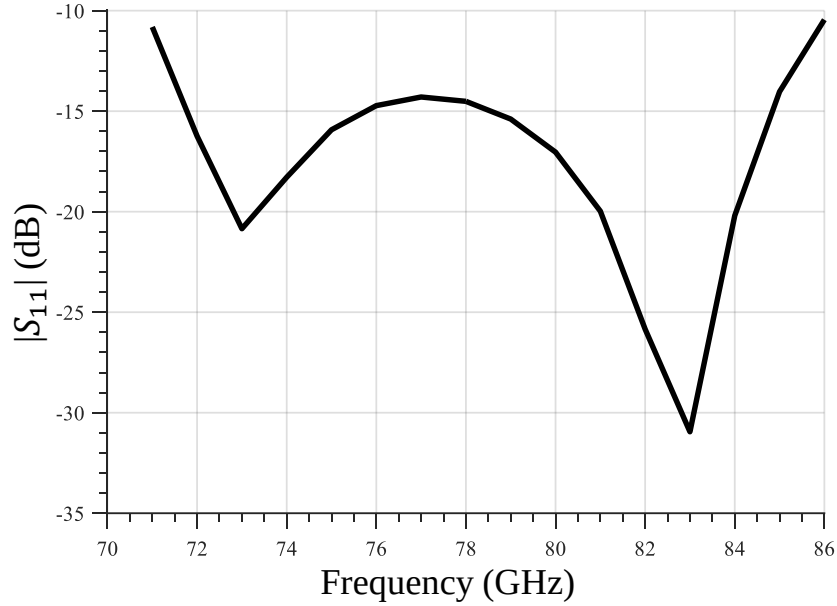

Figure 4-36: Simulated return loss of SIW-fed aperture coupled ME dipole antenna 7x7 array by activating the central element

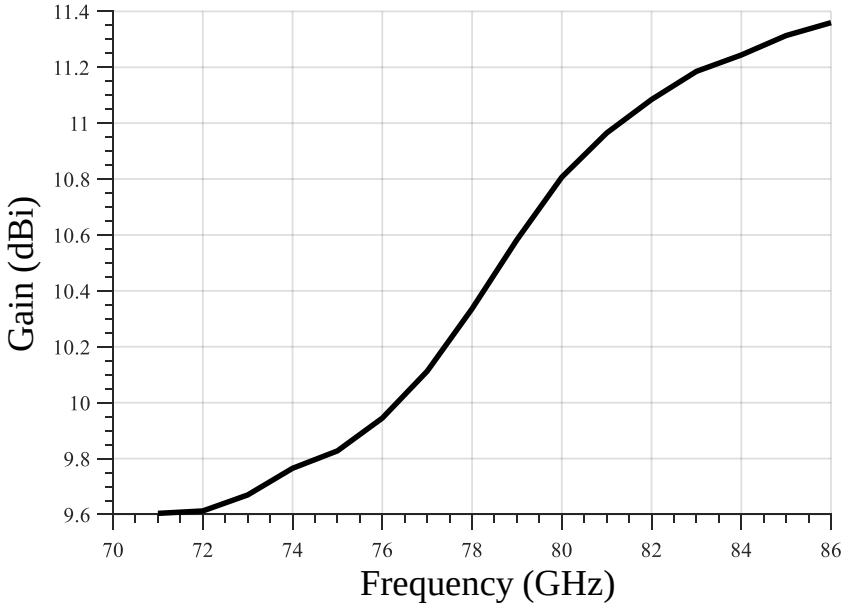

Figure 4-37: Simulated gain VS frequency of SIW-fed aperture coupled ME dipole antenna 7x7 array by activating the central element

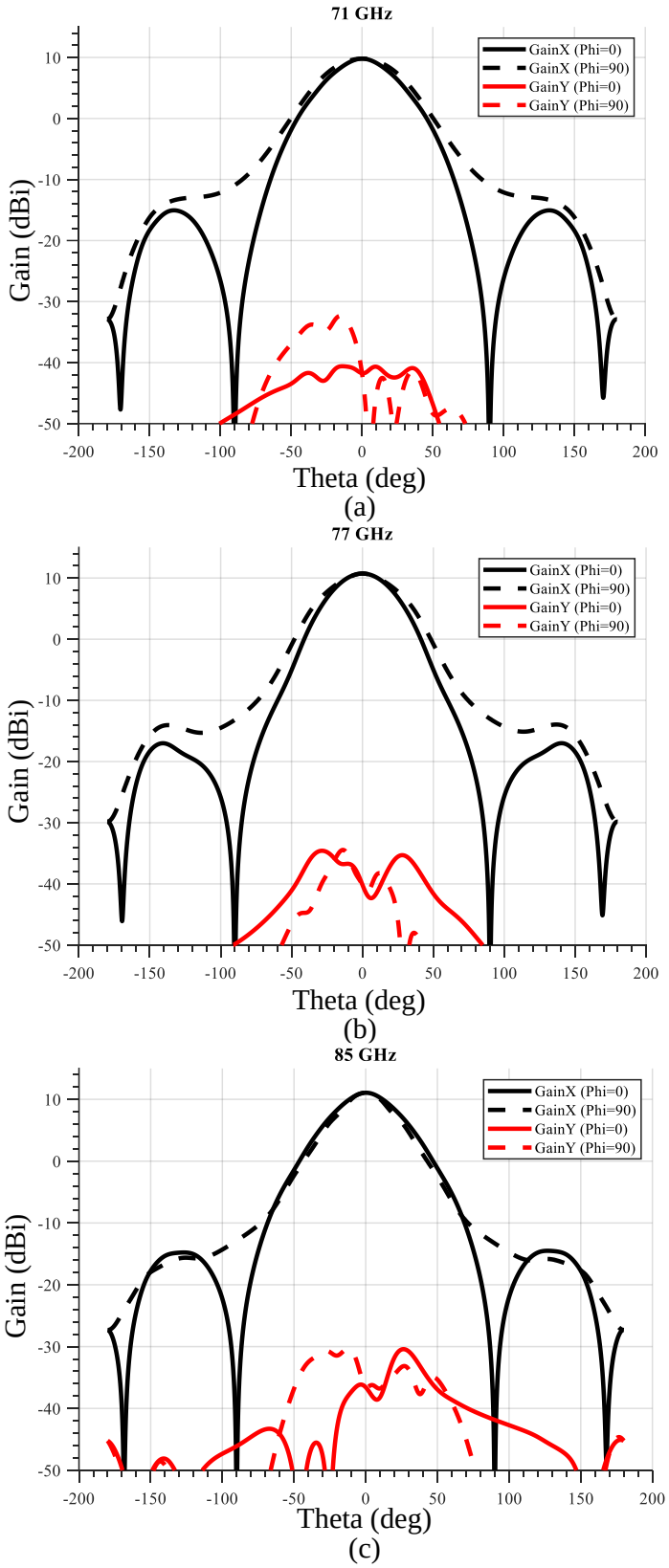

Figure 4-38: Radiation Patterns of SIW-fed aperture coupled ME dipole antenna 7x7 array by activating the central element at (a) 71 GHz (b) 77 GHz (c) 85 GHz

Once presented the 7x7 array central element performance, it is necessary to test the whole array in Cassegrain configuration. For this purpose, Ansys Savant [102] has been used to test the whole design. Savant is an industry tool that gives the possibility to do a highly efficient EM analysis of antennas on electrically large platforms (e.g reflectors, double reflectors). The algorithm used by this software is the Shooting and Bouncing Rays (SBR) technique and at the same time, Savant allows full antenna scattering prediction for geometries that are thousands of wavelengths in size, computing: far-fields patterns, near field distributions, and antenna-to-antenna coupling. Savant is the only commercial electromagnetic software to extend SBR with simultaneously consistent implementations of Physical Theory of Diffraction (PTD), Uniform Theory of Diffraction (UTD), and Creeping Wave to deliver maximum accuracy within a high-performance ray-tracing framework for large scale problems [102]. The complete Cassegrain configuration which includes the 7x7 SIW-fed ME-aperture coupled antenna array and which will be used in Savant is shown in **Figure 4-39**. The diameter of the main reflector is $D = 90$ cm, the eccentricity of the sub-reflector is $Ecc = 1.7$, the focal distance is $F = 22.5$ cm, the ratio of focal length to reflector aperture size is $f/D = 0.25$ and the ratio of the interfocal distance to the focal distance is $IF/F = 0.7$.

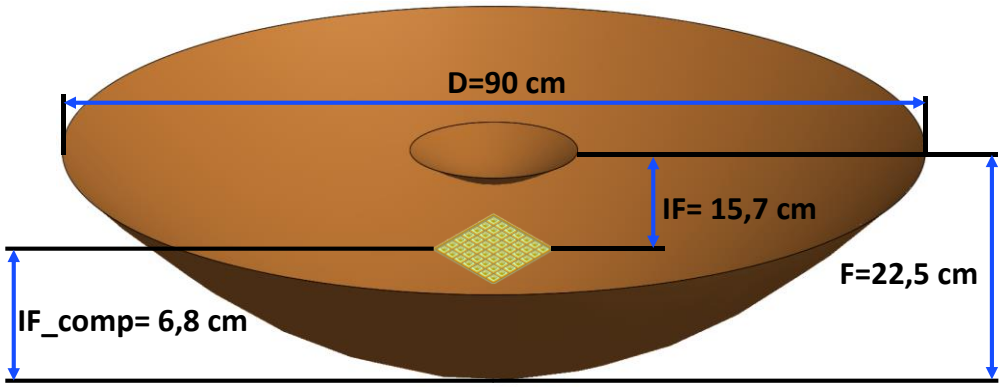

Figure 4-39: Cassegrain antenna fed by 7x7 SIW-fed aperture coupled ME dipole antenna array

To evaluate the performance of the 7x7 ME dipole array in the Cassegrain configuration, for extracting the Cassegrain antenna characteristic parameters, it was necessary to organize the work into two steps.

In the first part, several simulations have been done in Ansys HFSS for assessing the behavior of the 49 elements that create the 7x7 ME dipole array and then in the second part, the field of each element of the array has been exported from HFSS to Savant and analyzed in Cassegrain configuration.

It was possible to analyze the whole structure by adding in Savant a CAD file composed by the double reflector structure and thus obtaining the scheme proposed in **Figure 4-39**.

For simplicity, in **Figure 4-40** is reported a scheme of the 7x7 array with each element with the correspondent excitation port, which will play an important role in the next pages in which will be discussed the Cassegrain antenna results.

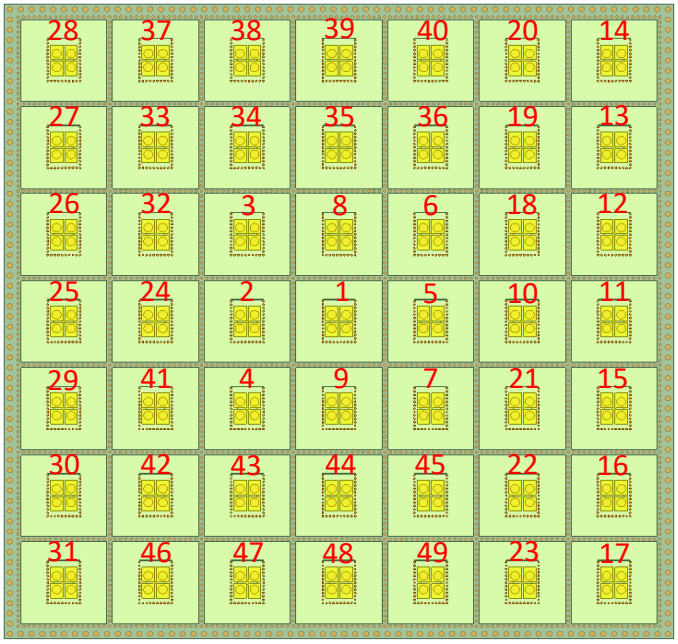

Figure 4-40: 7x7 SIW-fed aperture coupled ME dipole antenna array with the excitation ports

As stated in the design specification (**Table 4-1**) the Cassegrain antenna must provide a steering angle of $\theta_B = \pm 1$ degrees, and by using a beam-switched feeding antenna array it must guarantee a peak gain $\geq$ 50 dBi, within a frequency range that goes from 71 to 86 GHz, covering the whole E-Band. The complete Cassegrain antenna has been analyzed along the two cuts of Azimuth and Elevation, by activating one element at time as a beam-switched antenna response. In **Figure 4-41** is shown the 7x7 SIW-fed aperture coupled ME dipole antenna array in which ports 1,5,10 and 11 are activated separately in Cassegrain configuration, as in the scheme of **Figure 4-39**, along Azimuth cut, for which have been evaluated and analyzed the radiation patterns.

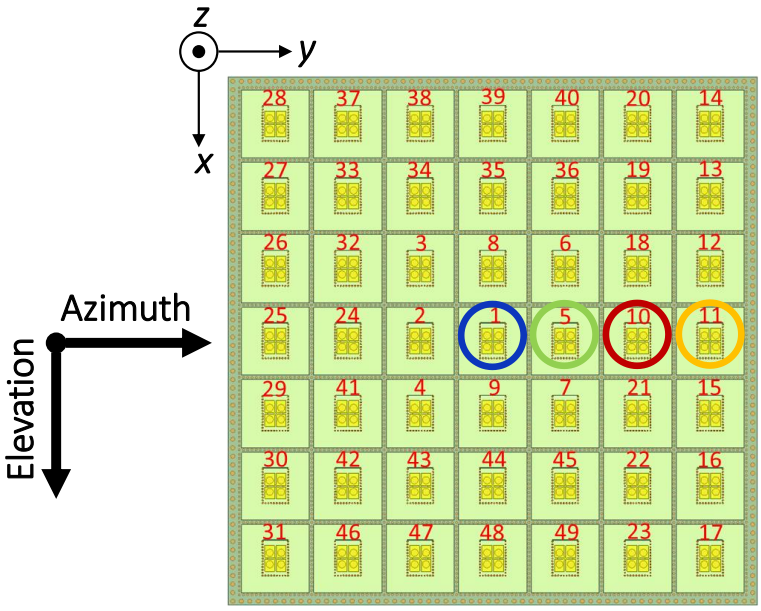

Figure 4-41: 7x7 SIW-fed aperture coupled ME dipole antenna array with the excitation ports activated separately along Azimuth cut

In **Figure 4-42** are presented the radiation patterns at three different frequencies, 71,77 and 85 GHz, for the Cassegrain antenna by activating separately ports 1,5,10 and 11. In terms of steering by activating port 1, the steering angle is $\theta_B = 0°$, by turning on port 5 is provided a steering of $\theta_B = 0.33°$, by switching on port 10, $\theta_B = 0.66°$ and finally by

powering up port 11, $\theta_B = 0.96°$. The peak gain at 71 GHz varies from 52 dBi to 51.73 dBi. At 77 GHz the maximum gain is comprised in a range between 53 dBi and 52.75 dBi. At 85 GHz the peak gain is 53.93 dBi, when $\theta_B = 0.33°$, the minimum value of peak gain is 53.72 dBi, when $\theta_B = 0.96°$.

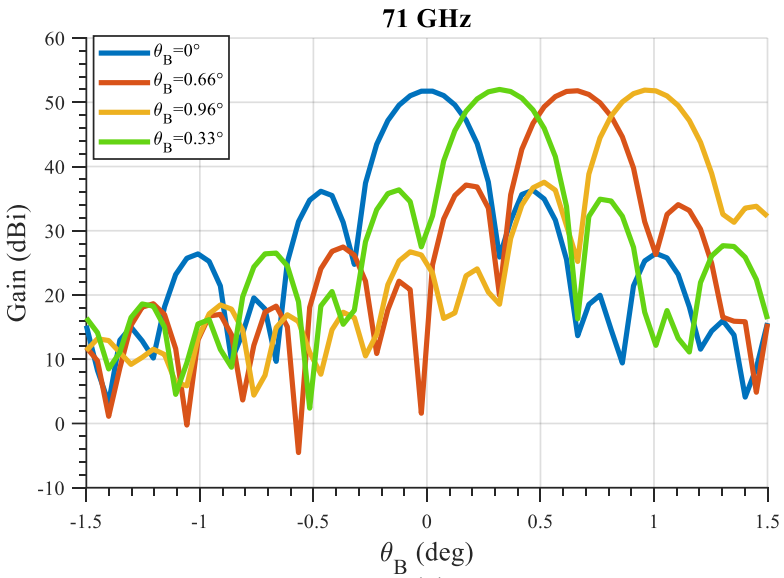

(a)

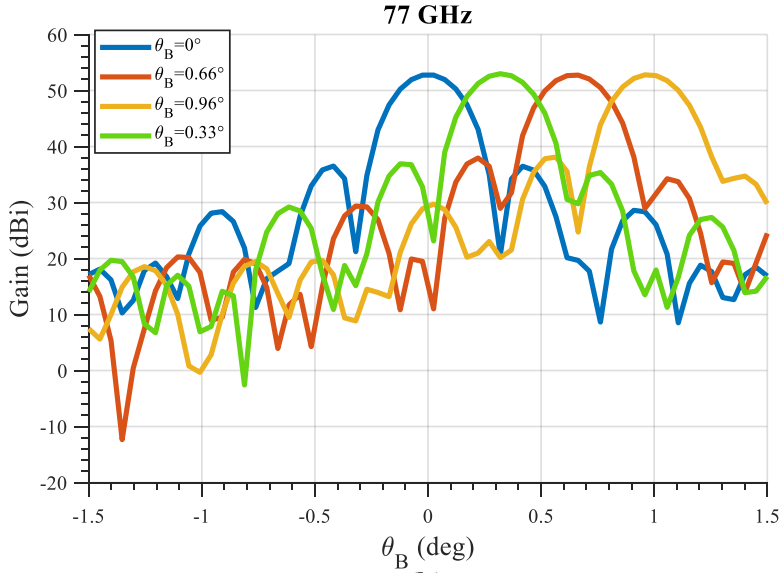

(b)

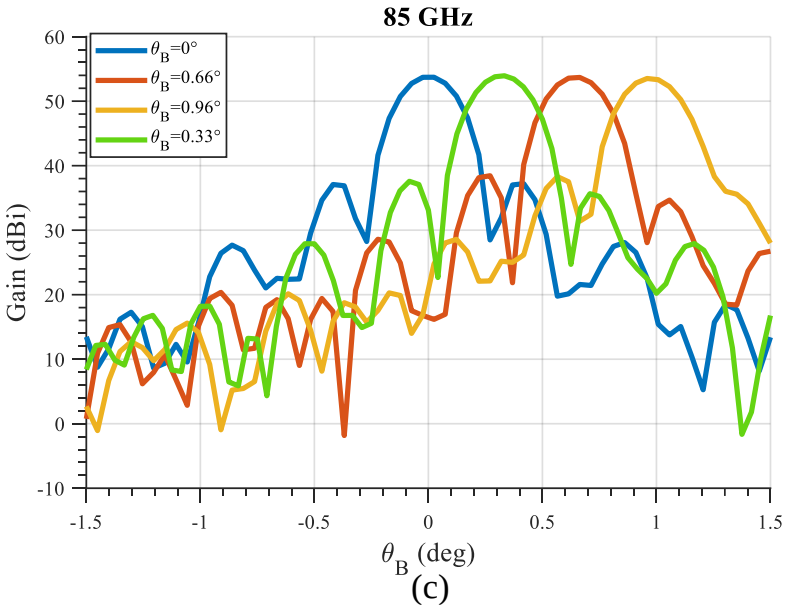

Figure 4-42: Cassegrain antenna Radiation Patterns by activating separately ports 1,5,10 and 11 at (a) 71 GHz (b) 77 GHz (c) 85 GHz

In **Figure 4-43** is illustrated the 7x7 SIW-fed aperture coupled ME dipole antenna array in which ports 1,8,35 and 39 are turned on separately, in Cassegrain configuration along Elevation cut, for which have been evaluated and analyzed the radiation patterns.

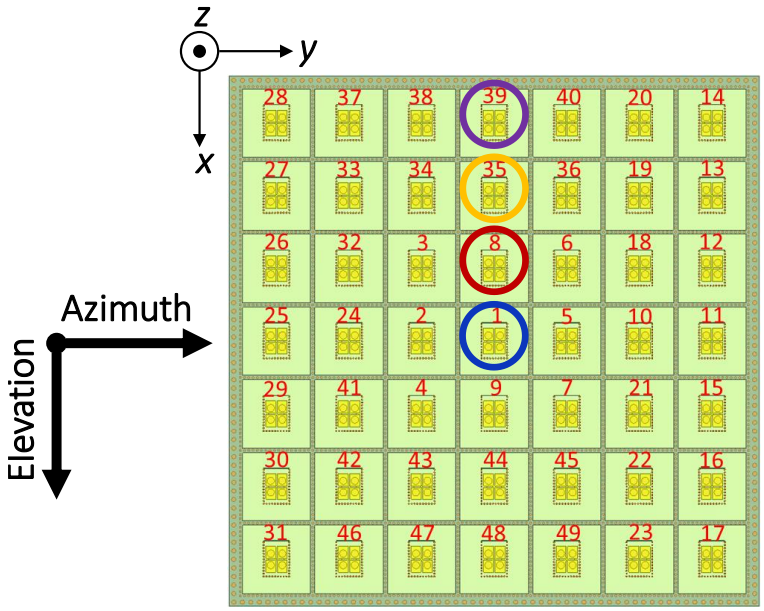

Figure 4-43: 7x7 SIW-fed aperture coupled ME dipole antenna array with the excitation ports activated separately along Elevation cut

In **Figure 4-44** are displayed the radiation patterns at three different frequencies, 71,77 and 85 GHz, for the Cassegrain antenna by activating separately ports 1,8,35 and 39 along Elevation cut. In terms of steering by activating port 1, the steering angle is $\theta_B = 0°$, by turning on port 8 is provided a steering of $\theta_B = -0.33°$, by switching on port 35, $\theta_B = -0.66°$ and finally by powering up port 39, $\theta_B = -0.96°$. The peak gain at 71 GHz is 51.93 dBi, when $\theta_B = -0.33°$. The minimum value of peak gain is 51.65 dBi, when $\theta_B = -0.96°$. At 77 GHz the peak gain varies between 52.91 dBi and 52.57 dBi. At 85 GHz the maximum gain is comprised in a range between 53.94 dBi and 53.45 dBi.

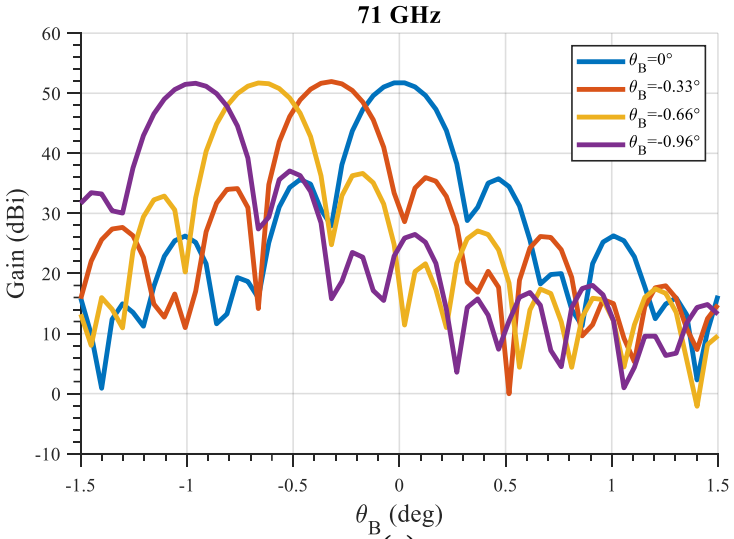

(a)

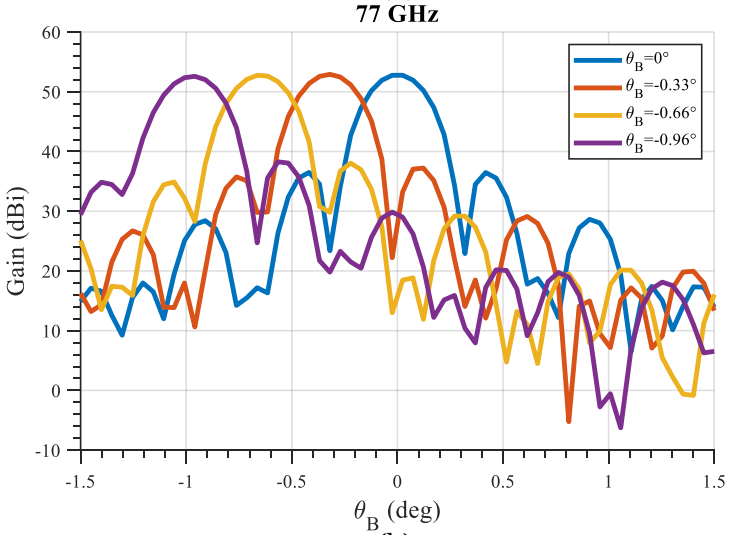

(b)

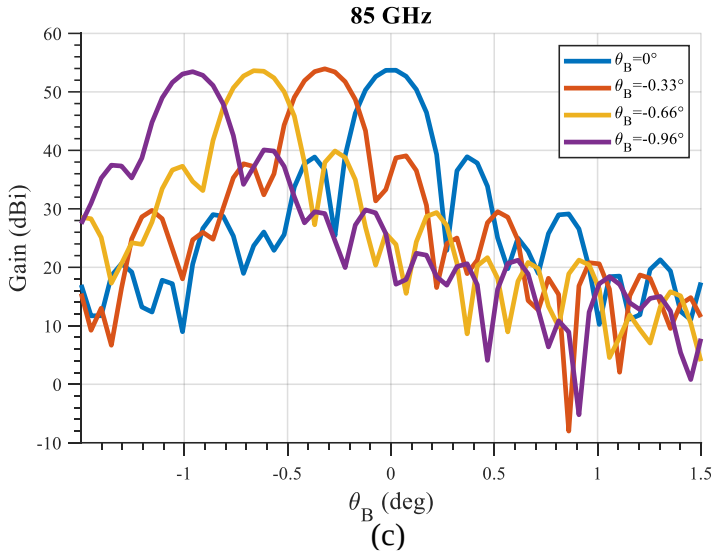

(c)

Figure 4-44: Cassegrain antenna Radiation Patterns by activating separately ports 1,8,35 and 39 at (a) 71 GHz (b) 77 GHz (c) 85 GHz

In **Figure 4-45** is shown the 7x7 SIW-fed aperture coupled ME dipole antenna array in which ports 1,6,19 and 14 are turned on separately in Cassegrain configuration, along Elevation cut, for which have been evaluated and analyzed the Radiation patterns. In this case, the Elevation cut has been twisted of 45° and the elements of the diagonal have been analyzed.

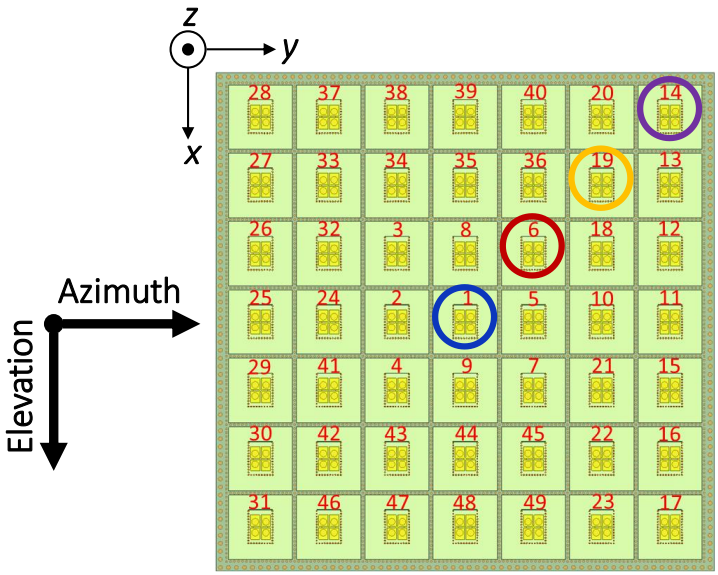

Figure 4-45: 7x7 SIW-fed aperture coupled ME dipole antenna array with the excitation ports activated separately along the diagonal of the twisted Elevation cut

In **Figure 4-46** are displayed the radiation patterns at three different frequencies, 71,77 and 85 GHz, for the Cassegrain antenna by activating separately ports 1,6,19 and 14 along the twisted Elevation angle. The rotation of 45° of the cut changes the steering angle. By considering separately the elements on the diagonal of the array, a factor of $\sqrt{2}$, which represents the diagonal of the square array, must be multiplied to the steering angle $\theta_B$provided by the reference Elevation cut. For this reason, in terms of steering by turning on port 1, the steering angle is $\theta_B = 0°$. By switching on port 6 is provided a steering of $\theta_B = \sqrt{2} * (-0.33°) = -0.47°$. By activating port 19 $\theta_B = \sqrt{2} * (-0.66°) = -0.96°$ and finally by powering up port 14, $\theta_B = \sqrt{2} * (-0.96°) = -1.36°$. The peak gain at 71 GHz varies from 52.25 dBi to 51.8 dBi. At 77 GHz the maximum gain is comprised in a range between 53.32 dBi and 52.58 dBi.

At 85 GHz the peak gain is 54 dBi, when $\theta_B = -0.47°$. The minimum value of peak gain is 52.85 dBi when $\theta_B = -1.36°$.

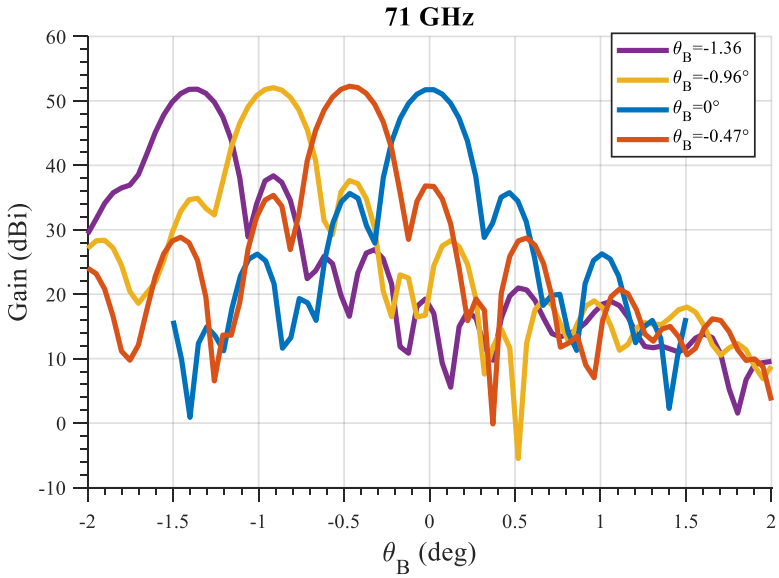

(a)

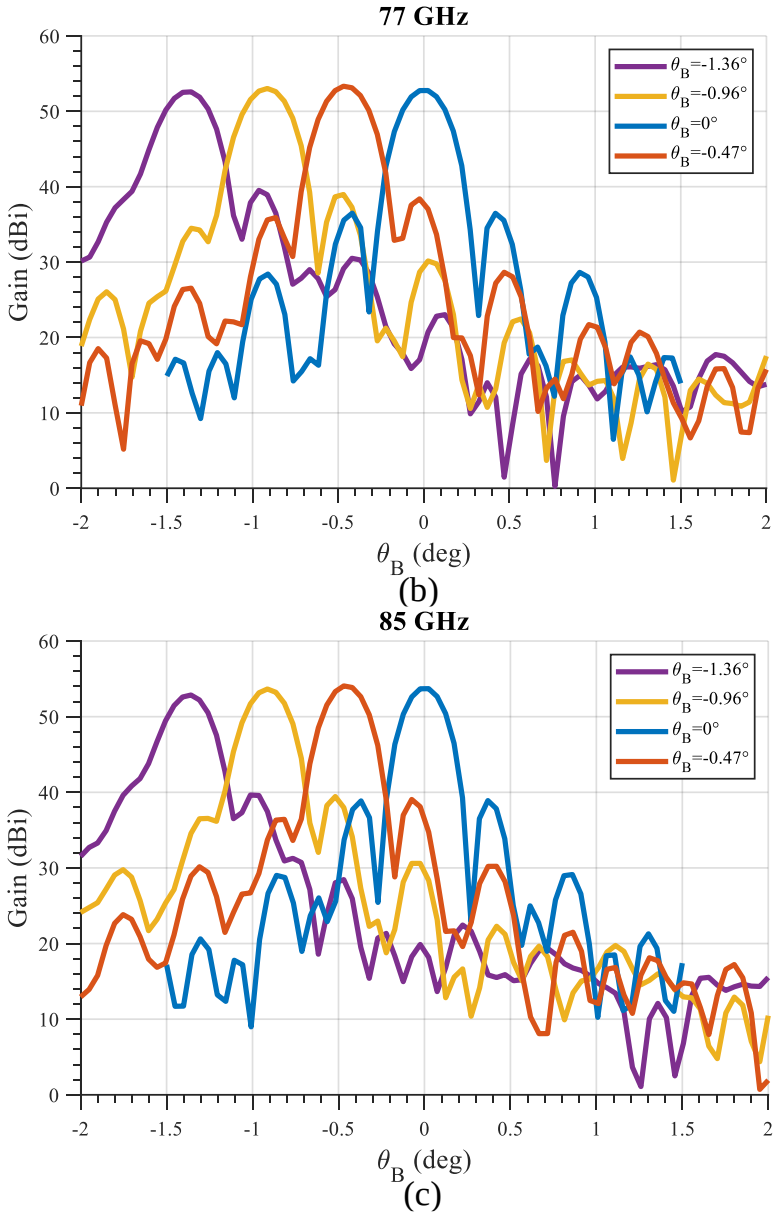

Figure 4-46: Cassegrain antenna Radiation Patterns by activating separately ports 1,6,19 and 14 at (a) 71 GHz (b) 77 GHz (c) 85 GHz

As shown in the results of the Cassegrain antenna fed by a 7x7 SIW-fed aperture coupled ME dipole antenna array, it is possible to state that the achieved gain, at different frequencies, perfectly matches the design specifications listed in **Table 4-1**.

The final beam-switched Cassegrain antenna is realized by the 7x7 SIW-fed aperture coupled ME dipole antenna array which feeds the double reflector structure and meets all

the antenna requirements: the impedance matching is below -10 dB within the E-Band (71-86 GHz), the average peak gain at different frequencies is bigger than 50 dBi and the steering specification of $\theta_B = \pm 1°$ are guaranteed with each element of the antenna capable of tilting the main beam of an angle $\theta_B = \pm 0.33°$.

A prototype of the 7x7 SIW-fed aperture-coupled ME-dipole antenna array has been realized and it is under measurements, the antenna is shown in **Figure 4-47**.

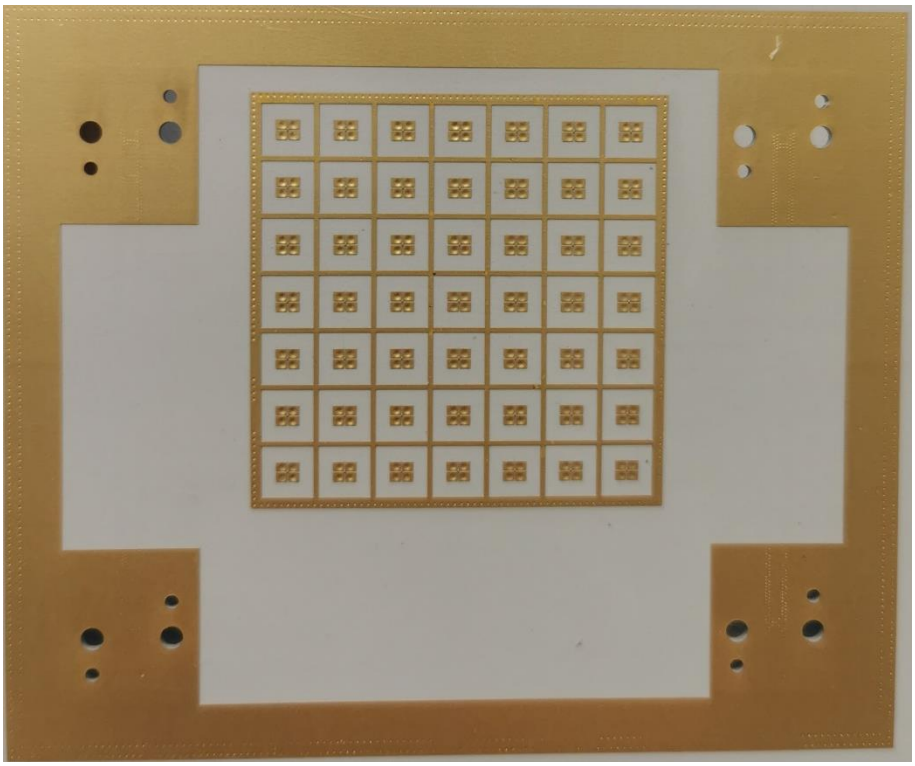

Figure 4-47: SIW-fed aperture-coupled ME-dipole antenna array prototype

CHAPTER 5

ON-CHIP ANTENNAS

5.1 On-chip antennas: theoretical background

Nowadays, there is a growing demand for high-frequency bandwidth mm-wave (30-300 GHz) electronic wireless transceiver systems to support applications such as high data rate wireless communication and high-resolution imaging. Today's wireless systems comprise four major modules: the digital baseband module, which deals with signal processing, the mixed-signal module handling signal conditioning, the RF front-end providing the RF carrier with modulated data, and the antenna for transmission of the signals. Wireless systems have been thought by integrating these four modules both horizontally or vertically, moreover, this method gives the possibility to choose the best technology suited for each component. For example, power amplifiers are best suited to the III-V compound semiconductor technology; antennas offer high efficiency on low-loss printed circuit boards (PCB) and digital circuits are best suitable to CMOS (complementary metal-oxide-semiconductor) or BiCMOS. The horizontal integration results in the multichip modules (MCM) and this approach uses significant chip area, which represents a big disadvantage with the ever-reducing size of wireless devices. On the other hand, vertical integration takes advantage of the system-in-package (SiP) approach, by reducing the form factors. This method is a valid alternative to the previous one, but functional modules, such as antennas, remain outside the package because of their dimension being the largest component of the system. Moreover, integrating these different technologies enhances the difficulties,

especially at higher frequencies where lossy interconnections and specialized processes such as flip-chip bonding and bond-wire play an important role, by increasing the complexity and the costs.

Backhauling links operating in the millimeter-wave frequencies are becoming an essential technology foundation to fulfil the multiple gigabits per second connectivity challenge posed by the 5G network infrastructures. Among the upcoming frequencies, growing attention is being received by E, W, and D-bands, which provide a total of around 50 GHz of available spectrum. The reduced wavelength associated with these frequencies creates a new context of opportunities that find fertile ground on emerging microelectronic technologies. From this perspective, it is particularly attractive the possibility to monolithically integrate a complete wireless sub-system, included the antenna, in a single chip [103], by creating a complete System on Chip (SoC), as shown in **Figure 5-1**.

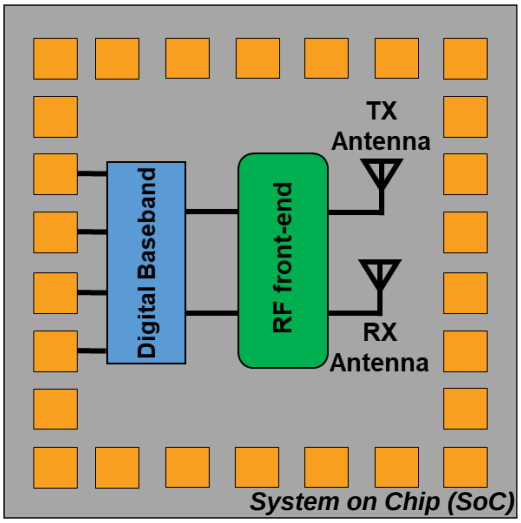

Figure 5-1: Representation of a SoC integration

In this case, as an alternative to the implementation of the antenna off-chip, it can be integrated directly on the chip. Antenna on Chip (AoC) is a valid solution because of the small antenna dimension, given by the high dielectric constant of the silicon substrate, and

furthermore, the lossy interconnections between amplifier and antenna are removed. AoCs are typically based on standard CMOS or BiCMOS technologies. Four fundamentals antennas commonly appear as on-chip antennas: monopole, dipole, Yagi-Uda, and loop antennas. The choice of each is dependent on the requirements of gain, impedance, radiation, and available chip area. Dipoles are usually suitable for differential feeding circuits, while monopoles for single-ended feeding. As differential feeding typical applications are related to bowtie antenna, which can enhance the antenna bandwidth [104], [105], the folded dipole which can be used for high impedance matching [106], [107] and the Yagi Uda antenna, that shows a high directional beam [108], [109]. Meanwhile, the various types of monopole on-chip antennas include triangular and circular shapes of the arm which can improve the antenna bandwidth [110]–[113]. On-chip monopole antennas are also widely used for their shorten length, which is usually only $\lambda/4$.

In comparison with conventional off-chip antennas, AoCs offer several advantages. Firstly, on-chip implementation is more feasible, in fact it integrates the complete RF front-end and the antenna directly on the same silicon die, thereby avoiding lossy interconnections. Secondly, there is no need of an impedance matching network between the antenna and RF front-end in the presence of an AoC, so the standard 50 Ω interface is not required anymore and the best performance of the system can be fulfilled by tuning the impedance of the RF-front end and of the antenna, in fact, they can be designed together in order to have their impedance coniugately matched. Finally, they provide flexibility to designers in the form of antenna and transceiver components codesign opportunity, thus saving precious chip area and design time.

Despite its high potential, this approach offers several challenges, one of them being related to the inherent low gain caused by losses in low-resistivity silicon substrates ($\rho = 10\Omega - cm$), which is beneficial for integrated circuits, as it avoids latch-up, but disastrous for on-chip antenna design. Besides, silicon substrate causes the confinement of the power in the substrate, thus reducing the portion of fields radiated into the air, this situation is related to the high dielectric constant of the silicon ($\varepsilon_R = 11.9$). All these problems are typical of CMOS or BiCMOS technologies. Another challenge is related to surface waves, which are caused by the problems listed before; they interfere with the space waves of the antenna, as shown in **Figure 5-2**, resulting in a radiation pattern with multiple nulls, causing power losses and severely influence the antenna radiation, thus resulting in low gain and low efficiency. As a result, the antenna gain is very low. The main problems are related to the silicon high permittivity and to the surface wave loss, mainly related to the thickness of the silicon substrate. The relation between the surface-waves losses, the thickness of the dielectric substrate, and the high permittivity of the substrate were previously investigated theoretically in [114].

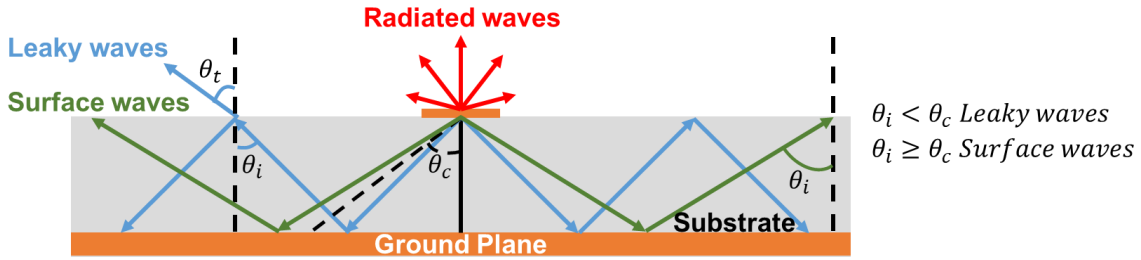

Figure 5-2: Surface waves model

What occurs in the high permittivity dielectric substrate is that the waves are partly reflected by the ground plane and partly propagate to the dielectric-air interface. If the incidence angle θ_i of the waves is smaller than a certain critical angle θ_c, the reflected waves are in part reflected by the dielectric-air interface and also in part lost into the free-

space with a refraction angle θ_t and at the same time, they can be added to the radiated waves either constructively or destructively, depending on the phases; these waves are known as leaky waves. The thickness of the dielectric substrate plays an important role, as it must be carefully chosen to maintain a good radiation efficiency. If the incidence angle θ_i is equal or larger than the certain critical angle θ_c , the incident waves are totally reflected and caught inside the dielectric substrate. These waves propagate as surface waves and can be diffracted at the edge of the dielectric substrate with a finite size. As a result, the main radiation pattern can be distorted, and multiple nulls can occur.

To solve all the problems listed before, several techniques have been proposed in literature employing dielectric resonator antennas (DRA) [115], silicon lenses [116], silicon on insulator (SOI) [117], or partially reflective surface (PRS) [110]. Other approaches include the reduction of the silicon losses through the selective removal of the silicon substrate. This approach can be implemented either using Localized Backside Etching (LBE) techniques [111], [112], [118], or other micromachining technologies [119]. Although these techniques provide a good enhancement of the gain and of the radiation efficiency, most of them suffer from higher fabrication costs, large footprint, or complex post-processing requirements. Recently, on-chip antenna gain enhancements were achieved using Artificial Magnetic Conductors (AMCs). AMCs are surfaces that fully reflect incident waves with a 0° reflection phase, as done by perfect magnetic conductors (PMCs). Therefore, they shield the antenna from the silicon substrate [120] without perturbing the radiated fields and reflect incident waves. As a result, the antenna placed over an AMC can improve the radiation efficiency of AoCs and can enhance the gain [121]. The main

drawback of AMC is related to the consumed area which has to extend around the antenna to produce the desired effect. All these aspects will be deepened in the following sections.

5.2 On-chip antennas: State of the Art

Most of on-chip antennas in the last few years have been implemented in bulk silicon-based technologies such as CMOS or SiGe BiCMOS.

CMOS technology has become the standard technology for IC designs and at the same time supports a high level of integration, offering enhanced process options, small chip-size, low power, and lower costs for mass production. Moreover, if compared to other technology such as GaAs, well-known in literature for enhancing on-chip antennas performance because of its high resistivity substrate at the cost of higher chip-area, they offer six or nine metal layers instead of two or three [103], this aspect adds flexibility for on-chip antennas design. Furthermore, the unity-gain frequency (f_t) and unity-power-gain frequency (f_{max}) of MOS transistors have now been pushed well beyond 300 GHz in some SiGe CMOS processes [122], thus enabling the realization of on-chip antennas design for mm-wave and THz applications. A large majority of recently designed on-chip antennas have used silicon-based technology, in particular SiGe BiCMOS. But the low resistivity and the high permittivity of the silicon substrates pose several challenges, which make on-chip antennas not at par with off-chip antennas. As a result, other technologies must be taken into account.

One of the main challenges in on-chip antenna design is to optimize its radiation efficiency. In literature, it is possible to find several techniques which enhance the radiation characteristics of on-chip antennas. A classification of the possible solutions can be done

by considering two alternatives. The first is related to the antenna and the second refers to the semiconductor substrate, on which the antenna is printed.

In recent years, several methods and techniques have been examined to power up the antenna efficiency of on-chip antennas. One of the first trends was that of placing a low-loss material on the top of an on-chip antenna, in order to make the antenna to radiate into free space, instead of being coupled to the silicon substrate, these techniques are linked to the use of a dielectric resonator, a superstrate, or a lens. Other possibilities include special techniques employed in order to avoid losses in the silicon substrate, such as micro-machining techniques [119] or other includes the locally removing of the silicon substrate, thus reducing the substrate losses, which are called Localized Backside Etching (LBE) [111], [112], [118], [123]. Moreover, semiconductor techniques are also beneficial for AoCs design, these are mainly thought for ICs but they have to be known to antenna design when they implement antennas in CMOS or BiCMOS technologies.

In [124] a quartz superstate was used to reduce the energy coupled into the silicon substrate for mm-wave antenna application; this method reaches at 110 GHz a 45% radiation efficiency. In [125] a phased array of transmitters with a parasitic dipole antenna on the top of the quartz superstrate achieves at 60 GHz a 50% radiation efficiency.

In [126], a Jerusalem cross AMC has been located below a Yagi Uda antenna and realized in CMOS technology and at 60 GHz the peak gain arose from -12.5 to -7.2 dBi, moreover, the radiation efficiency increased from 5% to 15%. In [127] an asymmetric AMC fulfilled a 50 % radiation efficiency. AMC structure can be used underneath AoCs to enhance the radiation efficiency.

Micro-electromechanical-system (MEMS) is yet another emerging technology that is preferred for on-chip antenna design mainly because of its compatibility with Silicon-based technologies and the capability to enhance AoCs performance. In [105] a fractal bowtie antenna was designed for dual-band operation at 60 and 77 GHz and the gain enhancement achieved is 6.5 dBi.

In [128] a dielectric resonator antenna (DRA) has been employed with a 3D on-chip antenna supported by a SIW cavity-backed antenna and a 80% radiation efficiency has been achieved, the antenna operating frequency is 340 GHz. In [129], a D-band on-chip higher-order mode Dielectric resonator antenna (DRA), fed by a half mode backed cavity structure, improved its radiation efficiency from 42% to 46%. In [130], a DRA placed over a high resistivity silicon substrate obtained a peak gain of 7 dBi with a radiation efficiency of 79.35% at 60 GHz.

Other approaches mix more than one technique to power up the performance of AoC. In [131], a THz on-chip antenna is proposed and an artificial dielectric layer is used, while the silicon substrate is removed locally by micromachining techniques; the gain enhancement achieved in this configuration is 2 dBi. In [22], to reduce the surface wave phenomena, the silicon substrate was thinned and combined with a cavity-backed structure in PCB below the AoC and a 45% radiation efficiency with a peak gain of 2 dBi at 60 GHz were achieved.

On the other hand, the use of semiconductor technology is also very common to improve the AoC performance. Silicon-on-insulator (SOI) is one of the most diffused techniques because of its high resistivity substrate that results in a significant improvement in the performance of SOI-CMOS based on-chip antennas [132]. In [133] a folded slot antenna

integrated on high resistivity silicon technology achieves a measured gain of 3.9 dBi at 60 GHz.

Through-silicon via (TSV) is another semiconductor technology in which vertical vias cross through the whole silicon wafer and it is employed in 3D ICs [134]. This technology is an alternative to bond-wire or flip-chip interconnections technologies, to reduce the lossy interconnections. As the most advanced technology, TSV greatly reduces the size of the integrated system, and at the same time reaches a good fabrication accuracy suitable for mm-wave applications. On the other hand, this process is very complex and expensive.

All the solutions presented previously deal with the improvement of the radiation efficiency of on-chip antennas, but on the other hand, they suffer from higher fabrication costs, large footprint, or complex post-processing requirements. One of the most promising solutions, which rescued particular attention in the last few years, is represented by Artificial Magnetic Conductors (AMCs), they can fulfill the same performance in bulky silicon substrate reducing fabrication difficulty, as they are thought as a shield between the antenna and the silicon substrate, as shown in **Figure 5-3**.

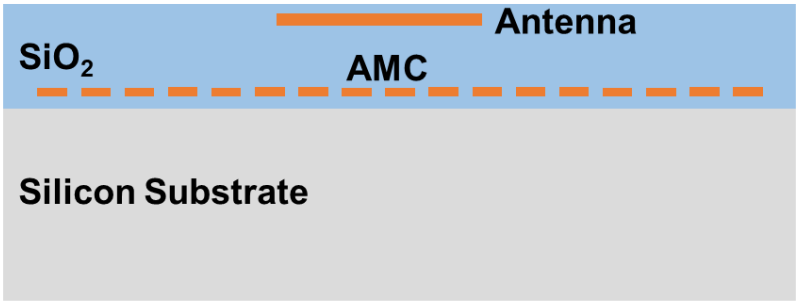

Figure 5-3: AMC concept

Planar metamaterials, having a subwavelength thickness, provide spatial variations in electromagnetic (EM) waves with scattering phases, amplitudes, and polarizations. These metamaterials, also referred as artificially engineered materials, considerably suppress

unavoidable losses in EM structures. Among metamaterials periodic structures which provide assistance in the propagation of EM wave in a specific frequency band it is possible to find: EBG (electromagnetic bandgap), HIS (high impedance surfaces), FSS (frequency selective surfaces), and PRS (partially reflective surfaces) [135].

In particular, AMC acts as HIS for the incident waves coming from the antenna to the substrate, as it produces oppositely charged image current that destructively interferes with the antenna currents. The AMC isolates the ground plane by inducing image currents in its own surface, constructively interfering with the antenna currents and boosting the antenna radiation efficiency, furthermore, AMCs can be implemented without any extra cost or complex post-processing requirements. AMCs mimic the PMC (perfect magnetic conductors) behavior, that is to say, surfaces that fully reflect waves with a 0° reflection phase, and so the reflection phase of AMCs cross zero at just one frequency. Since free magnetic charges are not known to exist in nature, there is not any material that produces scattering properties that look like those of a PMC. Furthermore, it is possible to define a useful bandwidth of an AMC as the frequency range where incident waves are reflected with a phase that varies between +90 degrees and -90 degrees since these phase values would not cause destructive interference between direct and reflected waves [120], [121].

The AMC concept was introduced for the first time by Sievenpiper in [121], where a mushroom EBG was proposed, in particular, EBG surfaces can suppress surface waves and produce bandstop or bandgap transmission and reflection characteristics at a particular frequency band. An on-chip antenna placed over an AMC can produce a smoother radiation pattern and a higher gain.

For the same purpose of AMC, split ring resonators (SRR) have been proposed. They are artificially produced structures and were proposed by Pendry in [136]. This type of resonator is well suited for on-chip implementation and its resonant frequency can be easily controlled using a combination of lumped and distributed components [137], [138]. Split ring resonators are proposed to achieve miniaturization at high frequencies [136].

Although AMCs bring various benefits, on the other hand, the main disadvantage of the AMC is linked to the consumed chip area, in fact, the AMC structure has to be extended around all the antenna to enhance the antenna performance.

For this purpose, in the following section will be presented two new techniques for enhancing the gain of on-chip antennas. In particular, they will be applied for on-chip monopole antennas.

5.3 Gain enhancement techniques for on-chip monopole antennas

As alternatives to the enhancement techniques presented in the previous section, two new methods for powering up the monopole on-chip antennas gain and radiation efficiency will be shown, both the techniques will take the W-band (75-110 GHz) as reference bandwidth. In the first configuration, a monolithically integrated AMC, represented by some SRRs, is combined with some localized backside etching (LBE). As it will be shown, LBE contribute to the gain increase as it allows selectively etching the silicon substrate below the antenna, thus creating an AMC which can reduce substrate power losses and increase the antenna radiation efficiency. In the second configuration, the monopole radiator is parasitically coupled with several split ring resonators (SRRs) capacitively loaded, which are designed to scatter the field in order to be constructively added to the one radiated by the monopole. These concepts will be proved by presenting a

W-band SRR-LBE loaded and a W-band SRR capacitively-loaded monopole antenna designed and manufactured using a standard 0.13 µm BiCMOS process. Both the configurations will follow a design flow which includes in the first part the unit cell SRR design and then the complete evaluation of the whole configuration.

5.3.1 SRR-LBE loaded monopole on-chip antenna

A first SRR loaded monopole antenna with an improved gain was designed surrounding the reference monopole antenna with a new type of AMC surface designed by combining the SRR with LBE. In this case, the SRR are acting as AMC, this type of resonator is well suited for monolithic integration and its resonant frequency can be easily controlled using a combination of lumped and distributed components. The presence of the LBE empowers the surface-wave suppression effect of a standard AMC, as the silicon is selectively removed thanks to the LBE, thus resulting in reduced substrate losses. The gain enhancement methodology proposed in this case is a combination of two techniques which are generally proposed standalone, as LBE belongs to micromachining techniques for enhancing the radiation efficiency [109], [118], [123] and the standalone SRR can be regarded as simple AMC surfaces. In this specific case, these two methodologies have been proposed together to take benefits from both the techniques and thus creating a new methodology for enhancing the on-chip monopole antenna gain.

A monopole has been selected as reference antenna, this kind of radiating element is commonly used in microwave monolithically integrated circuits (MMICs), as it can be designed to have large bandwidth and reduced size. For the case at hand, the monopole antenna is loaded with a triangular patch which serves to reduce its length and to enhance its bandwidth [139].

The technology used is IHP SG13S, a standard 0.13 μm BiCMOS process.

This process has 5 thin metal layers (M1, M2, M3, M4, and M5) whose thickness is about 0.49 µm and two top metal (TM) layers whose thickness is 2 µm for TM1 and 3 µm for TM2. LBE are a feature of the technology used, which consists in the local removal of the silicon substrate. The technology used is shown in **Figure 5-4**.

Figure 5-4: Simplified cross-section of IHP SG13S technology with LBE

In order to have an overview on the SRR-LBE behavior, which produces the desired gain and radiation efficiency enhancement, a unit cell has been taken into account, as illustrated in **Figure 5-5**. The unit cell has been designed and simulated in Ansys HFSS, by using Floquet port and Master and Slave boundaries conditions, to evaluate the periodic AMC structure in an infinite array domain [88], composed by the SRR and the LBE.

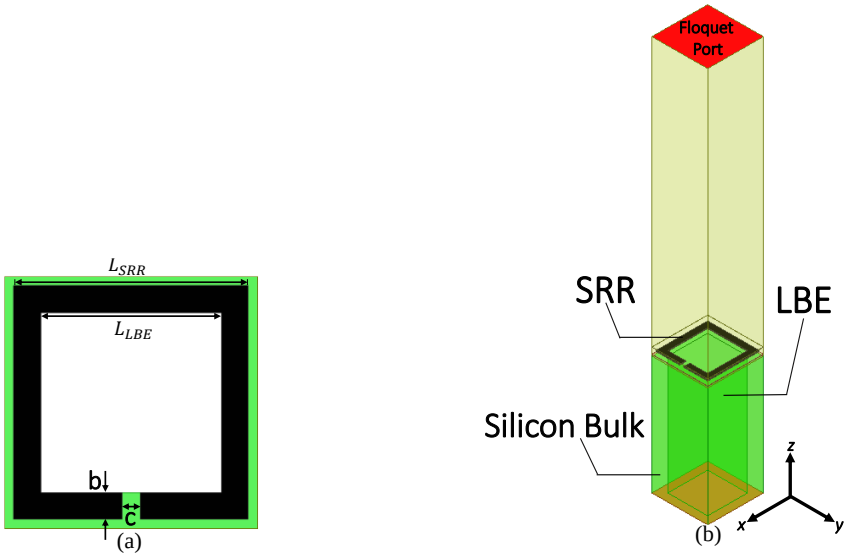

Figure 5-5: SRR-LBE unit cell: (a) Top view (b) Side view

The unit cell has been considered to get the reflection phase response of the SRR-LBE AMC. In fact, by tuning the SRR and LBE dimensions, it is possible to obtain the desired reflection phase, which is shown in **Figure 5-6**. As can be noticed, the proposed SRR-LBE AMC surface exhibits a reflection phase of 0° at 83 GHz. The frequency bandwidth is comprised between 62 GHz and 102 GHz, at which the reflection phase is within +90 degrees and -90 degrees. The optimized SRR-LBE AMC dimensions are shown in **Table 5-1**.

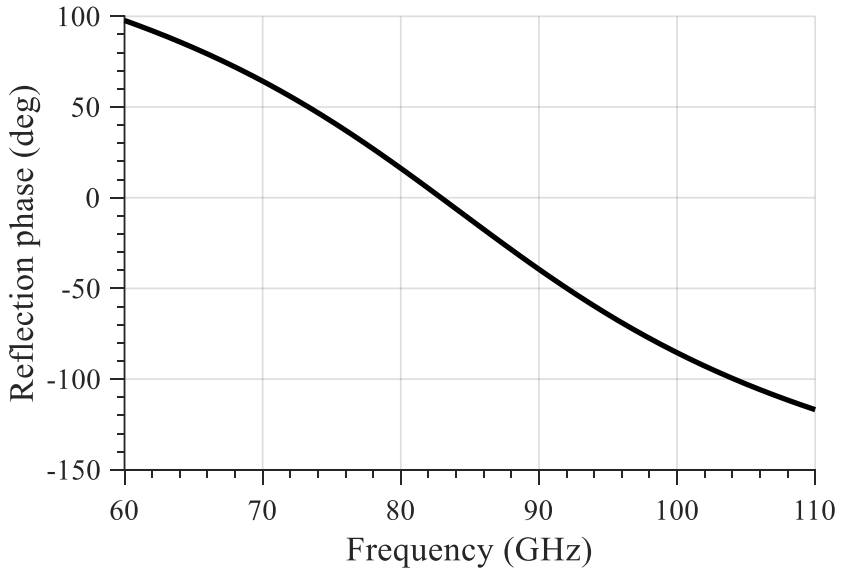

Figure 5-6: SRR-LBE unit cell AMC simulated reflection phase

Once defined the unit cell dimensions, after having evaluated its behavior, it is possible to consider the whole antenna, illustrated in **Figure 5-7**.

The monopole on-chip antenna was fed using a coplanar waveguide (CPW). As can be observed from the stackup shown in **Figure 5-4**, the antenna and the GSG pads are placed on the top level of the technology, Top Metal 2 (TM2), while the Split Ring Resonators (SRRs) are located in Top Metal 1 (TM1) level; the LBE are removed locally from the silicon substrate. The monopole dimensions are shown in **Table 5-1**. An unloaded

monopole has been taken as reference design and it has been compared with the SRR-LBE loaded antenna, in order to evaluate the effectiveness of the proposed idea. The actual structure of the proposed antenna has been simulated using the Ansys HFSS simulator [88]. It was possible to use the same dimensions, as reported in **Table 5-1**, for both the unloaded and the SRR-LBE monopole designs. After having evaluated the reflection phase of the single cell SRR-LBE in an infinite array set-up, a 7x7 array of SRR-LBE cells was placed underneath the monopole antenna and the whole structure was fine tuned. The resulting monopole antenna has a size of 1.296 x 1.508 mm^2 that is equal to the one of the reference monopole. For the case at hand, the SRR size is equal to 130 µm and the LBE size is equal to 100 µm.

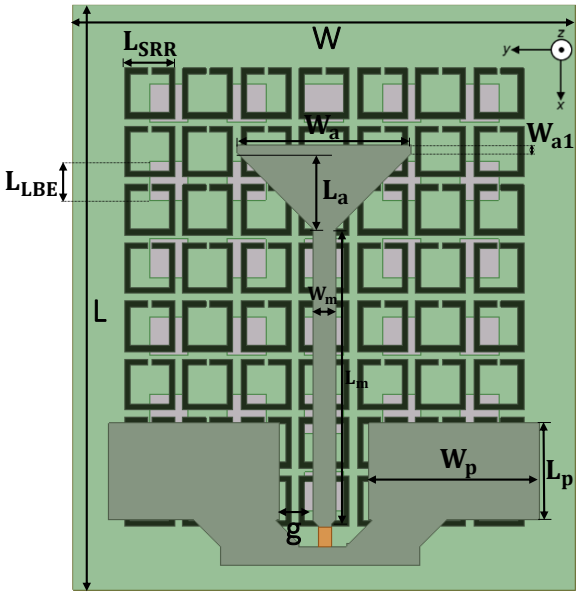

Figure 5-7: Geometry of the Monolithically integrated SRR-LBE monopole antenna

Parameters	W	L	W_m	W_a	W_{a1}	W_p	L_m	L_a	L_p	g	L_{SRR}	L_{LBE}	c	b
Value (µm)	1296	1508	60	450	19.95	440	750	195	250	85	130	100	15	10

Table 5-1: Monopole on-chip SRR-LBE loaded dimensions

The simulated reflection coefficient and the gain vs frequency response of the unloaded monopole antenna, taken as a reference, and of the SRR-LBE are reported respectively in **Figure 5-8** and **Figure 5-9**. As it can be observed, the presence of the SRR-LBE enlarges the impedance matching of the antenna.

Return loss remains below -10 dB from around 85 to 102 GHz for the unloaded case; while for the SRR-LBE loaded antenna, it maintains good performance from 85 to 105 GHz. This behavior is also evident in the gain vs frequency response, in which it is worth noticing that the presence of the SRR-LBE eliminates the gain drops of the unloaded monopole at 87 and 104 GHz. The peak gain of the SRR-LBE loaded monopole is 1.29 dBi at 87 GHz, and with respect to the unloaded monopole, there is a gain improvement of 8.6 dBi at 87 GHz. Within the band of interest, there is an average gain enhancement of about 2 dBi.

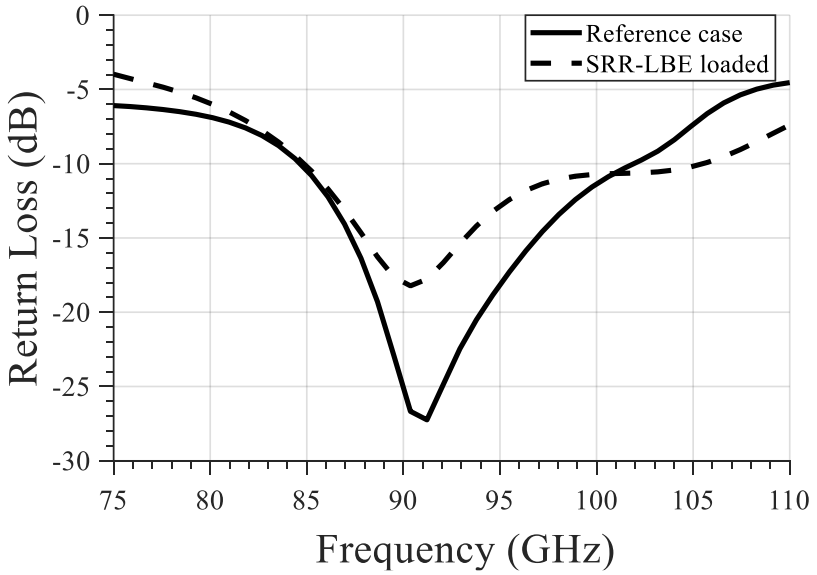

Figure 5-8: Simulated reflection coefficient of reference unloaded on-chip monopole and SRR-LBE loaded on-chip monopole

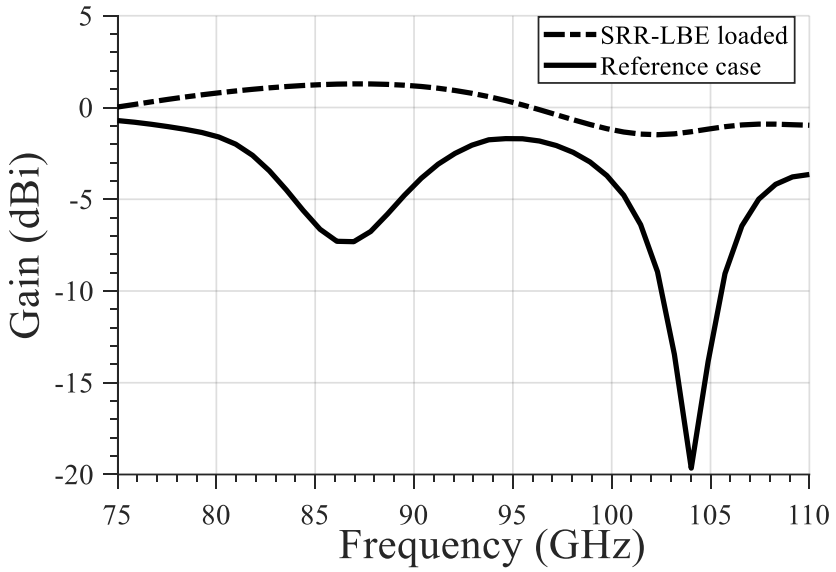

Figure 5-9: Simulated gain vs frequency response of reference unloaded on-chip monopole and SRR-LBE loaded on-chip monopole

5.3.2 SRR-LBE loaded monopole on-chip antenna

In this section will be introduced a solution to control monolithically integrated antenna gain in order to compensate for deteriorations caused by the die size or by interactions with other components present on the same MMIC. It will be demonstrated how parasitically coupled capacitively-loaded Split Ring Resonators (SRR) can be used to control the gain of a monolithically integrated monopole antenna. As shown, SRRs can be employed to constructively scatter the field of the monopole antenna and the surface waves to improve its radiation performance by canceling gain drops caused by die resonances or by other interactions taking place within the silicon chip. The gain enhancement methodology proposed in this work is widely used in conventional microstrip antennas and it has been applied to a variety of antenna geometries. For example, several studies of parasitically coupled antenna elements can be found in literature in microstrip technology [140]–[143]. In general, coupled radiating elements are used for gain improvement, to enlarge the operating band, or for reconfigurability purposes.

The design flow for this technique will be the same of the previous one: at first, a unit cell in which a SRR is loaded with a MIM capacitor will be taken into account, and then the whole monopole on-chip antenna structure will be evaluated.

The proposed work was developed using the same standard 0.13 μm SiGe BiCMOS process, as done for the previous technique, that is to say, IHP microelectronics SG13S as shown in **Figure 5-10**.

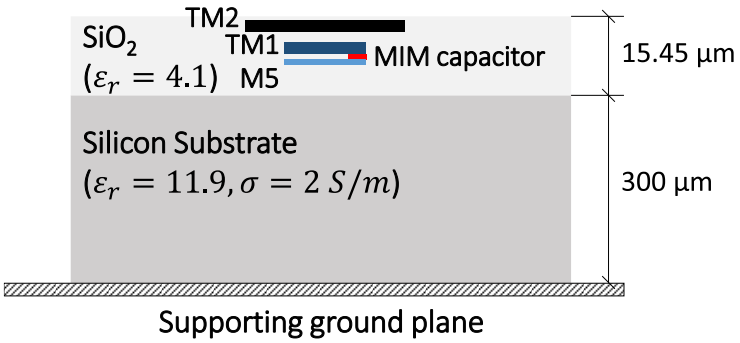

Figure 5-10: Simplified cross-section of IHP 0.13 µm SiGe BiCMOS process with MIM capacitor

As it can be observed in **Figure 5-10**, the antenna is located in the top metal layer of the technology, which is referred to as TM2, the SRR coupled elements are placed in TM1, while the MIM capacitors are located between TM1 and M5.

The characterization of the SRR was performed through an incident plane wave, as illustrated in **Figure 5-11**, using Ansys HFSS [88] to evaluate its behavior. The reflection phase response is shown in **Figure 5-12** and the null in the phase of the scattered field indicates an SRR resonance. As can be noticed, the proposed SRR capacitively-loaded surface exhibits a reflection phase of 0 degrees at 85 GHz. The frequency bandwidth is comprised between 77 GHz and 93 GHz, at which the reflection phase is within +90

degrees and -90 degrees. The optimized SRR capacitively-loaded dimensions are shown in **Table 5-2**.

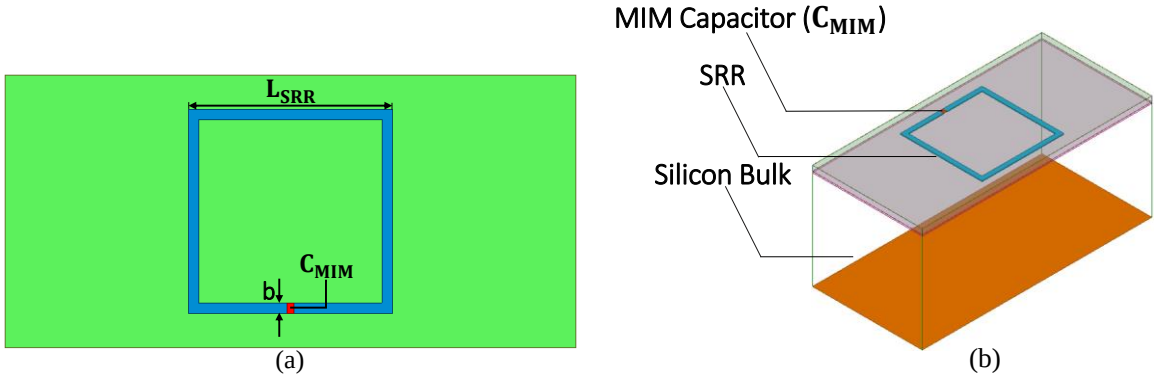

Figure 5-11: Rectangular SRR with capacitive load: (a) Top view (b) Side view

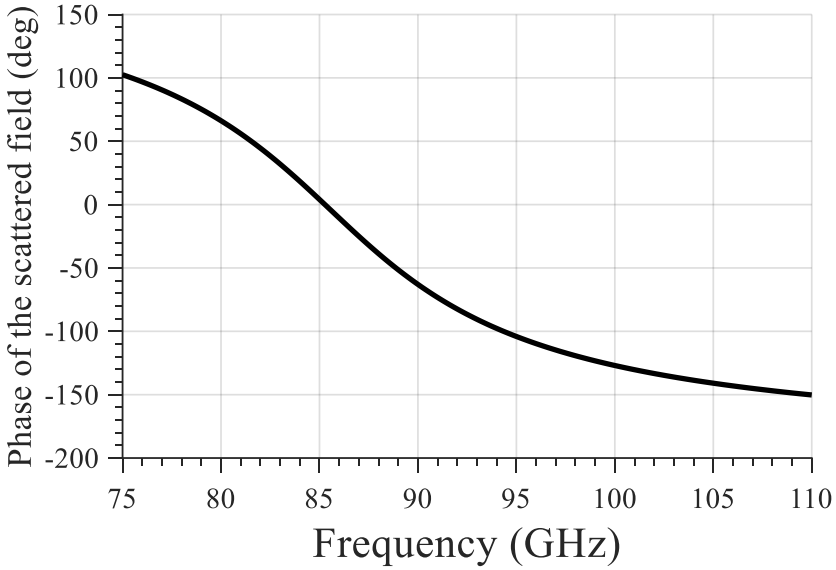

Figure 5-12: Reflection phase response of the SRR with a capacitive load

In order to evaluate the effectiveness of the proposed approach, a conventional monopole antenna was first designed and taken as a reference.

As it can be seen in **Figure 5-13**-a, the reference antenna is implemented on TM2 and it has a length L_m and width W_m. The monopole is loaded by a triangle, L_a, and its length was set to achieve a resonant frequency at around 92 GHz. The width of the triangle, W_a, was tuned to increase the bandwidth and to match the 50 Ohm input impedance [139]. The

antenna is designed to have ground reference whose width, W_p, and length, L_p, mainly controls its gain and radiation pattern. The ground reference and the monopole itself forms a coplanar waveguide (CPW) feeding configuration, which will be connected to the 50 Ohm GSG probe pads employed during the experimental characterization. The dimensions of the different geometrical parameters of the antenna are summarized in **Table 5-2**. The geometry of the SRR capacitively loaded configuration is shown in **Figure 5-13**-b. The monopole antenna is coupled to four square SRR elements. The resonant frequency of the SRRs depends on their size, L_{SRR} , and on the gap capacitance. To fine tune the latter, a monolithically integrated Metal-Insulator-Metal (MIM) capacitor was added between the SRR arms [138]. The SRRs affect the monopole performance in two ways. First, they act as a parasitic radiator, hence contributing to the overall antenna gain in relation to their resonance frequency. Second, their coupling to the monopole antenna, depending on the distance *g*, affects the monopole input impedance and reflection coefficient. Therefore, the design rationale reflects these two aspects.

For the case at hand, the SRR geometrical parameters, shown in **Table 5-2**, were set to have a resonant frequency at 85 GHz.

This resonance is expected to cancel the drop in the gain, which was present in the standalone monopole thus providing a uniform gain response over the entire operating band. Moreover, the coupling between the SRR and the monopole can be used to control the matching bandwidth of the latter antenna.

The SRR have been placed at a distance of g=85 μm from the monopole. Although higher gain values might be achieved by using a stronger coupling, in the proposed example the SRRs were designed to avoid relevant changes in the monopole impedance. Therefore, it

was possible to use the same dimensions, as reported in **Table 5-2**, for both the reference and the SRR-loaded monopole designs.

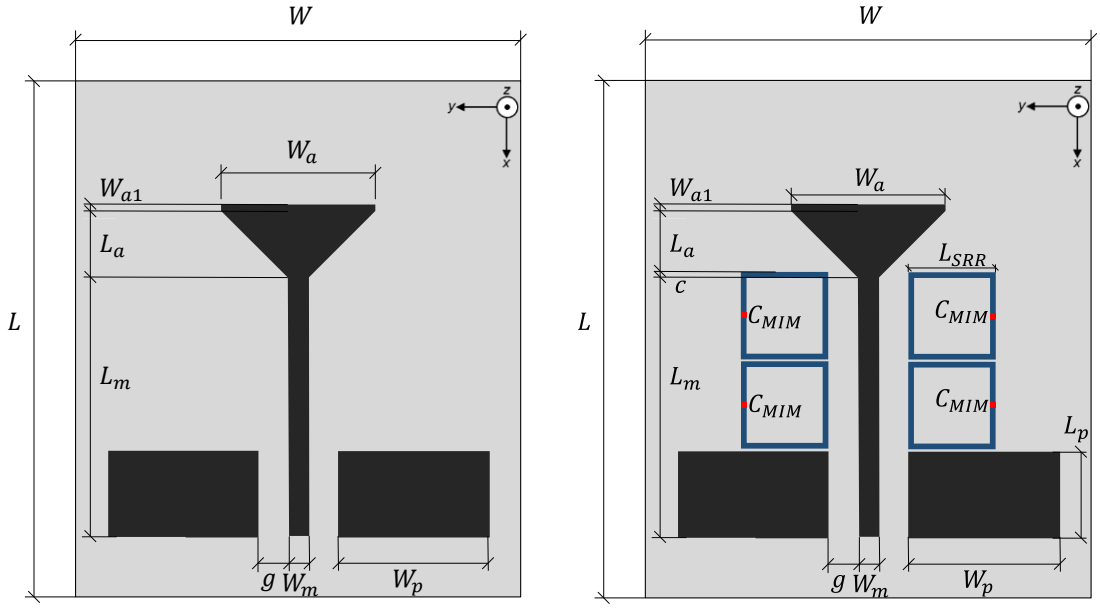

Figure 5-13: Geometry of the monolithically integrated monopole antenna (a) unloaded case (b) SRR capacitively-loaded

Parameters	**W**	**L**	**W_m**	**W_a**	**W_{a1}**	**W_p**	**L_m**	**L_a**	**L_p**	**g**	**L_{SRR}**	**b**	**C_{MIM}**
Value (μm)	1296	1508	60	450	19.95	440	750	195	250	85	250	15	250 fF

Table 5-2: Monopole on-chip SRR capacitively-loaded dimensions

The input impedances of the SRR-loaded and unloaded monopole are shown in **Figure 5-14**. The four SRRs create two additional resonances, at about 85 and 103 GHz. These values depend on the SRR geometry, on the loading capacitance, and on the coupling distance *g*. As it can be observed, higher coupling upshifts the resonance frequency of the SRR as it is seen from the antenna input port. On the other hand, the influence of the MIM capacitor is less pronounced as it only contributes to fine-tuning the input impedance [138]. The SRR resonance and coupling can be thus employed to optimize the antenna matching and to cancel the dips due to die resonances.

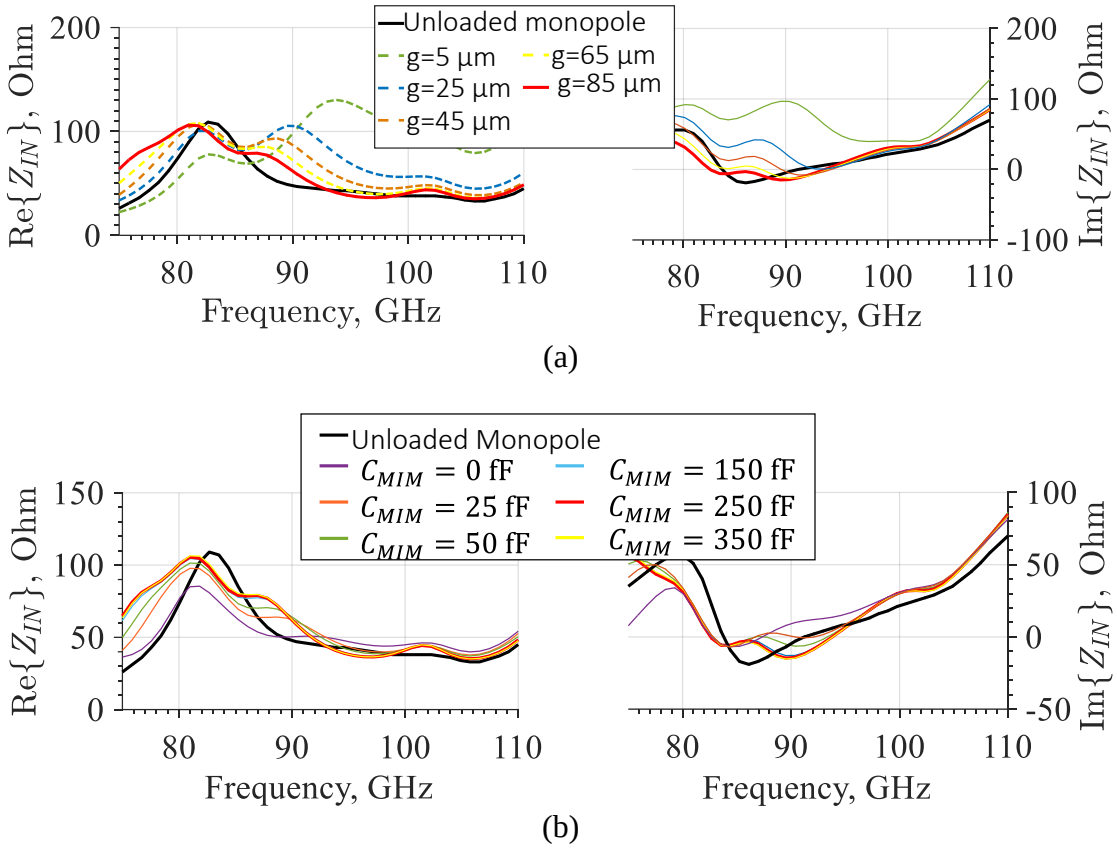

Figure 5-14: Simulated SRR capacitively-loaded on-chip monopole antenna input impedance (a) variations of the gap distance, g (b) variations of the MIM capacitor, C_{MIM}

The simulated reflection coefficient and the gain vs. frequency response of the unloaded monopole antenna taken as a reference are reported in **Figure 5-15**. As it can be observed, the minimum of the reflection coefficient is at 92 GHz where the antenna reaches a gain of -2.5 dBi. Return losses remain below -10 dB from around 85 to 102 GHz. It's also interesting to notice a gain drop at around 85 GHz.

The SRR capacitively loaded monopole antenna was designed with the objective to increase the antenna gain and to increase its uniformity within the antenna bandwidth. To this end, the use of capacitively-loaded SRRs is useful for different reasons. Firstly, the capacitance can be easily implemented in MMIC technology by adding lumped element components that are embedded into the process in the form of Metal-Insulator-Metal

(MIM) capacitors. Secondly, the presence of the capacitors adds another degree of freedom to control the resonant frequency of the rings which typically depends on their length, width, and gap. It is possible to adapt the SRR geometry to the topological needs of the circuit targeting a gain enhancement. For the case at hand, it was possible to use two square SRR on each side of the monopole while the MIM capacitor load was equal to 250 fF.

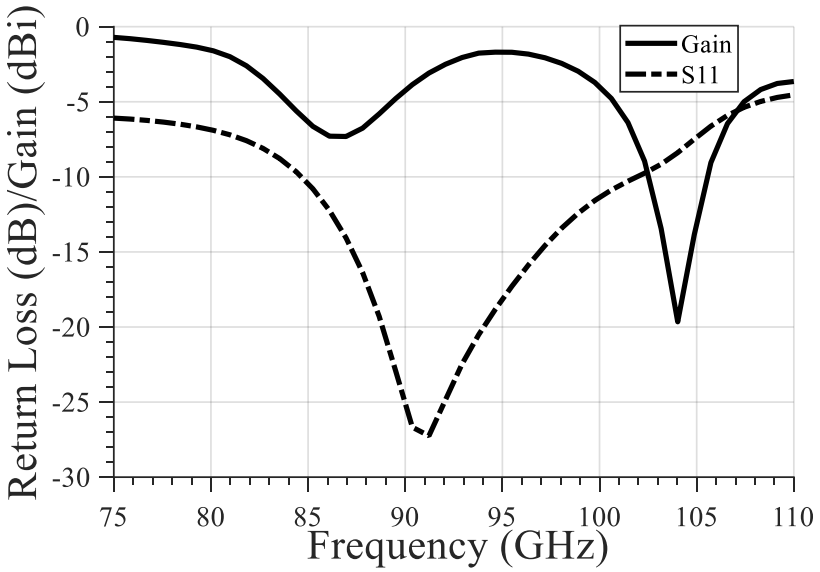

Figure 5-15: Simulated reflection coefficient and gain vs frequency response of the reference unloaded monopole on-chip

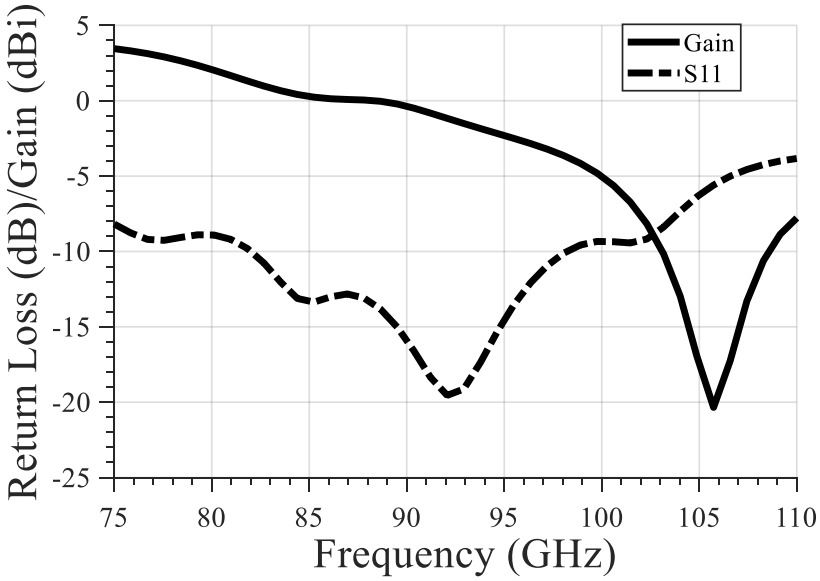

Figure 5-16: Simulated reflection coefficient and gain vs frequency response of the SRR capacitively-loaded monopole on-chip

For the SRR capacitively loaded, the simulated reflection coefficient and gain vs. frequency response are shown in **Figure 5-16**. As illustrated, the SRRs canceled the gain drop at 85 GHz by bringing its value from about -7 dBi (**Figure 5-15**) to approximately 0.6 dBi, while a peak gain of 3.46 dBi is achieved at 75 GHz. Moreover, controlling the coupling between the SRRs and the monopole allows achieving a wide matching to 50 Ohm at 85 GHz. Within the operating bandwidth (W-band), the gain response is uniform.

In order to analyze the coupling between the antenna and the parasitically coupled elements, the distribution of the surface currents on these elements was also studied. As it can be observed in **Figure 5-17**, the SRR acts as a magnetic dipole directed along the z-axis, and its radiated field sums to the one of the monopole. The H-plane coupling is mainly related to the distance between the monopole antenna and the SRRs. This parameter affects the phase offset between the monopole and the SRR fields.

It is worth noticing that the resonant frequency of the SRR mainly depends on the geometrical dimension of the ring and on the capacitive loading but it is almost independent of the monopole dimensions. As it might be expected, the SRR contribution varies as the frequency changes.

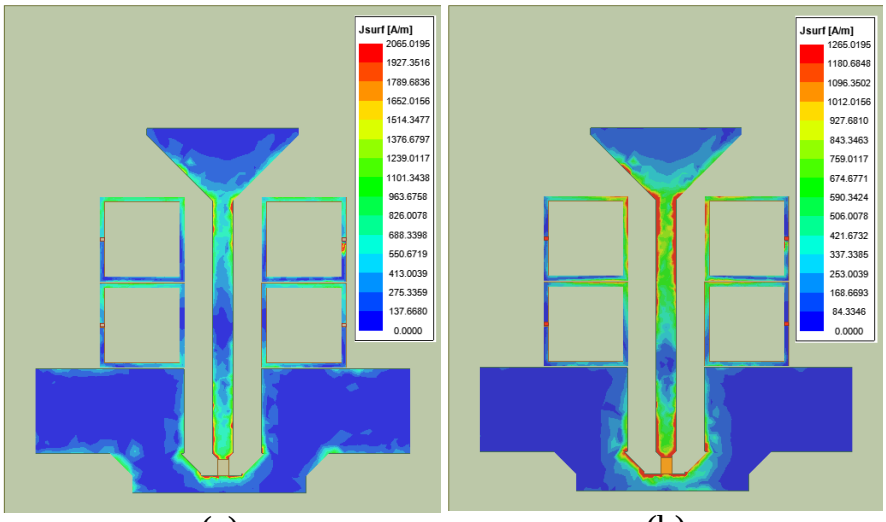

(a) (b)

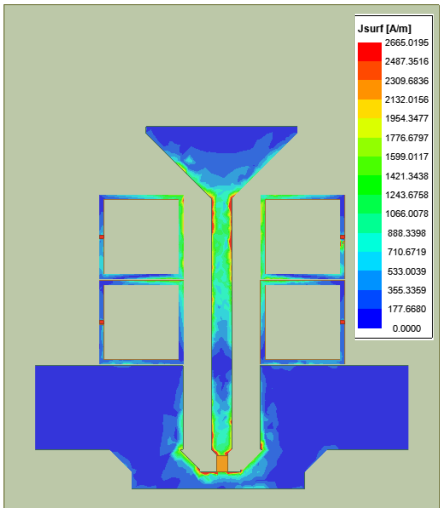

(c)

Figure 5-17: Simulated surface currents of the SRR capacitively-loaded monopole on-chip antenna: (a) 85 GHz (b) 88.3 GHz (c) 92.07 GHz

A prototype of the SRR capacitively-loaded antenna was designed and fabricated. The antenna was fed using GSG pads with a pitch of 100 µm. For this purpose, a transition from the monopole to the GSG pads was included in the layout. A microphoto of the prototype is reported in **Figure 5-18**. For measurement purposes, the die was bonded to the center of a 4×4 cm^2 ground layer using a 150 µm thick Nitto Denko REVALPHA No. 3195V glue. The glue sheet, as well as the GSG pad, were included in a full-wave simulation to reflect the test environment more accurately.

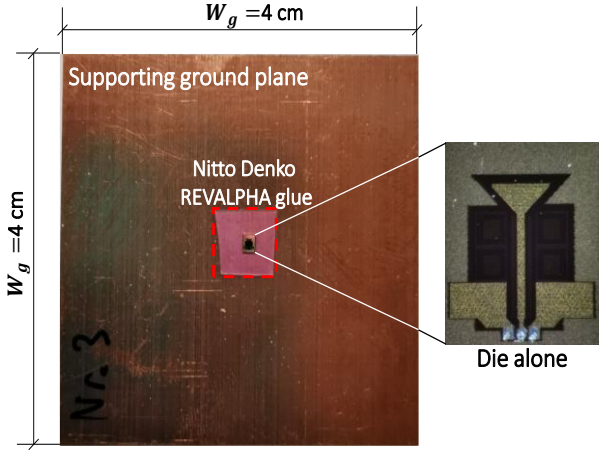

Figure 5-18: Photograph of the proposed on-chip monopole antenna attached to a 4 × 4 cm^2 ground plane

The measured reflection coefficient and gain vs frequency of the prototype are reported respectively in **Figure 5-19** and **Figure 5-20**, and they have been compared to the simulated ones in the presence of the GSG pads.

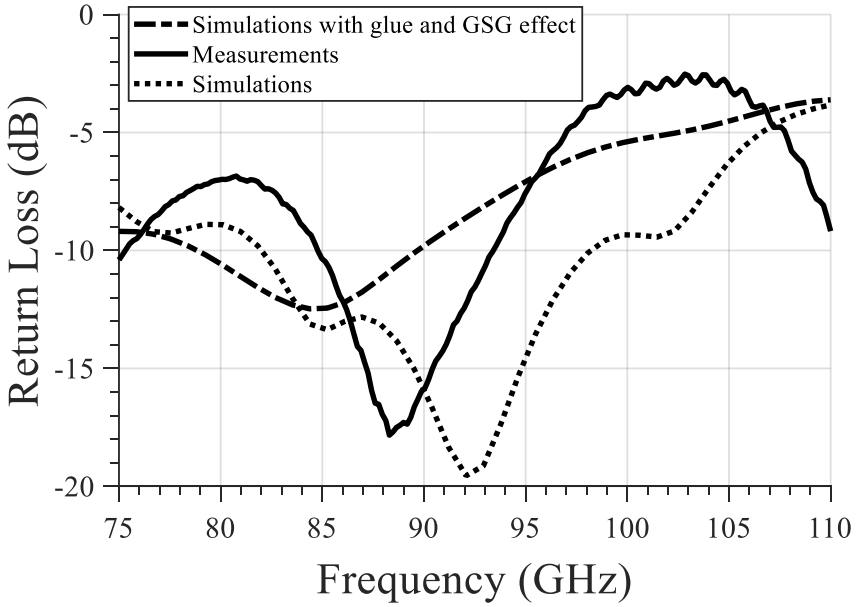

Figure 5-19: Comparison between measured and simulated reflection coefficient (without de-embedding) of the SRR capacitively-loaded monopole on-chip including ground and the glue sheet effect

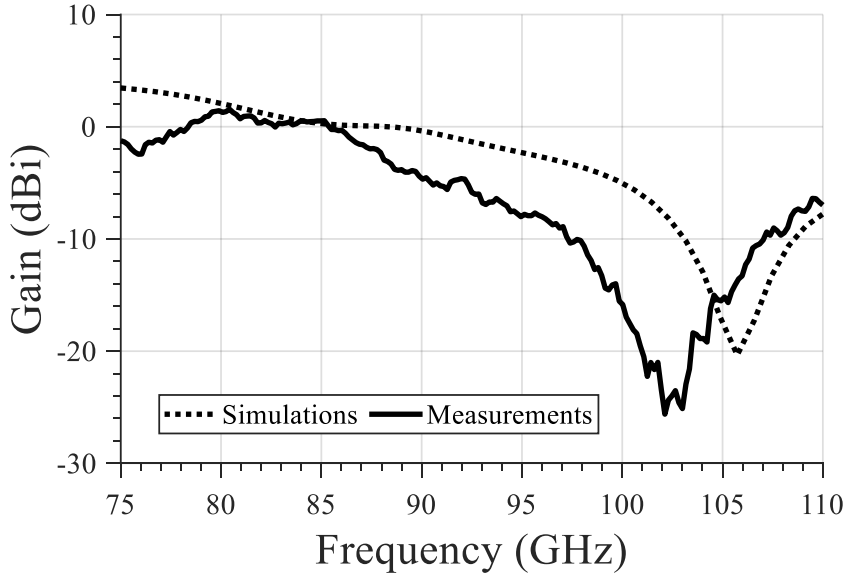

Figure 5-20: Comparison between measured and simulated gain vs frequency of the SRR capacitively-loaded monopole on-chip including ground and the glue sheet effect

The glue sheet and the GSG transition slightly upshift the antenna's operating frequency. This behavior is visible in both simulation and experimental data and it might be ascribed to the pad's capacitive loading. The measured -10 dB bandwidth of the reflection coefficient is comprised between 84.5 and 93.5 GHz. Although similar effects can be observed also in the gain response, the overall performance well matches the simulated one. In particular, the gain response is uniform within the antenna operating band, its 3-dB bandwidth is comprised between 77 GHz and 87 GHz. The gain response is uniform over the bandwidth, while the peak gain is equal to 1.61 dBi at 81.5 GHz, near the resonance frequency of the SRR. The measurements have been provided by the Karlsruhe Institute of Technology (KIT).

Measured and simulated radiation patterns are reported in **Figure 5-21** at 81.5 GHz.

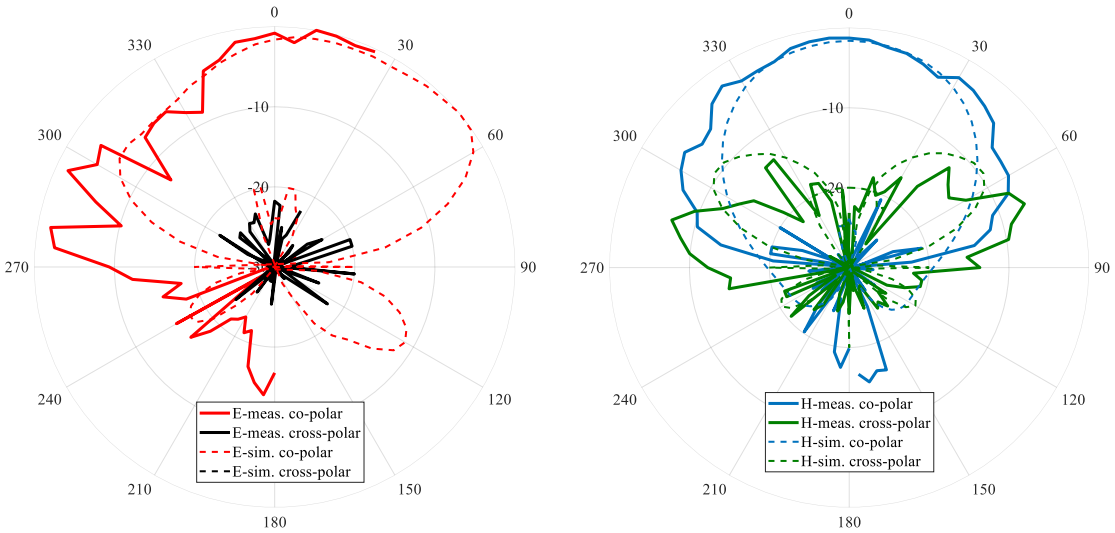

(a) (b)

Figure 5-21: Measured vs. simulated radiation patterns of the SRR-loaded monopole antenna: a) co-polar and cross-polar E-plane patterns at 81.5 GHz; b) co-polar and cross-polar H-plane patterns at 81.5 GHz

As it can be noticed, in the H-plane there is an excellent agreement between simulated and measured results. In the E-plane, the monopole tends to have a tilted pattern. This effect is visible both in the simulation and measurement. The measured data show a maximum gain in the E-plane of 2.06 dBi at around 25°. In **Figure 5-21**-a, the measured E-plane pattern shows a side lobe in the direction opposite to the GSG feeding probe.

As documented in the literature [144], [145], this effect is due to the probe itself, which distorts the radiation pattern.

This technique demonstrates how the gain of on-chip antennas can be controlled by using parasitically coupled SRR elements. Specifically, a monopole antenna operating in W-band was coupled to four capacitively-loaded SRRs. By tuning the resonance of the SRRs and their coupling with the fed radiator, one can increase the gain response's uniformity. Simulated and measured results have proved the effectiveness of the proposed technique, demonstrating how SRR can compensate for gain dips of about 5 dB while contributing to increasing the overall antenna gain. Similar effects can occur when the die is integrated into a more complex circuit or embedded within a larger MMIC.

5.4 Comparison between the proposed gain enhancement techniques for on-chip monopole antennas

After having proposed the two gain enhancement techniques separately, a comparison in terms of reflection coefficient and gain vs frequency response has been done between the two new methodologies. Both the configurations have been compared to the same unloaded monopole antenna, to prove the effectiveness of the proposed ideas. The aim of this section is to establish the best solution, between the proposed configurations, which provides a stable gain enhancement within the band of interest, and on the other

hand, which offers the best affordable solutions in terms of chip area occupation, fabrication costs, and complexity. The simulated reflection coefficient and the gain vs frequency response of the unloaded monopole antenna taken as a reference, of the SRR-LBE and of the SRR loaded case are reported respectively in **Figure 5-22** and **Figure 5-23**.

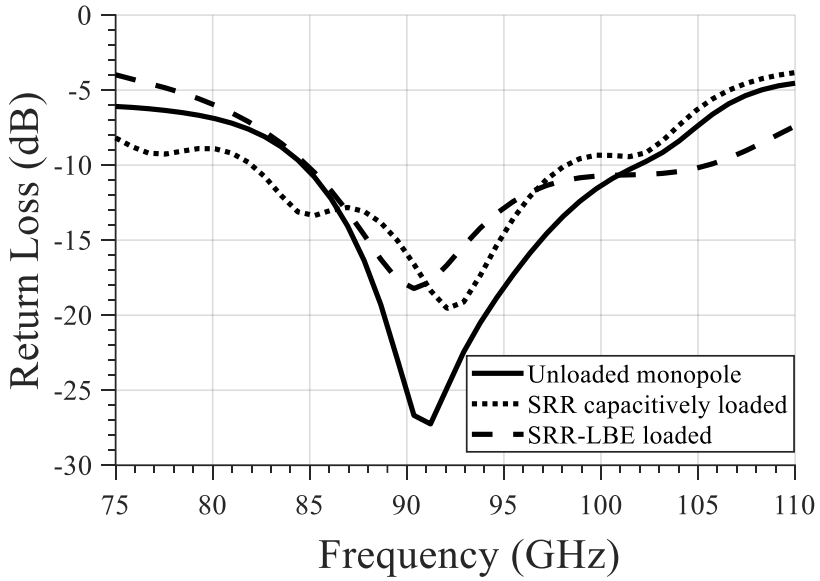

Figure 5-22: Simulated reflection coefficient of the unloaded monopole, SRR capacitively-loaded and SRR-LBE loaded

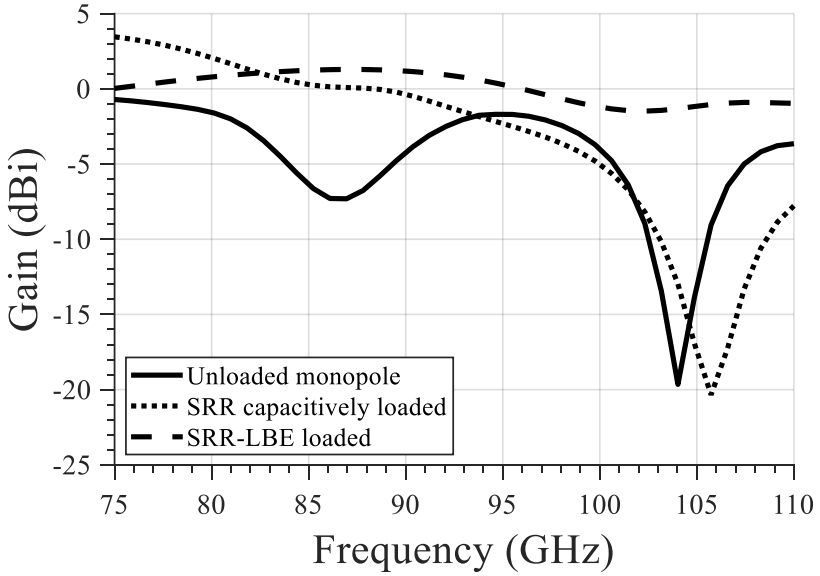

Figure 5-23: Simulated gain vs. frequency responses of the unloaded monopole, SRR capacitively-loaded and SRR-LBE loaded

As it can be observed, in the first case the presence of the SRR-LBE enlarges the impedance matching of the antenna. The return loss remains below 10 dB from around 85 to 105 GHz. In the second case, the presence of the capacitively-loaded SRR adds another peak of resonance at 85 GHz, shifting and enlarging the impedance matching of the on-chip monopole. Return loss remains below -10 dB from around 85 to 102 GHz for the unloaded case; while for the capacitively-loaded SRR antenna, it maintains good performance from 81 to 99 GHz. This behavior is also evident in the gain vs frequency response, in which the presence of the capacitively-loaded SRR, smooths the gain within the band of interest, especially in the lower W-band, where the unloaded monopole has a gain drop. On the other hand, the SRR-LBE configuration generates a gain improvement of about 2 dBi in the higher part of the band of interest.

Both the techniques provide a stable gain enhancement of about 2 dBi within the band of interest, with respect to an unloaded monopole, and can be used to improve radiation characteristics of monopole on-chip antenna. The solution with capacitively loaded SRRs appears to be more interesting as it leaves more space around the antenna for monolithically integrating other electronic circuits while the configuration based on SRR and LBE cells consumes all the silicon surrounding the radiating element. Moreover, LBE is a particular feature of the standard 0.13 μm SiGe BiCMOS technology used, which increases the cost of fabrication of the on-chip antenna. The SRR-LBE solution can be considered as a typical AMC solution which provides enhanced performance for the proposed monopole on-chip, but on the other hand, recent studies of AMC for on-chip antennas showed few limitations of the structures such as: added extra chip area, because the AMC surface extends for all the die area, which increases the overall system cost and hardware complexity.

Furthermore, some power is still lost in the silicon substrate since the ground plane of the AMC is usually designed underneath the silicon substrate. This makes on-chip antennas to need post-processing, which results in additional costs and increased design complexity [135].

For the aforementioned problems of the SRR-LBE configuration, the on-chip monopole SRR capacitively-loaded antenna appears to be the most attractive solution in terms of chip area consumption, fabrication costs, and complexity.

CHAPTER 6

E-BAND PHASE SHIFTER

6.1 Introduction

Backhauling links are the interconnections between the core of a telecommunication network and its peripheral nodes (e.g. base stations), shown in **Figure 6-1**. They are receiving increasing attention as they play a key role in sustaining the huge fronthaul data rate [146], [147]. This aspect will be further augmented in 5G networks where the proliferation of the number of cells will demand the use in large scale of high-capacity wireless backhauling links [148]. In this context, the use of point-to-point (P2P) millimeter-wave radio links (i.e. E-band, 71–76 and 81–86 GHz) is a very promising technology for several reasons: i) the high capacity that can be reached (with 10 GHz of spectrum available), ii) the very large channel bandwidths (up to 2 GHz), and iii) the links are often licensed under a "light license" process that can be obtained quickly and at a fraction of the cost of traditional link licenses.

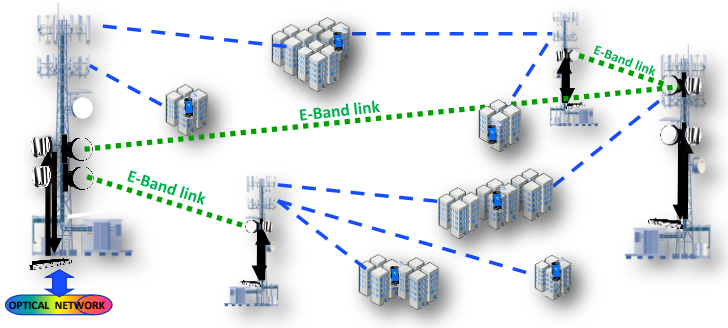

Figure 6-1: Targeted application SiGe E-band receiver for 5G Backhaul

One of the key cost drivers of the E-band backhauling networks is related to the transceiver which became a key research topic over the last few years. Transceivers should be monolithically integrated and should adapt to various modulation transmission formats, including low-power high quadrature amplitude modulation (QAM) and high-power constant envelop modulation. Therefore, the key elements of innovation are the linearity of its response, the dynamic range., and also the area from which depends the chip cost. The specific application context makes SiGe BiCMOS technologies a breakthrough in the system concept enabling a mixed-signal design including mm-wave, base-band, and digital functionalities embedded into a single chip.

In this chapter, a differential I/Q phase shifter in E-band will be presented.

The proposed design is a sub-block of a highly integrated SiGe BiCMOS E-band I/Q receiver, which covers the mm-wave band from 70 to 88 GHz and it is based on SiGe BiCMOS ST 55nm semiconductor technology [149], [150]. In particular, the E-band receiver design fully exploits the mixed-signal capabilities of the selected technology.

The whole E-band receiver was designed for the European Project Horizon 2020 TARANTO (TowARds Advanced bicmos Nano Technology platforms for rf and thz applicatiOns), while the other blocks of the receiver have been designed by other partners. For this reason, the attention in this chapter will be focused only on the phase shifter design.

The E-band receiver consists of a Low Noise Amplifier (LNA), a Variable-Gain Amplifier (VGA), a differential phase shifter on the local oscillator chain, and a double-balanced mixer that provide I and Q outputs. The block diagram of the receiver and chip photo are shown in **Figure 6-2** and **Figure 6-3**, respectively.

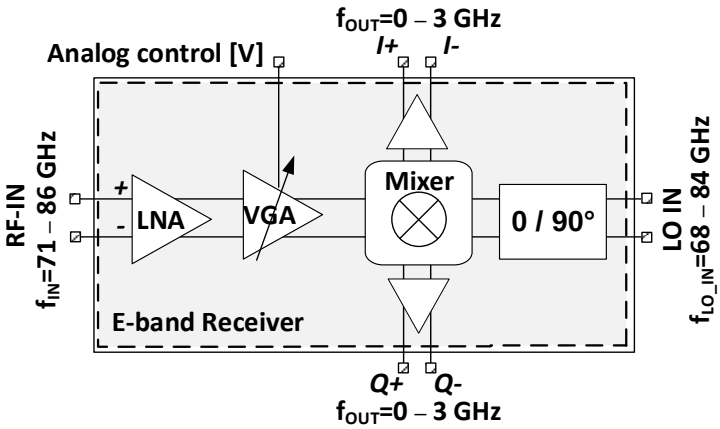

Figure 6-2: SiGe E-band receiver block diagram

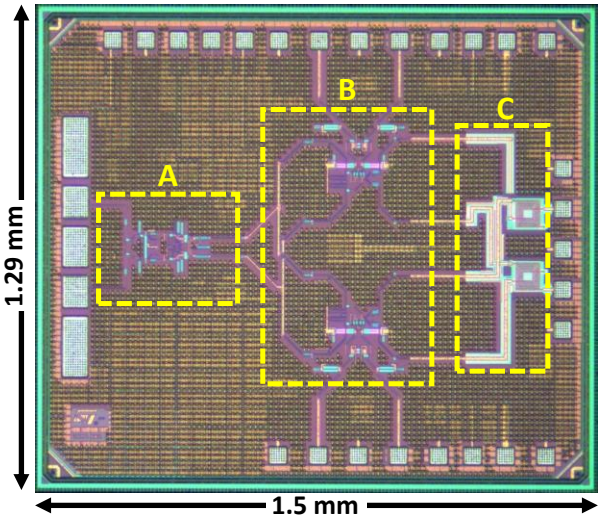

Figure 6-3: Die photograph of the E-band Receiver fabricated in BiCMOS055. In detail: A) LNA-VGA, B) I/Q mixer and output buffers, and C) 0/90° hybrid on LO chain. Die size is (1.5 x 1.29) mm^2

6.2 Differential phase shifter design

The E-Band Phase Shifter 0°/90° has been designed using ST Microelectronics 55-nm SiGe BiCMOS055 technology and it is put as input for an I/Q mixer, as illustrated in **Figure 6-3**. The combination of: i) high-frequency performance of the bipolar transistors, providing high speed and gain that are critical for high-frequency analog sections, ii) CMOS technology, excellent for building low-power logic function, and iii) Back End Of Line (BEOL) that includes an upper layer with thicker copper for improved quality factor at

mm-wave of the passive devices (inductor, capacitors, and transmission lines), makes the 55-nm SiGe BiCMOS (BiCMOS055) developed by STMicroelectronics [149] the process technology optimized for mixed-signal high-frequency IC chipsets, for applications in cellular network, mm-wave backhauling, front-hauling, satellite communication, and radar. The technology allows the design of RF circuits for applications up to 0.5 THz. The BEOL has been developed to meet the requirements of mm-wave applications and it consists of eight metallic layers and a final layer of aluminum. Moreover, the technology features Low Power (LP) and General Purpose (GP) CMOS transistors, high-quality MIM capacitors with 5fF/μm², and High-Speed HBT that exhibits f_T and f_{MAX} of 320 and 370 GHz, respectively.

The E-band differential phase shifter block has been designed to split the differential input signal from the LO input into two differential pairs in phase quadrature. To minimize the occupied area while providing a wideband response, a configuration using a pair of single-ended quadrature couplers implemented using intertwined coils was taken into account.

The E-Band phase shifter requirements are the following:

I. Operating Frequency: 60.84 GHz-87 GHz;

II. Amplitude Unbalance < 1dB;

III. Phase Unbalance < 8°.

As shown in **Figure 6-4**, it includes two coupler-based phase shifters interconnected through delay lines which are designed to provide the required phase shift to the output ports. The entire architecture was analyzed through full-wave simulations in Ansys HFSS [88] to properly design the entire layout, while the input and output port location was

agreed with the other partners of the TARANTO project, in order to make the layout seamlessly integrable with the remaining MMIC components.

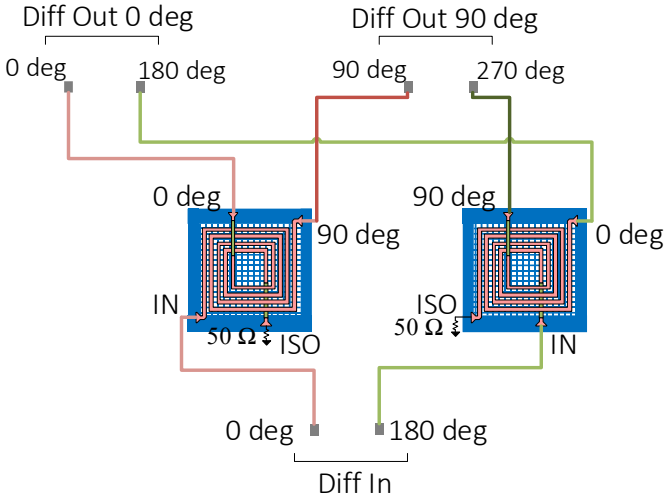

Figure 6-4: E-band phase shifter layout

The evaluation of the performance was done taking into account different parameters, the first of which is related to the phase offset between the input and output ports. The simulated values, reported in **Figure 6-5**, shows the phase of the transmitted signal, which is in line with the expected values, as every signal is shifted of 90 degrees.

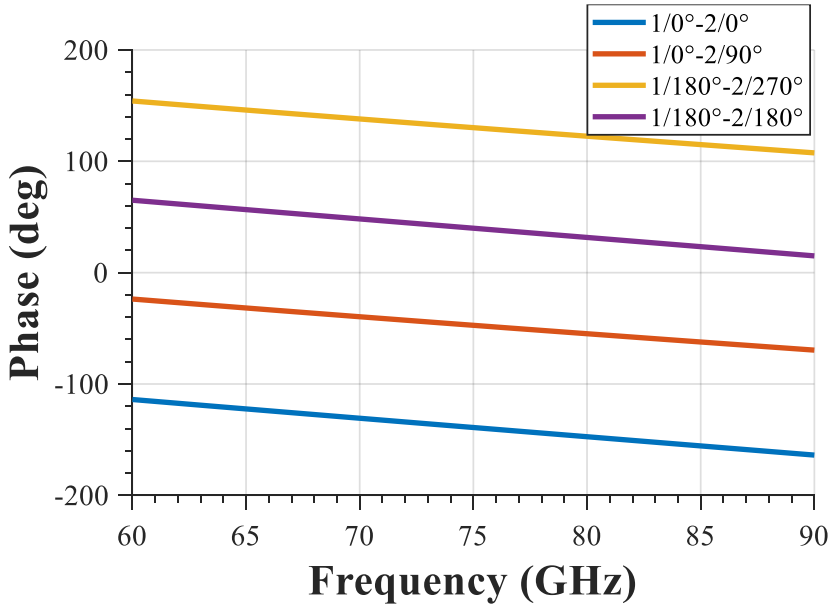

Figure 6-5: E-band phase shifter simulated output phases

The imbalance of phase offset does not exceed 8 degrees over the entire band of interest (**Figure 6-6**). The transmission losses, shown in **Figure 6-7**, indicate an amplitude imbalance between the two ports which does not exceed $\pm$0.4 dB at the two extremes of the band (60.84–87 GHz), whereas the imbalance for a single port is higher. The phase imbalance and the amplitude imbalance are defined as:

$$\text{Phase Imbalance} = < \left(-\frac{S_{31}}{S_{21}}\right) \qquad \text{Amplitude Imbalance} = \left|\frac{S_{31}}{S_{21}}\right|$$

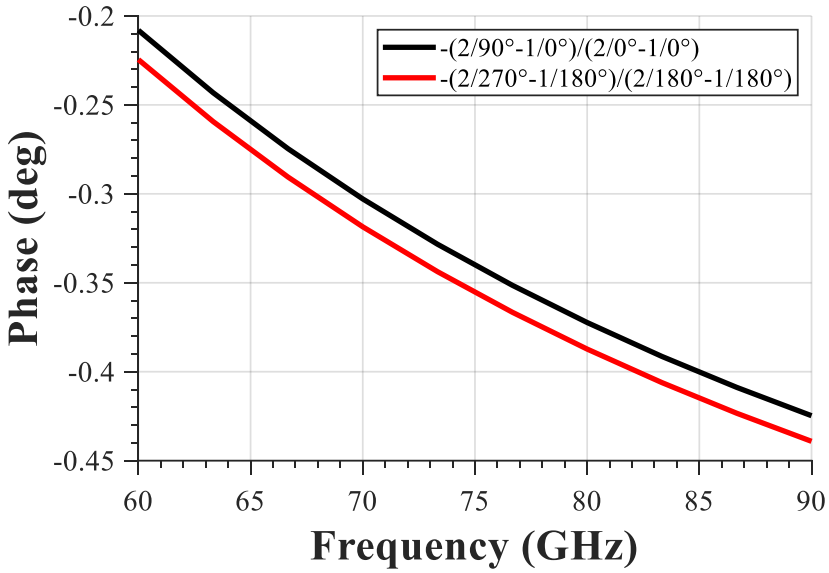

Figure 6-6: E-band phase shifter simulated phase imbalance

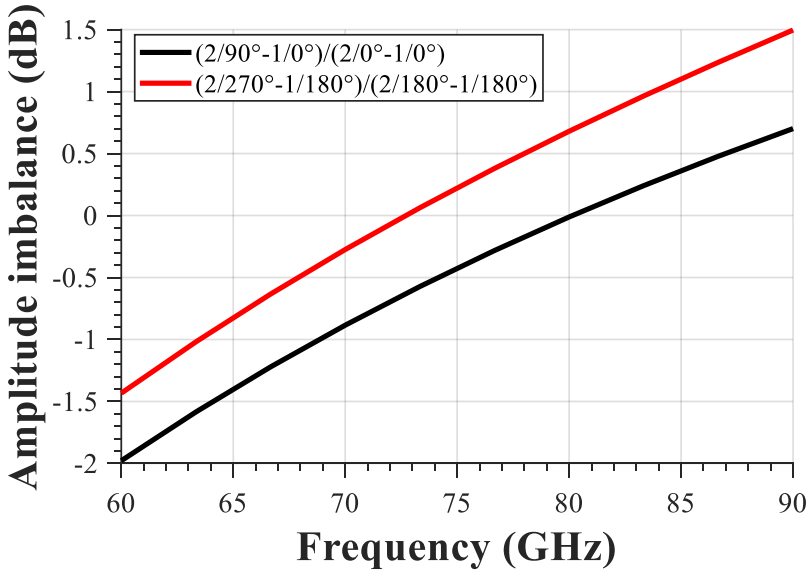

Figure 6-7: E-band phase shifter simulated amplitude imbalance

The insertion losses, reported in Fig. 35, remain below 1.5 dB while the reflection losses (Fig. 36) are less than 17 dB over the entire band.

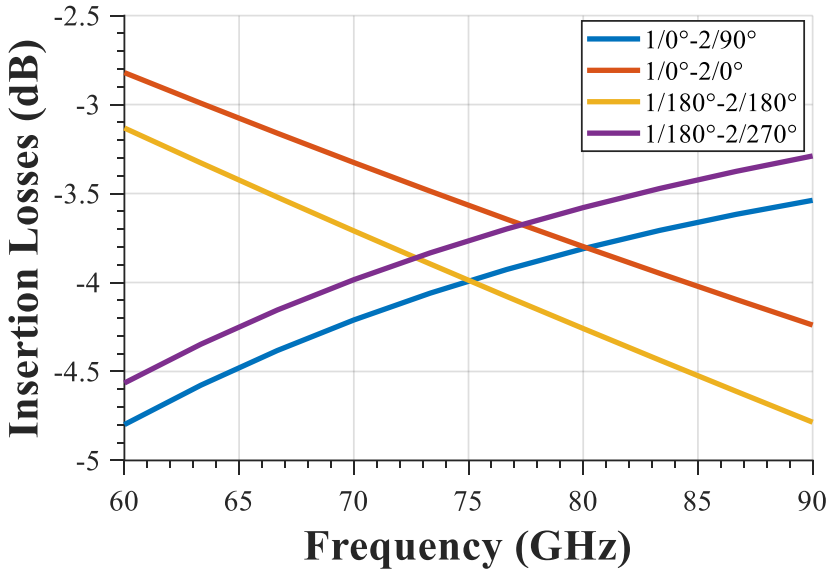

Figure 6-8: E-band phase shifter simulated Insertion Losses

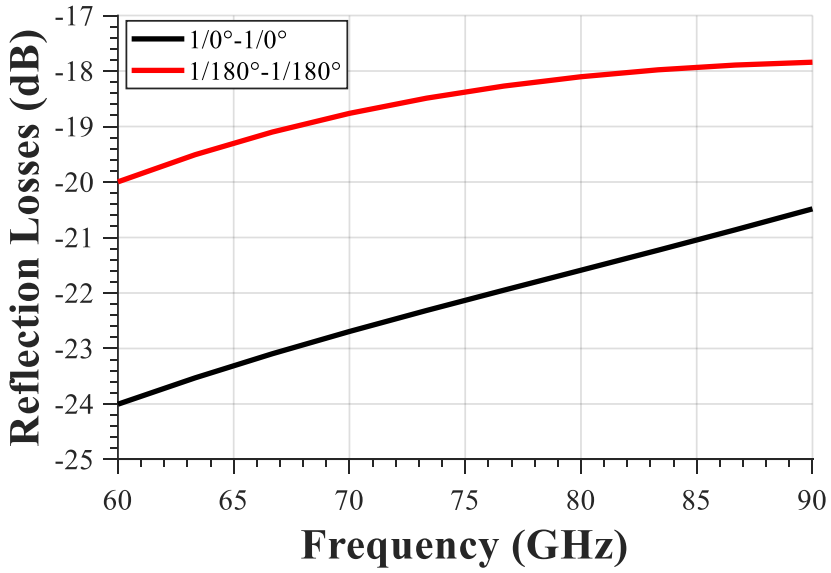

Figure 6-9: E-band phase shifter simulated Reflection Losses

In this chapter, an E-band phase shifter is presented. It is part of a compact SiGe BiCMOS I/Q receiver for backhauling applications. The novelty in the Phase Shifter design is linked to the use of two single-ended 90 degrees hybrids to create a phase shifter, with differential inputs and outputs, which is used to split the local oscillator signal in I/Q for an E-band

receiver. The hybrids were put together using delay lines, in order to achieve the required project specifications.

The whole E-band receiver, illustrated in **Figure 6-3**, was fabricated and measured. The results of the receiver are not reported in this chapter. The chip area of the E-band I/Q receiver is limited to only 1.8 mm^2.

CONCLUSION AND FUTURE WORKS

The primary object of this study is to design and analyze radiating elements for the upcoming 5G backhauling systems. An E-band beam-switched Cassegrain reflector antenna fed by an array of magneto-electric dipoles for 5G backhauling systems has been proposed. This antenna was thought to reconfigure the beam compensating small boom movements, which are estimated to be within ±1 degrees in both azimuth and elevation planes, for realizing a high gain antenna with a peak gain within the band of interest major than 50 dBi. The novelty introduced in this design is related to the use of magneto-electric dipoles as feeding elements of the Cassegrain antenna, typically these antennas are illuminated by horn antennas to realize a high gain antenna. The feeding magneto electric dipoles antenna array has been realized and it is under measurements. Future works can include the fabrication of the other proposed feeding elements for the Cassegrain configuration, such as lens antenna and Fabry-Perot cavity antennas. Furthermore, it would be very noticeable to prototype lens antennas using ABS with a 3D-printer.

Afterward, SiGe BiCMOS monolithically integrated antennas have been taken into account, taking as target monopole antennas. In particular, two techniques in W-band for enhancing the gain and the efficiency of on-chip monopole antennas have been proposed and designed. The first methodology involved the use of LBE (Localized Backside Etching) and SRRs (Split Ring Resonators), proposed as an innovative AMC (Artificial Magnetic Conductor) to power up the on-chip monopole antenna gain. The second

approach included the use of four capacitively-loaded SRRs, put around the radiating element and capable to enhance the gain of on-chip monopole antenna without consuming too much chip size. The antenna of the second technique has been prototyped, proving a good agreement between simulated and measured data. Future works can involve the use of these techniques for enhancing the gain of other on-chip antennas.

Finally, an E-band SiGe BiCMOS phase shifter has been considered. The proposed phase shifter is a sub-block of a compact E-band I/Q receiver in SiGe BiCMOS for 5G backhauling applications. Two single-ended 90 degrees hybrids have been put together with some delay lines to create a phase shifter with differential inputs and outputs, employed to split the local oscillator signal in I/Q for the E-band receiver. The overall compact receiver has been realized and tested and it provides good results.

BIBLIOGRAPHY

[1] S. Sun, B. Rong, R. Q. Hu, e Y. Qian, «Spatial Domain Management and Massive MIMO Coordination in 5G SDN», *IEEE Access*, vol. 3, pagg. 2238–2251, 2015, doi: 10.1109/ACCESS.2015.2498609.

[2] D. Cho, J. Kim, e I. Kim, «Outdoor Demonstration of 5Gbps MHN Enhanced System», in *2018 Tenth International Conference on Ubiquitous and Future Networks (ICUFN)*, lug. 2018, pagg. 886–890, doi: 10.1109/ICUFN.2018.8436782.

[3] S. Y. Zheng, Z. L. Su, Y. M. Pan, Z. Qamar, e D. Ho, «New Dual-/Tri-Band Bandpass Filters and Diplexer With Large Frequency Ratio», *IEEE Transactions on Microwave Theory and Techniques*, vol. 66, n. 6, pagg. 2978–2992, giu. 2018, doi: 10.1109/TMTT.2018.2833862.

[4] R. H. Nakata, B. Haruna, T. Yamaguchi, V. M. Lubecke, S. Takayama, e K. Takaba, «Motion Compensation for an Unmanned Aerial Vehicle Remote Radar Life Sensor», *IEEE Journal on Emerging and Selected Topics in Circuits and Systems*, vol. 8, n. 2, pagg. 329–337, giu. 2018, doi: 10.1109/JETCAS.2018.2821624.

[5] S. Y. Zheng, «A Dual-Band Antenna accross Microwave and Millimeter-wave Frequency Bands», in *2018 International Applied Computational Electromagnetics Society Symposium - China (ACES)*, lug. 2018, pagg. 1–2, doi: 10.23919/ACESS.2018.8669229.

[6] N. Kanthasamy, R. V. Cowlagi, e A. M. Wyglinski, «State Estimation for Mitigating Positioning Errors in V2V Networks Employing Dual Beamforming», in *2018 IEEE 88th Vehicular Technology Conference (VTC-Fall)*, ago. 2018, pagg. 1–5, doi: 10.1109/VTCFall.2018.8690869.

[7] D. Sharma, S. K. Dubey, e V. N. Ojha, «Wearable Antenna for millimeter wave 5G Communications», in *2018 IEEE Indian Conference on Antennas and Propogation (InCAP)*, dic. 2018, pagg. 1–4, doi: 10.1109/INCAP.2018.8770921.

[8] W. S. Tang, Z. L. Su, e S. Y. Zheng, «Dual-Band Bandpass Filter with Large Frequency Ratio and Independently Tunable Center Frequencies», in *2019 IEEE MTT-S International Wireless Symposium (IWS)*, mag. 2019, pagg. 1–3, doi: 10.1109/IEEE-IWS.2019.8804022.

[9] Y. Kim, I. Lee, e S. Jeon, «A New mm-Wave Multiple-Band Single-Pole Multiple-Throw Switch With Variable Transmission Lines», *IEEE Transactions on Microwave Theory and Techniques*, vol. 68, n. 7, pagg. 2551–2561, lug. 2020, doi: 10.1109/TMTT.2020.2988863.

[10] A. Delmade *et al.*, «Optical Heterodyne Analog Radio-Over-Fiber Link for Millimeter-Wave Wireless Systems», *Journal of Lightwave Technology*, vol. 39, n. 2, pagg. 465–474, gen. 2021, doi: 10.1109/JLT.2020.3032923.

[11] I. T. AG, «How does 5G work? - Infineon Technologies». https://www.infineon.com/cms/en/discoveries/mobile-communication-5g/ (consultato gen. 02, 2021).

[12] D. Choudhury, «5G wireless and millimeter wave technology evolution: An overview», in *2015 IEEE MTT-S International Microwave Symposium*, mag. 2015, pagg. 1–4, doi: 10.1109/MWSYM.2015.7167093.

[13] M. Bennis, M. Debbah, e H. V. Poor, «Ultrareliable and Low-Latency Wireless Communication: Tail, Risk, and Scale», *Proceedings of the IEEE*, vol. 106, n. 10, pagg. 1834–1853, ott. 2018, doi: 10.1109/JPROC.2018.2867029.

[14] G. Brown, «Ultra-Reliable Low-Latency 5G for Industrial Automation», pag. 11.

[15] «5G RF For Dummies® E-Book 2nd Edition - Qorvo». https://www.qorvo.com/design-hub/ebooks/5g-rf-for-dummies (consultato gen. 02, 2021).

[16] «ts_138104v150400p.pdf». Consultato: gen. 02, 2021. [Online]. Disponibile su: https://www.etsi.org/deliver/etsi_ts/138100_138199/138104/15.04.00_60/ts_138104v150400p.pdf.

[17] «ts_138104v150500p.pdf». Consultato: gen. 02, 2021. [Online]. Disponibile su: https://www.etsi.org/deliver/etsi_ts/138100_138199/138104/15.05.00_60/ts_138104v150500p.pdf.

[18] «ts_138104v160400p.pdf». Consultato: gen. 02, 2021. [Online]. Disponibile su: https://www.etsi.org/deliver/etsi_ts/138100_138199/138104/16.04.00_60/ts_138104v160400p.pdf.

[19] «the-3gpp-release-15-5g-nr-design.pdf». Consultato: gen. 02, 2021. [Online]. Disponibile su: https://www.qualcomm.com/media/documents/files/the-3gpp-release-15-5g-nr-design.pdf.

[20] A. O. Watanabe, M. Ali, S. Y. B. Sayeed, R. R. Tummala, e P. M. Raj, «A Review of 5G Front-End Systems Package Integration», *IEEE Transactions on Components, Packaging and Manufacturing Technology*, pagg. 1–1, 2020, doi: 10.1109/TCPMT.2020.3041412.

[21] S. Parkvall, E. Dahlman, A. Furuskar, e M. Frenne, «NR: The New 5G Radio Access Technology», *IEEE Communications Standards Magazine*, vol. 1, n. 4, pagg. 24–30, dic. 2017, doi: 10.1109/MCOMSTD.2017.1700042.

[22] B. B. Adela, P. T. M. van Zeijl, U. Johannsen, e A. B. Smolders, «On-Chip Antenna Integration for Millimeter-Wave Single-Chip FMCW Radar, Providing High Efficiency and Isolation», *IEEE Transactions on Antennas and Propagation*, vol. 64, n. 8, pagg. 3281–3291, ago. 2016, doi: 10.1109/TAP.2016.2570228.

[23] A. B. Smolders *et al.*, «Building 5G Millimeter-Wave Wireless Infrastructure: Wide-Scan Focal-Plane Arrays With Broadband Optical Beamforming», *IEEE Antennas and Propagation Magazine*, vol. 61, n. 2, pagg. 53–62, apr. 2019, doi: 10.1109/MAP.2019.2895662.

[24] «R-REP-M.2412-2017-PDF-E.pdf». Consultato: gen. 03, 2021. [Online]. Disponibile su: https://www.itu.int/dms_pub/itu-r/opb/rep/R-REP-M.2412-2017-PDF-E.pdf.

[25] W. Hong *et al.*, «Multibeam Antenna Technologies for 5G Wireless Communications», *IEEE Transactions on Antennas and Propagation*, vol. 65, n. 12, pagg. 6231–6249, dic. 2017, doi: 10.1109/TAP.2017.2712819.

[26] H. Huang, «Overview of antenna designs and considerations in 5G cellular phones», in *2018 International Workshop on Antenna Technology (iWAT)*, mar. 2018, pagg. 1–4, doi: 10.1109/IWAT.2018.8379253.

[27] I. F. Akyildiz, X. Wang, e W. Wang, «Wireless mesh networks: a survey», *Computer Networks*, vol. 47, n. 4, pagg. 445–487, mar. 2005, doi: 10.1016/j.comnet.2004.12.001.

[28] T. Sharma, A. Chehri, e P. Fortier, «Review of optical and wireless backhaul networks and emerging trends of next generation 5G and 6G technologies», *Transactions on Emerging Telecommunications Technologies*, vol. n/a, n. n/a, pag. e4155, doi: https://doi.org/10.1002/ett.4155.

[29] A. Slalmi, H. Kharraz, R. Saadane, C. Hasna, A. Chehri, e G. Jeon, «Energy Efficiency Proposal for IoT Call Admission Control in 5G Network», in *2019 15th International Conference on Signal-Image Technology Internet-Based Systems (SITIS)*, nov. 2019, pagg. 396–403, doi: 10.1109/SITIS.2019.00070.

[30] «Mobile-Backhaul-Options.pdf». Consultato: gen. 10, 2021. [Online]. Disponibile su: https://www.gsma.com/spectrum/wp-content/uploads/2019/04/Mobile-Backhaul-Options.pdf.

[31] «MW & mmW spectrum for 5G wireless backhaul». [Online]. Disponibile su: https://www.itu.int/en/ITU-R/study-groups/workshops/fsimt2020/Documents/1-Wireless%20Backhaul%20for%20IMT%202020-5G%20-%20Overview%20and%20introduction.pdf.

[32] F. Schwering e A. A. Oliner, «Millimeter-Wave Antennas», in *Antenna Handbook: Volume III Applications*, Y. T. Lo e S. W. Lee, A c. di Boston, MA: Springer US, 1993, pagg. 1–148.

[33] A. F. Kay, «Millimeter wave antennas», *Proceedings of the IEEE*, vol. 54, n. 4, pagg. 641–647, apr. 1966, doi: 10.1109/PROC.1966.4785.

[34] J. Ala-Laurinaho *et al.*, «2-D Beam-Steerable Integrated Lens Antenna System for 5G E -Band Access and Backhaul», *IEEE Transactions on Microwave Theory and Techniques*, vol. 64, n. 7, pagg. 2244–2255, lug. 2016, doi: 10.1109/TMTT.2016.2574317.

[35] A. Bisognin *et al.*, «Ball Grid Array-Module With Integrated Shaped Lens for WiGig Applications in Eyewear Devices», *IEEE Transactions on Antennas and Propagation*, vol. 64, n. 3, pagg. 872–882, mar. 2016, doi: 10.1109/TAP.2016.2517667.

[36] A. N. Plastikov, «A High-Gain Multibeam Bifocal Reflector Antenna With 40° Field of View for Satellite Ground Station Applications», *IEEE Transactions on Antennas and Propagation*, vol. 64, n. 7, pagg. 3251–3254, lug. 2016, doi: 10.1109/TAP.2016.2560918.

[37] J. Wang, J. xiang Ge, Y. Zhou, H. Xia, e X. zhi Yang, «Design of a High-Isolation 35/94-GHz Dual-Frequency Orthogonal-Polarization Cassegrain Antenna», *IEEE Antennas and Wireless Propagation Letters*, vol. 16, pagg. 1297–1300, 2017, doi: 10.1109/LAWP.2016.2633284.

[38] Z. Hao, M. He, K. Fan, e G. Luo, «A Planar Broadband Antenna for the E-Band Gigabyte Wireless Communication», *IEEE Transactions on Antennas and Propagation*, vol. 65, n. 3, pagg. 1369–1373, mar. 2017, doi: 10.1109/TAP.2016.2635590.

[39] M. Li e K. Luk, «Low-Cost Wideband Microstrip Antenna Array for 60-GHz Applications», *IEEE Transactions on Antennas and Propagation*, vol. 62, n. 6, pagg. 3012–3018, giu. 2014, doi: 10.1109/TAP.2014.2311994.

[40] E. Levine, G. Malamud, S. Shtrikman, e D. Treves, «A study of microstrip array antennas with the feed network», *IEEE Transactions on Antennas and Propagation*, vol. 37, n. 4, pagg. 426–434, apr. 1989, doi: 10.1109/8.24162.

[41] M. Zhang, J. Hirokawa, e M. Ando, «An E-Band Partially Corporate Feed Uniform Slot Array With Laminated Quasi Double-Layer Waveguide and Virtual PMC Terminations», *IEEE Transactions on Antennas and Propagation*, vol. 59, n. 5, pagg. 1521–1527, mag. 2011, doi: 10.1109/TAP.2011.2122301.

[42] A. Vosoogh e P. Kildal, «Corporate-Fed Planar 60-GHz Slot Array Made of Three Unconnected Metal Layers Using AMC Pin Surface for the Gap Waveguide», *IEEE Antennas and Wireless Propagation Letters*, vol. 15, pagg. 1935–1938, 2016, doi: 10.1109/LAWP.2015.2510296.

[43] D. Zarifi, A. Farahbakhsh, A. U. Zaman, e P. Kildal, «Design and Fabrication of a High-Gain 60-GHz Corrugated Slot Antenna Array With Ridge Gap Waveguide Distribution Layer», *IEEE Transactions on Antennas and Propagation*, vol. 64, n. 7, pagg. 2905–2913, lug. 2016, doi: 10.1109/TAP.2016.2565682.

[44] X. Chen, K. Wu, L. Han, e F. He, «Low-Cost High Gain Planar Antenna Array for 60-GHz Band Applications», *IEEE Transactions on Antennas and Propagation*, vol. 58, n. 6, pagg. 2126–2129, giu. 2010, doi: 10.1109/TAP.2010.2046861.

[45] G. Q. Luo, Z. F. Hu, W. J. Li, X. H. Zhang, L. L. Sun, e J. F. Zheng, «Bandwidth-Enhanced Low-Profile Cavity-Backed Slot Antenna by Using Hybrid SIW Cavity Modes», *IEEE Transactions on Antennas and Propagation*, vol. 60, n. 4, pagg. 1698–1704, apr. 2012, doi: 10.1109/TAP.2012.2186226.

[46] S. Da, Y. Li, e J. Wang, «Air-Filled Substrate Integrated Waveguide Fed Magneto-Electric Dipole Antenna Array for Millimeter-Wave Applications», *IEEE Access*, vol. 7, pagg. 129307–129316, 2019, doi: 10.1109/ACCESS.2019.2939873.

[47] Z. Hao, Q. Yuan, B. Li, e G. Q. Luo, «Wideband W -Band Substrate-Integrated Waveguide Magnetoelectric (ME) Dipole Array Antenna», *IEEE Transactions on Antennas and Propagation*, vol. 66, n. 6, pagg. 3195–3200, giu. 2018, doi: 10.1109/TAP.2018.2820503.

[48] T. Tomura, J. Hirokawa, T. Hirano, e M. Ando, «A 45° Linearly Polarized Hollow-Waveguide 16 $\,\times$16-Slot Array Antenna Covering 71–86 GHz Band», *IEEE Transactions on Antennas and Propagation*, vol. 62, n. 10, pagg. 5061–5067, ott. 2014, doi: 10.1109/TAP.2014.2345567.

[49] Y. Li e K. Luk, «60-GHz Dual-Polarized Two-Dimensional Switch-Beam Wideband Antenna Array of Aperture-Coupled Magneto-Electric Dipoles», *IEEE Transactions on Antennas and Propagation*, vol. 64, n. 2, pagg. 554–563, feb. 2016, doi: 10.1109/TAP.2015.2507170.

[50] Q. Zhu, K. B. Ng, C. H. Chan, e K. Luk, «Substrate-Integrated-Waveguide-Fed Array Antenna Covering 57–71 GHz Band for 5G Applications», *IEEE Transactions on Antennas and Propagation*, vol. 65, n. 12, pagg. 6298–6306, dic. 2017, doi: 10.1109/TAP.2017.2723080.

[51] Y. J. Cheng, Y. X. Guo, e Z. G. Liu, «W-Band Large-Scale High-Gain Planar Integrated Antenna Array», *IEEE Transactions on Antennas and Propagation*, vol. 62, n. 6, pagg. 3370–3373, giu. 2014, doi: 10.1109/TAP.2014.2310483.

[52] D. Zarifi, A. Farahbakhsh, e A. U. Zaman, «A Gap Waveguide-Fed Wideband Patch Antenna Array for 60-GHz Applications», *IEEE Transactions on Antennas and*

Propagation, vol. 65, n. 9, pagg. 4875–4879, set. 2017, doi: 10.1109/TAP.2017.2722866.

[53] H. Irie e J. Hirokawa, «Perpendicular-Corporate Feed in Three-Layered Parallel-Plate Radiating-Slot Array», *IEEE Transactions on Antennas and Propagation*, vol. 65, n. 11, pagg. 5829–5836, nov. 2017, doi: 10.1109/TAP.2017.2751659.

[54] A. Boriskin e R. Sauleau, A c. di, *Aperture Antennas for Millimeter and Sub-Millimeter Wave Applications*. Springer International Publishing, 2018.

[55] L. Wang, Y. J. Cheng, D. Ma, e C. X. Weng, «Wideband and Dual-Band High-Gain Substrate Integrated Antenna Array for E-Band Multi-Gigahertz Capacity Wireless Communication Systems», *IEEE Transactions on Antennas and Propagation*, vol. 62, n. 9, pagg. 4602–4611, set. 2014, doi: 10.1109/TAP.2014.2334357.

[56] J. Hesselbarth, D. L. Cuenca, e H. B. Molina, «Millimeter-wave front-end integration concept using beam-switched lens antenna», in *2016 10th European Conference on Antennas and Propagation (EuCAP)*, apr. 2016, pagg. 1–5, doi: 10.1109/EuCAP.2016.7481656.

[57] J. R. Costa, C. A. Fernandes, G. Godi, R. Sauleau, L. L. Coq, e H. Legay, «Compact Ka-Band Lens Antennas for LEO Satellites», *IEEE Transactions on Antennas and Propagation*, vol. 56, n. 5, pagg. 1251–1258, mag. 2008, doi: 10.1109/TAP.2008.922690.

[58] N. T. Nguyen, R. Sauleau, M. Ettorre, e L. L. Coq, «Focal Array Fed Dielectric Lenses: An Attractive Solution for Beam Reconfiguration at Millimeter Waves», *IEEE Transactions on Antennas and Propagation*, vol. 59, n. 6, pagg. 2152–2159, giu. 2011, doi: 10.1109/TAP.2011.2144550.

[59] N. T. Nguyen, A. Rolland, A. V. Boriskin, G. Valerio, L. L. Coq, e R. Sauleau, «Size and Weight Reduction of Integrated Lens Antennas Using a Cylindrical Air Cavity», *IEEE Transactions on Antennas and Propagation*, vol. 60, n. 12, pagg. 5993–5998, dic. 2012, doi: 10.1109/TAP.2012.2208931.

[60] G. V. Trentini, «Partially reflecting sheet arrays», *IRE Transactions on Antennas and Propagation*, vol. 4, n. 4, pagg. 666–671, ott. 1956, doi: 10.1109/TAP.1956.1144455.

[61] S. A. Hosseini, F. D. Flaviis, e F. Capolino, «A highly-efficient single-feed planar Fabry-Pérot cavity antenna for 60 GHz technology», in *Proceedings of the 2012 IEEE International Symposium on Antennas and Propagation*, lug. 2012, pagg. 1–2, doi: 10.1109/APS.2012.6349418.

[62] R. Sauleau, P. Coquet, e T. Matsui, «Low-profile directive quasi-planar antennas based on millimetre wave Fabry–Perot cavities», *IEE Proceedings - Microwaves, Antennas and Propagation*, vol. 150, n. 4, pagg. 274–278, ago. 2003, doi: 10.1049/ip-map:20030416.

[63] A. Hosseini, F. Capolino, e F. D. Flaviis, «Gain Enhancement of a V-Band Antenna Using a Fabry-Pérot Cavity With a Self-Sustained All-Metal Cap With FSS», *IEEE Transactions on Antennas and Propagation*, vol. 63, n. 3, pagg. 909–921, mar. 2015, doi: 10.1109/TAP.2014.2386358.

[64] Y. Lee, X. Lu, Y. Hao, S. Yang, J. R. G. Evans, e C. G. Parini, «Low-Profile Directive Millimeter-Wave Antennas Using Free-Formed Three-Dimensional (3-D) Electromagnetic Bandgap Structures», *IEEE Transactions on Antennas and*

Propagation, vol. 57, n. 10, pagg. 2893–2903, ott. 2009, doi: 10.1109/TAP.2009.2029299.

[65] H. Yang e N. Alexopoulos, «Gain enhancement methods for printed circuit antennas through multiple superstrates», *IEEE Transactions on Antennas and Propagation*, vol. 35, n. 7, pagg. 860–863, lug. 1987, doi: 10.1109/TAP.1987.1144186.

[66] D. Abbou, T. P. Vuong, R. Touhami, F. Ferrero, D. Hamzaoui, e M. C. E. Yagoub, «High-Gain Wideband Partially Reflecting Surface Antenna for 60 GHz Systems», *IEEE Antennas and Wireless Propagation Letters*, vol. 16, pagg. 2704–2707, 2017, doi: 10.1109/LAWP.2017.2742862.

[67] H. Xu, J. Zhou, K. Zhou, Q. Wu, Z. Yu, e W. Hong, «Planar Wideband Circularly Polarized Cavity-Backed Stacked Patch Antenna Array for Millimeter-Wave Applications», *IEEE Transactions on Antennas and Propagation*, vol. 66, n. 10, pagg. 5170–5179, ott. 2018, doi: 10.1109/TAP.2018.2862345.

[68] K. Luk e B. Wu, «The Magnetoelectric Dipole—A Wideband Antenna for Base Stations in Mobile Communications», *Proceedings of the IEEE*, vol. 100, n. 7, pagg. 2297–2307, lug. 2012, doi: 10.1109/JPROC.2012.2187039.

[69] K. Mak, K. So, H. Lai, e K. Luk, «A Magnetoelectric Dipole Leaky-Wave Antenna for Millimeter-Wave Application», *IEEE Transactions on Antennas and Propagation*, vol. 65, n. 12, pagg. 6395–6402, dic. 2017, doi: 10.1109/TAP.2017.2722868.

[70] S. K. Sharma, S. Rao, e L. Shafai, *Handbook of reflector antennas and feed systems. Volume 1, Volume 1,*. 2013.

[71] P. Lam, Shung-Wu Lee, D. Chang, e K. Lang, «Directivity optimization of a reflector antenna with cluster feeds: A closed-form solution», *IEEE Transactions on Antennas and Propagation*, vol. 33, n. 11, pagg. 1163–1174, nov. 1985, doi: 10.1109/TAP.1985.1143516.

[72] M. Zimmerman, S. W. Lee, B. Houshmand, Y. Rahmat-Samii, e R. Acosta, «A comparison of reflector antenna design for wide-angle scanning», in *Digest on Antennas and Propagation Society International Symposium*, giu. 1989, pagg. 266–269 vol.1, doi: 10.1109/APS.1989.134667.

[73] W. Hu *et al.*, «94 GHz Dual-Reflector Antenna With Reflectarray Subreflector», *IEEE Transactions on Antennas and Propagation*, vol. 57, n. 10, pagg. 3043–3050, ott. 2009, doi: 10.1109/TAP.2009.2029275.

[74] J. Huang e Y. Rahmat-Samii, «Fan beam generated by a linear-array fed parabolic reflector», *IEEE Transactions on Antennas and Propagation*, vol. 38, n. 7, pagg. 1046–1053, lug. 1990, doi: 10.1109/8.55616.

[75] P. F. Goldsmith, C.- Hsieh, G. R. Huguenin, J. Kapitzky, e E. L. Moore, «Focal plane imaging systems for millimeter wavelengths», *IEEE Transactions on Microwave Theory and Techniques*, vol. 41, n. 10, pagg. 1664–1675, ott. 1993, doi: 10.1109/22.247910.

[76] B. Rohrdantz, T. Jaschke, T. Reuschel, S. Radzijewski, A. Sieganschin, e A. F. Jacob, «An Electronically Scannable Reflector Antenna Using a Planar Active Array Feed at Ka-Band», *IEEE Transactions on Microwave Theory and Techniques*, vol. 65, n. 5, pagg. 1650–1661, mag. 2017, doi: 10.1109/TMTT.2017.2663402.

[77] Y. Lo, «On the beam deviation factor of a parabolic reflector», *IRE Transactions on Antennas and Propagation*, vol. 8, n. 3, pagg. 347–349, mag. 1960, doi: 10.1109/TAP.1960.1144854.

[78] «GRASP | Reflector antenna design software», *TICRA*. https://www.ticra.com/software/grasp/ (consultato gen. 29, 2021).

[79] J. Vian e Z. Popovic, «Smart lens antenna arrays», in *2001 IEEE MTT-S International Microwave Sympsoium Digest (Cat. No.01CH37157)*, mag. 2001, vol. 1, pagg. 129–132 vol.1, doi: 10.1109/MWSYM.2001.966855.

[80] T. Chaloun *et al.*, «Wide-angle scanning active transmit/receive reflectarray», *IET Microwaves, Antennas & Propagation*, vol. 8, n. 11, pagg. 811–818, 2014, doi: https://doi.org/10.1049/iet-map.2013.0704.

[81] D. McGrath, «Planar three-dimensional constrained lenses», *IEEE Transactions on Antennas and Propagation*, vol. 34, n. 1, pagg. 46–50, gen. 1986, doi: 10.1109/TAP.1986.1143726.

[82] L. Dussopt, A. Moknache, T. Potelon, e R. Sauleau, «Switched-beam E-band transmitarray antenna for point-to-point communications», in *2017 11th European Conference on Antennas and Propagation (EUCAP)*, mar. 2017, pagg. 3119–3122, doi: 10.23919/EuCAP.2017.7928369.

[83] C. Dragone, «Theory of imaging of Cassegrainian and Gregorian antennas», *IEEE Transactions on Antennas and Propagation*, vol. 34, n. 5, pagg. 689–701, mag. 1986, doi: 10.1109/TAP.1986.1143870.

[84] W. Luk and Wong, «A New Wideband Unidirectional Antenna Element», *IJMOT*, 2006.

[85] C.-Y. Shuai e G.-M. Wang, «Substrate-integrated low-profile unidirectional antenna», *IET Microwaves, Antennas & Propagation*, vol. 12, n. 2, pagg. 185–189, 2018, doi: https://doi.org/10.1049/iet-map.2017.0302.

[86] X. Cui, F. Yang, M. Gao, e Z. Liang, «Wideband microstrip magnetoelectric dipole antenna with stripline aperture-coupled excitation», *IET Microwaves, Antennas & Propagation*, vol. 12, n. 9, pagg. 1575–1581, mar. 2018, doi: 10.1049/iet-map.2018.0078.

[87] M. Li e K. Luk, «Wideband Magneto-Electric Dipole Antenna for 60-GHz Millimeter-Wave Communications», *IEEE Transactions on Antennas and Propagation*, vol. 63, n. 7, pagg. 3276–3279, lug. 2015, doi: 10.1109/TAP.2015.2425418.

[88] «ANSYS HFSS: Software di simulazione di un campo elettromagnetico ad alta frequenza». https://www.ansys.com/it-it/products/electronics/ansys-hfss (consultato feb. 14, 2021).

[89] Do-Hoon Kwon, «On the radiation Q and the gain of crossed electric and magnetic dipole moments», *IEEE Transactions on Antennas and Propagation*, vol. 53, n. 5, pagg. 1681–1687, mag. 2005, doi: 10.1109/TAP.2005.846805.

[90] Rui Wu e Q. X. Chu, «A broadband dual-polarized butterfly antenna for base stations», in *2016 IEEE International Conference on Computational Electromagnetics (ICCEM)*, feb. 2016, pagg. 304–306, doi: 10.1109/COMPEM.2016.7588568.

[91] H. Wong, K. Mak, e K. Luk, «Wideband Shorted Bowtie Patch Antenna With Electric Dipole», *IEEE Transactions on Antennas and Propagation*, vol. 56, n. 7, pagg. 2098–2101, lug. 2008, doi: 10.1109/TAP.2008.924765.

[92] N. T. Nguyen, N. Delhote, M. Ettorre, D. Baillargeat, L. L. Coq, e R. Sauleau, «Design and Characterization of 60-GHz Integrated Lens Antennas Fabricated Through Ceramic Stereolithography», *IEEE Transactions on Antennas and Propagation*, vol. 58, n. 8, pagg. 2757–2762, ago. 2010, doi: 10.1109/TAP.2010.2050447.

[93] D. F. Filipovic, S. S. Gearhart, e G. M. Rebeiz, «Double-slot antennas on extended hemispherical and elliptical silicon dielectric lenses», *IEEE Transactions on Microwave Theory and Techniques*, vol. 41, n. 10, pagg. 1738–1749, ott. 1993, doi: 10.1109/22.247919.

[94] R. Sauleau e B. Bares, «A complete procedure for the design and optimization of arbitrarily shaped integrated lens antennas», *IEEE Transactions on Antennas and Propagation*, vol. 54, n. 4, pagg. 1122–1133, apr. 2006, doi: 10.1109/TAP.2006.872563.

[95] B. Chantraine-Bares e R. Sauleau, «Electrically-Small Shaped Integrated Lens Antennas: A Study of Feasibility in Q-Band», *IEEE Transactions on Antennas and Propagation*, vol. 55, n. 4, pagg. 1038–1044, apr. 2007, doi: 10.1109/TAP.2007.893377.

[96] A. Rolland, M. Ettorre, A. V. Boriskin, L. L. Coq, e R. Sauleau, «Axisymmetric Resonant Lens Antenna With Improved Directivity in Ka-Band», *IEEE Antennas and Wireless Propagation Letters*, vol. 10, pagg. 37–40, 2011, doi: 10.1109/LAWP.2011.2109931.

[97] N. T. Nguyen, R. Sauleau, e L. L. Coq, «Reduced-Size Double-Shell Lens Antenna With Flat-Top Radiation Pattern for Indoor Communications at Millimeter Waves», *IEEE Transactions on Antennas and Propagation*, vol. 59, n. 6, pagg. 2424–2429, giu. 2011, doi: 10.1109/TAP.2011.2144554.

[98] K. F. Brakora, J. Halloran, e K. Sarabandi, «Design of 3-D Monolithic MMW Antennas Using Ceramic Stereolithography», *IEEE Transactions on Antennas and Propagation*, vol. 55, n. 3, pagg. 790–797, mar. 2007, doi: 10.1109/TAP.2007.891855.

[99] B. T. Malik, V. Doychinov, S. A. R. Zaidi, I. D. Robertson, e N. Somjit, «Antenna Gain Enhancement by Using Low-Infill 3D-Printed Dielectric Lens Antennas», *IEEE Access*, vol. 7, pagg. 102467–102476, 2019, doi: 10.1109/ACCESS.2019.2931772.

[100] A. P. Feresidis e J. C. Vardaxoglou, «High gain planar antenna using optimised partially reflective surfaces», *IEE Proceedings - Microwaves, Antennas and Propagation*, vol. 148, n. 6, pagg. 345–350, dic. 2001, doi: 10.1049/ip-map:20010828.

[101] D. R. Jackson e A. A. Oliner, «A leaky-wave analysis of the high-gain printed antenna configuration», *IEEE Transactions on Antennas and Propagation*, vol. 36, n. 7, pagg. 905–910, lug. 1988, doi: 10.1109/8.7194.

[102] «ANSYS Savant Technical Features». https://www.ansys.com/it-it/products/electronics/ansys-savant-technical-features (consultato feb. 28, 2021).

[103] H. M. Cheema e A. Shamim, «The last barrier: on-chip antennas», *IEEE Microwave Magazine*, vol. 14, n. 1, pagg. 79–91, gen. 2013, doi: 10.1109/MMM.2012.2226542.

[104] S. Pan, L. Gilreath, P. Heydari, e F. Capolino, «Investigation of a Wideband BiCMOS Fully On-Chip -Band Bowtie Slot Antenna», *IEEE Antennas and Wireless Propagation Letters*, vol. 12, pagg. 706–709, 2013, doi: 10.1109/LAWP.2013.2264538.

[105] L. Marnat, A. A. A. Carreno, D. Conchouso, M. G. Martı´nez, I. G. Foulds, e A. Shamim, «New Movable Plate for Efficient Millimeter Wave Vertical on-Chip Antenna», *IEEE Transactions on Antennas and Propagation*, vol. 61, n. 4, pagg. 1608–1615, apr. 2013, doi: 10.1109/TAP.2013.2241720.

[106] Ruoyu Wang, Yaoming Sun, M. Kaynak, S. Beer, J. Borngräber, e J. C. Scheytt, «A micromachined double-dipole antenna for 122 – 140 GHz applications based on a SiGe BiCMOS technology», in *2012 IEEE/MTT-S International Microwave Symposium Digest*, giu. 2012, pagg. 1–3, doi: 10.1109/MWSYM.2012.6258421.

[107] H. J. Ng, W. Ahmad, M. Kucharski, J. Lu, e D. Kissinger, «Highly-miniaturized 2-channel mm-wave radar sensor with on-chip folded dipole antennas», in *2017 IEEE Radio Frequency Integrated Circuits Symposium (RFIC)*, giu. 2017, pagg. 368–371, doi: 10.1109/RFIC.2017.7969094.

[108] F. Huang, C. Lee, C. Kuo, e C. Luo, «MMW Antenna in IPD Process for 60-GHz WPAN Applications», *IEEE Antennas and Wireless Propagation Letters*, vol. 10, pagg. 565–568, 2011, doi: 10.1109/LAWP.2011.2158379.

[109] W. T. Khan *et al.*, «A D-Band Micromachined End-Fire Antenna in 130-nm SiGe BiCMOS Technology», *IEEE Transactions on Antennas and Propagation*, vol. 63, n. 6, pagg. 2449–2459, giu. 2015, doi: 10.1109/TAP.2015.2416751.

[110] C.-C. Liu e R. G. Rojas, «V-Band Integrated on-Chip Antenna Implemented With a Partially Reflective Surface in Standard 0.13- μm BiCMOS Technology», *IEEE Transactions on Antennas and Propagation*, vol. 64, n. 12, pagg. 5102–5109, dic. 2016, doi: 10.1109/TAP.2016.2620606.

[111] C. Mustacchio, L. Boccia, E. Arnieri, e G. Amendola, «W-Band On-chip Monopole Antenna in Standard 0.13 µm SiGe BiCMOS Technology», in *2019 14th International Conference on Advanced Technologies, Systems and Services in Telecommunications (TELSIKS)*, ott. 2019, pagg. 138–140, doi: 10.1109/TELSIKS46999.2019.9002348.

[112] C. Mustacchio, L. Boccia, E. Arnieri, e G. Amendola, «Gain Enhancement Techniques for Monolithically Integrated Antennas», in *2020 International Workshop on Integrated Nonlinear Microwave and Millimetre-Wave Circuits (INMMiC)*, lug. 2020, pagg. 1–3, doi: 10.1109/INMMiC46721.2020.9160089.

[113] C. Mustacchio, L. Boccia, E. Arnieri, e G. Amendola, «Gain Enhancement Technique for On-Chip Monopole Antenna», in *2020 50th European Microwave Conference (EuMC)*, gen. 2021, pagg. 650–653, doi: 10.23919/EuMC48046.2021.9338160.

[114] P. Perlmutter, S. Shtrikman, e D. Treves, «Electric surface current model for the analysis of microstrip antennas with application to rectangular elements», *IEEE Transactions on Antennas and Propagation*, vol. 33, n. 3, pagg. 301–311, mar. 1985, doi: 10.1109/TAP.1985.1143581.

[115] A. Ali, J. Yun, H. J. Ng, D. Kissinger, F. Giannini, e P. Colantonio, «Sub-THz On-Chip Dielectric Resonator Antenna with Wideband performance», in *2019 49th European Microwave Conference (EuMC)*, ott. 2019, pagg. 912–915, doi: 10.23919/EuMC.2019.8910822.

[116] A. Babakhani, X. Guan, A. Komijani, A. Natarajan, e A. Hajimiri, «A 77-GHz Phased-Array Transceiver With On-Chip Antennas in Silicon: Receiver and Antennas», *IEEE Journal of Solid-State Circuits*, vol. 41, n. 12, pagg. 2795–2806, dic. 2006, doi: 10.1109/JSSC.2006.884811.

[117] R. Pilard, F. Gianesello, D. Gloria, D. Titz, F. Ferrero, e C. Luxey, «60 GHz HR SOI CMOS antenna for a System-on-Chip integration scheme targeting high data-rate kiosk applications», in *2011 IEEE International Symposium on Antennas and Propagation (APSURSI)*, lug. 2011, pagg. 895–898, doi: 10.1109/APS.2011.5996420.

[118] M. Seyyed-Esfahlan, M. Kaynak, B. Göttel, e I. Tekin, «SiGe Process Integrated On-Chip Dipole Antenna on Finite-Size Ground Plane», *IEEE Antennas and Wireless Propagation Letters*, vol. 12, pagg. 1260–1263, 2013, doi: 10.1109/LAWP.2013.2282971.

[119] E. Ojefors, H. Kratz, K. Grenier, R. Plana, e A. Rydberg, «Micromachined Loop Antennas on Low Resistivity Silicon Substrates», *IEEE Transactions on Antennas and Propagation*, vol. 54, n. 12, pagg. 3593–3601, dic. 2006, doi: 10.1109/TAP.2006.886532.

[120] F. Capolino, *Theory and Phenomena of metamaterials*. CRC Press, 2009.

[121] D. Sievenpiper, Lijun Zhang, R. F. J. Broas, N. G. Alexopolous, e E. Yablonovitch, «High-impedance electromagnetic surfaces with a forbidden frequency band», *IEEE Transactions on Microwave Theory and Techniques*, vol. 47, n. 11, pagg. 2059–2074, nov. 1999, doi: 10.1109/22.798001.

[122] J. Grzyb, P. R. Vazquez, N. Sarmah, W. Förster, B. Heinemann, e U. Pfeiffer, «High data-rate communication link at 240 GHz with on-chip antenna-integrated transmitter and receiver modules in SiGe HBT technology», in *2017 11th European Conference on Antennas and Propagation (EUCAP)*, mar. 2017, pagg. 1369–1373, doi: 10.23919/EuCAP.2017.7928160.

[123] H. J. Ng, J. Wessel, D. Genschow, R. Wang, Y. Sun, e D. Kissinger, «Miniaturized 122 GHz system-on-chip radar sensor with on-chip antennas utilizing a novel antenna design approach», in *2016 IEEE MTT-S International Microwave Symposium (IMS)*, mag. 2016, pagg. 1–4, doi: 10.1109/MWSYM.2016.7540353.

[124] W. Shin, B. Ku, O. Inac, Y. Ou, e G. M. Rebeiz, «A 108–114 GHz 4 $\,\times\,$4 Wafer-Scale Phased Array Transmitter With High-Efficiency On-Chip Antennas», *IEEE Journal of Solid-State Circuits*, vol. 48, n. 9, pagg. 2041–2055, set. 2013, doi: 10.1109/JSSC.2013.2260097.

[125] S. Zihir, O. D. Gurbuz, A. Kar-Roy, S. Raman, e G. M. Rebeiz, «60-GHz 64- and 256-Elements Wafer-Scale Phased-Array Transmitters Using Full-Reticle and Subreticle Stitching Techniques», *IEEE Transactions on Microwave Theory and Techniques*, vol. 64, n. 12, pagg. 4701–4719, dic. 2016, doi: 10.1109/TMTT.2016.2623948.

[126] H. Kuo, H. Yue, Y. Ou, C. Lin, e H. Chuang, «A 60-GHz CMOS Sub-Harmonic RF Receiver With Integrated On-Chip Artificial-Magnetic-Conductor Yagi Antenna and Balun Bandpass Filter for Very-Short-Range Gigabit Communications», *IEEE Transactions on Microwave Theory and Techniques*, vol. 61, n. 4, pagg. 1681–1691, apr. 2013, doi: 10.1109/TMTT.2013.2247622.

[127] A. Barakat *et al.*, «Back radiation reduction of 60 GHz CMOS slot Antenna-on-Chip (AoC) using Artificial Dielectric Layer (ADL) for Area Reuse», lug. 2014, pagg. 137–137, doi: 10.1109/USNC-URSI.2014.6955519.

[128] X. Deng, Y. Li, C. Liu, W. Wu, e Y. Xiong, «340 GHz On-Chip 3-D Antenna With 10 dBi Gain and 80% Radiation Efficiency», *IEEE Transactions on Terahertz Science*

and Technology, vol. 5, n. 4, pagg. 619–627, lug. 2015, doi: 10.1109/TTHZ.2015.2424682.

[129] D. Hou *et al.*, «D-band on-chip higher-order-mode dielectric-resonator antennas fed by half-mode cavity in CMOS technology», *IEEE Antennas and Propagation Magazine*, vol. 56, n. 3, pagg. 80–89, giu. 2014, doi: 10.1109/MAP.2014.6867684.

[130] M. O. Sallam *et al.*, «Micromachined On-Chip Dielectric Resonator Antenna Operating at 60 GHz», *IEEE Transactions on Antennas and Propagation*, vol. 63, n. 8, pagg. 3410–3416, ago. 2015, doi: 10.1109/TAP.2015.2439694.

[131] W. H. Syed, G. Fiorentino, D. Cavallo, M. Spirito, P. M. Sarro, e A. Neto, «Design, Fabrication, and Measurements of a 0.3 THz On-Chip Double Slot Antenna Enhanced by Artificial Dielectrics», *IEEE Transactions on Terahertz Science and Technology*, vol. 5, n. 2, pagg. 288–298, mar. 2015, doi: 10.1109/TTHZ.2015.2399276.

[132] S. Li *et al.*, «Performance of V-Band On-Chip Antennas in GlobalFoundries 45nm CMOS SOI Process for Mm-Wave 5G Applications», in *2018 IEEE/MTT-S International Microwave Symposium - IMS*, giu. 2018, pagg. 1593–1596, doi: 10.1109/MWSYM.2018.8439650.

[133] D. Titz *et al.*, «60GHz antenna integrated on High Resistivity silicon technologies targeting WHDMI applications», in *2011 IEEE Radio Frequency Integrated Circuits Symposium*, giu. 2011, pagg. 1–4, doi: 10.1109/RFIC.2011.5940637.

[134] G. Katti, M. Stucchi, K. D. Meyer, e W. Dehaene, «Electrical Modeling and Characterization of Through Silicon via for Three-Dimensional ICs», *IEEE Transactions on Electron Devices*, vol. 57, n. 1, pagg. 256–262, gen. 2010, doi: 10.1109/TED.2009.2034508.

[135] R. Karim, A. Iftikhar, e R. Ramzan, «Performance-Issues-Mitigation-Techniques for On-Chip-Antennas – Recent Developments in RF, MM-Wave, and Thz Bands With Future Directions», *IEEE Access*, vol. 8, pagg. 219577–219610, 2020, doi: 10.1109/ACCESS.2020.3042928.

[136] J. B. Pendry, A. J. Holden, D. J. Robbins, e W. J. Stewart, «Magnetism from conductors and enhanced nonlinear phenomena», *IEEE Transactions on Microwave Theory and Techniques*, vol. 47, n. 11, pagg. 2075–2084, nov. 1999, doi: 10.1109/22.798002.

[137] F. Bilotti, A. Toscano, L. Vegni, K. Aydin, K. B. Alici, e E. Ozbay, «Equivalent-Circuit Models for the Design of Metamaterials Based on Artificial Magnetic Inclusions», *IEEE Transactions on Microwave Theory and Techniques*, vol. 55, n. 12, pagg. 2865–2873, dic. 2007, doi: 10.1109/TMTT.2007.909611.

[138] E. Serrano *et al.*, «SiGe BiCMOS balanced transmission line based on coplanar waveguide and split ring resonator», *Radio Science*, vol. 51, n. 6, pagg. 868–875, giu. 2016, doi: 10.1002/2016RS006033.

[139] Kin-Lu Wong e Yi-Fang Lin, «Stripline-fed printed triangular monopole», *Electronics Letters*, vol. 33, n. 17, pagg. 1428–1429, ago. 1997, doi: 10.1049/el:19970960.

[140] M. Barbuto, F. Bilotti, e A. Toscano, «Design of a multifunctional SRR-loaded printed monopole antenna», *International Journal of RF and Microwave Computer-Aided Engineering*, vol. 22, n. 4, pagg. 552–557, 2012, doi: 10.1002/mmce.20645.

[141] S. Dakhli *et al.*, «Capacitively Loaded Loop-Based Antennas with Reconfigurable Radiation Patterns», *International Journal of Antennas and Propagation*, 2015. https://www.hindawi.com/journals/ijap/2015/523198/ (consultato apr. 07, 2020).

[142] M. SMARI, S. DAKHLI, e F. CHOUBANI, «A Frequency-Reconfigurable Printed Antenna with Switchable Capacitively Loaded Loops», in *2019 15th International Wireless Communications Mobile Computing Conference (IWCMC)*, giu. 2019, pagg. 1422–1425, doi: 10.1109/IWCMC.2019.8766771.

[143] D.-F. Guan, Y.-S. Zhang, Z.-P. Qian, Y. Li, W. Cao, e F. Yuan, «Compact Microstrip Patch Array Antenna With Parasitically Coupled Feed», *IEEE Transactions on Antennas and Propagation*, vol. 64, n. 6, pagg. 2531–2534, giu. 2016, doi: 10.1109/TAP.2016.2547019.

[144] Q. Liu, A. C. F. Reniers, U. Johannsen, M. C. van Beurden, e A. B. Smolders, «Improved Probing Reliability in Antenna-on-Chip Measurements», *IEEE Antennas and Wireless Propagation Letters*, vol. 17, n. 9, pagg. 1745–1749, set. 2018, doi: 10.1109/LAWP.2018.2865605.

[145] M. R. Karim, X. Yang, e M. F. Shafique, «On Chip Antenna Measurement: A Survey of Challenges and Recent Trends», *IEEE Access*, vol. 6, pagg. 20320–20333, 2018, doi: 10.1109/ACCESS.2018.2821196.

[146] L. Verma, M. Fakharzadeh, e S. Choi, «Backhaul need for speed: 60 GHz is the solution», *IEEE Wireless Communications*, vol. 22, n. 6, pagg. 114–121, dic. 2015, doi: 10.1109/MWC.2015.7368832.

[147] R. Chuenchom *et al.*, «E-Band 76-GHz Coherent RoF Backhaul Link Using an Integrated Photonic Mixer», *Journal of Lightwave Technology*, vol. 34, n. 20, pagg. 4744–4750, ott. 2016, doi: 10.1109/JLT.2016.2573047.

[148] M. P. Thakur, S. Mikroulis, C. C. Renaud, J. E. Mitchell, e A. Stöhr, «DWDM-PON/mm-Wave wireless converged Next Generation Access Topology using coherent heterodyne detection», in *2014 16th International Conference on Transparent Optical Networks (ICTON)*, lug. 2014, pagg. 1–3, doi: 10.1109/ICTON.2014.6876454.

[149] P. Chevalier *et al.*, «A 55 nm triple gate oxide 9 metal layers SiGe BiCMOS technology featuring 320 GHz fT / 370 GHz fMAX HBT and high-Q millimeter-wave passives», in *2014 IEEE International Electron Devices Meeting*, dic. 2014, pag. 3.9.1-3.9.3, doi: 10.1109/IEDM.2014.7046978.

[150] P. Chevalier, G. Avenier, E. Canderle, A. Montagné, G. Ribes, e V. T. Vu, «Nanoscale SiGe BiCMOS technologies: From 55 nm reality to 14 nm opportunities and challenges», in *2015 IEEE Bipolar/BiCMOS Circuits and Technology Meeting - BCTM*, ott. 2015, pagg. 80–87, doi: 10.1109/BCTM.2015.7340556.